Artificial Synapses based on the Photoconductance of $LaAlO_3$ /$SrTiO_3$ QuantumWells

Yu CHEN

ADVERTIMENT. L'accés als continguts d'aquesta tesi queda condicionat a l'acceptació de les condicions d'ús establertes per la següent llicència Creative Commons: http://cat.creativecommons.org/?page_id=184

ADVERTENCIA. El acceso a los contenidos de esta tesis queda condicionado a la aceptación de las condiciones de uso establecidas por la siguiente licencia Creative Commons: http://es.creativecommons.org/blog/licencias/

WARNING. The access to the contents of this doctoral thesis it is limited to the acceptance of the use conditions set by the following Creative Commons license: https://creativecommons.org/licenses/?lang=en

Universitat Autònoma de Barcelona (UAB)

Doctoral Thesis

Artificial Synapses based on the Photoconductance of $LaAlO_3/SrTiO_3$ Quantum Wells

---

Author:
Yu Chen

Supervisor:
Dr. Gervasi Herranz Casabona
Tutor:
Prof. Javier Rodrìguez Viejo

A thesis submitted in fulfillment of the requirements
for the degree of Doctor in Materials Science

in the

Laboratory of Multifunctional Oxides and Complex Structures (MULFOX)
Institut de Ciència de Materials de Barcelona (ICMAB-CSIC)

September 19, 2019

Declaration of Authorship

Dr. Gervasi HERRANZ CASABONA, Tenured Scientist at the Institut de Ciencia de Materials de Barcelona (ICMAB-CSIC) and Prof. Javier Rodrìguez Viejo, Professor at Universitat Autònoma de Barcelona (UAB).

Certify,

that Yu CHEN , with a Master in Condensed Matter Physics from the Shanghai University, carried out, under their supervision, the thesis entitled "Artificial Synapses based on the Photoconductance of $LaAlO_3/SrTiO_3$ Quantum Wells". This work has been developed within a Ph.D. program in Materials Science at the Universitat Autònoma de Barcelona at the department of Physics.
For that record they sign the certificate.

Signed (Dr. Gervasi HERRANZ CASABONA):

Signed (Prof. Javier Rodrìguez Viejo):

Signed (Yu CHEN):

Bellaterra, September 2019:

UNIVERSITAT AUTÒNOMA DE BARCELONA (UAB)

Abstract

Universitat Autònoma de Barcelona
Institut de Ciència de Materials de Barcelona (ICMAB-CSIC)

Doctor in Materials Science

Artificial Synapses based on the Photoconductance of $LaAlO_3/SrTiO_3$ Quantum Wells

by Yu CHEN

Recently, inspired by neurobiology, researchers have investigated systems that process information based on spiking neural networks where synaptic plasticity is the kernel of calculation, communication, or even storage of information. In this area, neuromorphic computing is proposed to cope with complex cognitional tasks through emulating spiking neural networks consisting of artificial synapses, aiming at overcoming the von Neumann bottleneck in conventional computational paradigms. In this Thesis, we have investigated the optical properties of the $LaAlO_3/SrTiO_3$ interfaces, which can be exploited as artificial optical synapses due to their persistent photoconductance. In particular, we find that the conductance of these interfaces can be increased or decreased plastically depending on the time order of arrival of optical pulses of different wavelengths. The observed plastic photoresponse, which depends on the order of time arrival of optical stimuli, paves the way to the implementation of spike-timing dependent plasticity (STDP) using light as external stimulus.

In the Thesis we discuss the origin of the observed wavelength-dependent time-correlated photoresponse in epitaxial $LaAlO_3/SrTiO_3$ quantum wells. We conclude that the photoresponse involves two photoexcitation processes, namely, the excitation of electrons located at defect-related DX centers and the photoexcitation to surface states via quantum tunneling. As aforementioned, it is shown that this photoresponse can be adapted to achieve STDP, using the conductance of epitaxial $LaAlO_3/SrTiO_3$ quantum wells as optical synapses. The possibility of exploiting the photoconductance of $LaAlO_3/SrTiO_3$ to emulate some basic cognitive tasks is also explored. Additionally, we have explored the photoconductance of amorphous $LaAlO_3/SrTiO_3$ interfaces, where the conductance is sensitive to illumination conditions in well-lighted environments. We include a discussion about the perspective of using the persistence photoconductance of $LaAlO_3/SrTiO_3$ quantum wells to applications in neuromorphic vision.

Acknowledgements

As the studied artificial synapses are reconfigurable under external stimulus, I am shaping my mind to be a better person under all the experiences. Especially, as the artificial synapses base on the photoconductance of $LaAlO_3/SrTiO_3$ interfaces, I reinforce my knowledge at this doctoral interface – ICMAB. I would like to acknowledge the China Scholarship Council grant *n^o* 201506890029 for supporting me study in ICMAB, and the Spanish Government for the supported projects.

The completion of the thesis is attributed to the valuable and helpful collaborations. I would like to express my deepest gratitude to: Dr. Florencio Sánchez from ICMAB for growing $LaAlO_3$ films, Dr. Blai Casals and Dr.Rafael Cichelero from ICMAB for giving countless scientific and technological suggestions, Dr. Bernat Bozzo Closas from ICMAB for taking Hall-effect measurements, Dr. Laurence Mechin from CNRS - GREYC Caen for the measurements of Deep-Level Transient Spectroscopy, Dr. Mariona Coll from ICMAB for growing AlO_x with ALD, Dr. Jaume Gazquez from ICMAB for supporting the STEM measurements, Dr. Ignasi Fina from ICMAB for developing measurement software, and Prof.Josep Fontcuberta from ICMAB for useful academic suggestions.

A special thanks to Dr. Gervasi HERRANZ CASABONA, it is an impressive and rewarding experience to work with you. I benefit a lot from not only your research methods or academic thoughts but also the approachable and patient personality. As the artificial synapses mimic the biological synapses to achieve strong functionalities, I am trying to emulate you to be a nice scholar in the future academic life.

I am really glad to work at our Laboratory of Multifunctional Oxides and Complex Structures (MULFOX) group, a special thanks to group mates: Dr. Ignasi Fina, Dr. Mikko Kataja, Dr. Blai Casals, Dr. Liu Fanmao, Dr.Mateusz Ścigaj, Dr. Qian Mengdi, Dr. Rafael Cichelero, Dr. Lyu Jike, Dr. Morteza Alizadeh, Dr. Nico Dix, Mathieu, Saúl, Milena, Marc, Sheng Yunwei, Long Xiao, Song Tingfeng and Jia Jiahui. And I wish Sheng Yunwei, Long Xiao, Song Tingfeng and Jia JiaHui, who join in MULFOX group later than me, can enjoy the PhD study, of course, sometimes which may be hard or even frustrated for seeing few output, but you will learn much more than you expected, e.g., you would be inspired by Pep who is an interpreter of Fourier transformation to teach you how to look at a physical problem in a view of band structures instead of only real space, you can learn how to program from the coding wizard Ignasi, or you can feel the scholar charm like Gervasi.

I also would like to acknowledge my office mates: Fu Can, Ma Zheng and Jan. I also thanks to the nice friends at ICMAB: Miquel, Irene, Alejandro, Juri, and Artur.

A special thanks to ICMAB staff. A special mention to Luigi Morrone and Raúl Solanas.

In the past four years, I am also grateful to all my Chinese friends Li Zhi, Lyu Jike, Tan Fangchang, Zhang Qianzhe, Fu Can, Zhang Qiaoming, Liu Daijun, Zhang Chao, Qian Mengdi, Liu Fanmao, Xu Heng, Li Ziliang, Qian Wenjie, Lu Changyong, Sheng Yunwei, Long Xiao, Song Tingfeng, Liu Zhao, Su Huanhuan, Gan Lei, Yu Pengmei, Ma Zheng, Wang Haining, Zhang Xiaodong, Zhang Songbai and others I cannot list explicitly, with whom I have extremely good time. I am really happy to share some moments with Su Huanhuan, Liu Zhao and Gan Lei, who have enriched my experience and mind. A special thanks to Sheng Yunwei, who is always raising questions that inspired me to look deeply into the physical mechanism. I also express my special thanks to Yu Pengmei for growing AlO_x film.

Last but not least, no word can express my gratitude to my parents, who make me want to be myself. Thank you, Papa and Mama.

Contents

Declaration of Authorship iii

Abstract v

Acknowledgements vii

1 Introduction 1
- 1.1 Background 1
- 1.2 Spiking neural networks 5
  - 1.2.1 Physical implementation of plastic synapses 7
    - Electronic memristor 8
    - Photonic synapses 9
- 1.3 $LaAlO_3/SrTiO_3$ interface 10
  - 1.3.1 Perovskite oxides $LaAlO_3$ and $SrTiO_3$ 11
    - $LaAlO_3$ 11
    - $SrTiO_3$ 12
  - 1.3.2 Conductivity mechanism of $LaAlO_3/SrTiO_3$ interface 12
  - 1.3.3 Persistent photoconductance 13
- 1.4 Outline of the thesis 14

2 Methods: experiments and simulations 17
- 2.1 Sample fabrication 17
  - 2.1.1 Deposition 17
    - Pulsed laser deposition 17
    - Metal evaporation 19
    - Atomic Layer Deposition 19
  - 2.1.2 Lithography 20
- 2.2 Photoresponse measurement 21
  - 2.2.1 Confocal microscopy system 21
  - 2.2.2 Controllable Laser source 22
    - Laser Irradiance regulation 22
    - Laser bandwidth 23
    - Measurements under low irradiance 24
- 2.3 Simulations: Brain simulator 25
  - 2.3.1 Biological neurons 25
  - 2.3.2 Description of basic instructions of the Brian simulator 26

Neuron network 26
Synapse 27
2.3.3 An example of Brian simulation 28

3 Photoinduced tunable carrier accumulation and depletion in a quantum well 31
3.1 Abstract 31
3.2 Experimental observations 32
3.3 Theoretical model 32
3.4 Conclusion 39

4 Wavelength-Sensitive Temporal Correlations at the epitaxial $LaAlO_3/SrTiO_3$ 41
4.1 Abstract 41
4.2 Introduction 42
4.3 Results 43
4.4 Discussion of the potential for neuromorphic engineering 47
4.5 Conclusion 49
4.6 Sample preparation and simulations 50
4.6.1 Sample Preparation 50
4.6.2 Simulations of neural networks 50
4.7 Supporting Information 51
4.7.1 Structural characterization of epitaxial $LaAlO_3/SrTiO_3$ samples 51
4.7.2 Long-term depression of photoconductance induced by illumination with two-pulse sequences 51
4.7.3 Simulations of neural networks 53
4.7.4 Emulation of inhibitory synapses with two-pulse sequences 56
4.7.5 Photoconductive spectral response of epitaxial versus amorphous interfaces 56
4.7.6 Reproducibility of photoconductance response 57
4.7.7 Time relaxation of conductance after photoexcitation 58
4.7.8 Voltage readouts in photoconductance measurements 59
4.7.9 Conductance modulation under multiple-pulse sequences 59

5 Plasticity of amorphous $LaAlO_3/SrTiO_3$ 61
5.1 Abstract 61
5.2 Introduction 62
5.3 Experiment 63
5.4 Plastic photoresponse of amorphous $LaAlO_3/SrTiO_3$ interfaces 64
5.5 Conclusion 70
5.6 Supporting information 70
5.6.1 Measurement noise and thermal noise 70
5.6.2 Dependence of the resistance and photoconductance on growth conditions 71

6 Outlook and Perspectives **73**
6.1 Artificial synapses and neurons for vision . . . 73
6.1.1 Photoreceptor and ganglion cells . . . 74
6.1.2 Electric vision . . . 75
6.2 Complex oxide device based on 2DES . . . 76

A Optical lithography protocols **77**

B Photoconductance Calculation Details **79**
B.1 Photoexcitation via DX-resonance states . . . 79
B.2 Calculation of the density of states (DOS) . . . 80
B.2.1 Quantum well states . . . 80
B.2.2 DX-center states . . . 83
B.2.3 Surface states . . . 84
B.3 Deep-level transient spectroscopy (DLTS) . . . 84
B.4 Calculation of the photoconductance . . . 85
B.4.1 Photoexcitation with single pulses . . . 85
B.4.2 Photoexcitation with two-pulse sequences . . . 85
B.5 Photoexcitation without DX-centers . . . 87
B.6 Configuration-coordinate model . . . 87

C Calculation of bulk band structure with matlab **91**

List of publications and communications **95**

Bibliography **97**

List of Figures

1.1 Development of the computer down for Moore's law 3
1.2 Speed and efficiency of neuromorphic hardware platforms 4
1.3 Brain inspiration and neuromorphic neural networks 5
1.4 The address-event representation 6
1.5 Spike Timing-Dependent Plasticity modes 7
1.6 Electronic memristors 8
1.7 Emulation of symmetric spike-timing-dependent plasticity (STDP) 10
1.8 Conducting $LaAlO_3/SrTiO_3$ interface 10
1.9 Schematic sketch of The polar catastrophe. 11
1.10 Schematic illustration of the perovskite structure. 12
1.11 configuration-coordination (c-c) diagram 14

2.1 Sketch of pulsed laser deposition (PLD) setup 18
2.2 Sketch of metal deposition 19
2.3 Sketch of atomic layer deposition 20
2.4 Schematics of the lithography process 21
2.5 Schematics of photoresponse measurement 22
2.6 Schematics of the irradiance measurement 23
2.7 The bandwidth of the laser 24
2.8 Light intensity attenuated by polarizer 25
2.9 The dependence of action potential on the level of depolarization 27
2.10 Simulation of persistence photoconductance based on photo-spikes 28

3.1 Photoexcitation of carriers into or out of the quantum well via DX-centers and quantum tunneling 33
3.2 Time-asymmetric photoexcitation 37
3.3 Electrostatic boundary conditions and carrier depletion 38

4.1 Schematics of Configurational coordinates 42
4.2 PPC and Schematic depiction of the Hall-bar geometry 43
4.3 Photoconductive response of the epitaxial $LaAlO_3/SrTiO_3$ 44
4.4 Tunability of the photoconductance of the epitaxial $LaAlO_3/SrTiO_3$ 45
4.5 Photoconductance to single pulse/two-pulse sequence of light 46
4.6 Photoconductance to the two-pulse sequences 48
4.7 Movement simulation 49
4.8 Temperature dependence of the sheet resistance of $LaAlO_3/SrTiO_3$ interface . . . 50

4.9 Structural characterization of epitaxial $LaAlO_3/SrTiO_3$ samples 51
4.10 Depression of PPC under illumination with V+R/G/B 52
4.11 Depression of PPC under illumination with G+R and B+R/G 53
4.12 Radial and linear plots of the synaptic strengths 55
4.13 Simulation of the decay or depression of the synaptic strength excited by violet light ($\Delta T_v = 40\, ms$) 56
4.14 Spectral photoconductance of an amorphous $LaAlO_3/SrTiO_3$ 57
4.15 Reproducibility of photoconductance response 58
4.16 Conductance changes after photoexcitation with a single violet pulse and a two-pulse sequence of violet plus red 58
4.17 Relative changes of conductance after two two-pulse sequences consisting 59
4.18 Relative changes of conductance after two two-pulse sequences consisting 60

5.1 Experimental setup and crossectional view of the amorphous-$LaAlO_3/SrTiO_3$ interface 63
5.2 Nonlinear increase of resistance and photoconductance is related to the aging of the amorphous $LaAlO_3/SrTiO_3$ interface 65
5.3 Plastic response of the amorphous $LaAlO_3/SrTiO_3$ interface. 66
5.4 Photoconductance under low irradiance at amorphous $LaAlO_3/SrTiO_3$ interface. . 67
5.5 The power spectral density and spectral density of thermal noise. 71
5.6 Normalized photoconductance and resistance of two a-$LaAlO_3/SrTiO_3$ sample with thickness 3 and 6 nm. 71

6.1 Biological vision and its simulation in 2DES systems 74

B.1 The total density of states (DOS) of the π band and σ band in bulk $SrTiO_3$. 81
B.2 Wedge model for quantum well $LaAlO_3/SrTiO_3$ 82
B.3 Density of states (DOS) of $LaAlO_3/SrTiO_3$ interface 83
B.4 Schematics of DLTS measurement 84
B.5 Photoexcitation with two-pulse sequences 86
B.6 Photoexcitation with two-pulse sequences 88
B.7 Large-lattice-relaxation of the DX-centers 89

C.1 Energy Band of bulk $SrTiO_3$ 91

List of Abbreviations

PLD	**P**ulsed **L**aser **D**eposition
ALD	Atomic Laser Deposition
$SrTiO_3$	**S**trontium **T**itanate
$LaAlO_3$	**L**anthanum **A**luminate
2DES	**2** **D**imensional **E**lectron **S**ystem
QW	**Q**uantum **W**ell
PPC	**P**ersistent **P**hotoconductance
DX	**D**onor combine with unknown (**X**) lattice defects
DOS	**D**ensity **of** **S**tate
CMOS	**C**omplementary **M**etal-**O**xide-**S**emiconductor
ANNs	**A**rtificial **N**eural **N**etworks
AER	**A**ddress-**E**vent **R**epresentation
SNNs	**S**piking **N**eural **N**etworks
STDP	**S**pike **T**iming-**D**ependent **P**lasticity
EPSP	**E**xcitatory **P**ost**s**ynaptic **P**otential
IPSP	**I**nhibitory **P**ost**s**ynaptic **P**otential
RAM	**R**andom **A**ccess **M**emory
PCM	**P**hase **C**hange **M**emory
HRS	**H**igh **R**esistance **S**tate
LRS	**L**ow **R**esistance **S**tate
u.c.	**U**nit **C**ell
VB	**V**alence **B**and
CB	**C**onduction **B**and
DB	**D**efect **B**and
DLTS	**D**eep-**L**evel **T**ransient **S**pectroscopy

Dedicated to my parents…

Chapter 1

Introduction

"We humans are neural nets. What we can do, machines can do... Neural networks have connections. Each connection has a weight on it and that weight can be changed through learning. What a neural net does is take activity from the connection times weights and sum them up and decide whether to send outputs."

Geoffrey Hinton

Inspired by neurobiology, we developed Artificial Synapses based on the Photoconductance of $LaAlO_3/SrTiO_3$ Quantum Wells. An introductory background (see Section 1.1) is introduced to present the advantages of information processing based on spiking neural networks (see Section 1.2). Then, the following Section 1.3 describes the properties of $LaAlO_3/SrTiO_3$, with emphasis on the persistent photoconductance, which can be potentially applied to develop artificial synapses. At the end, the outline of this Thesis is given.

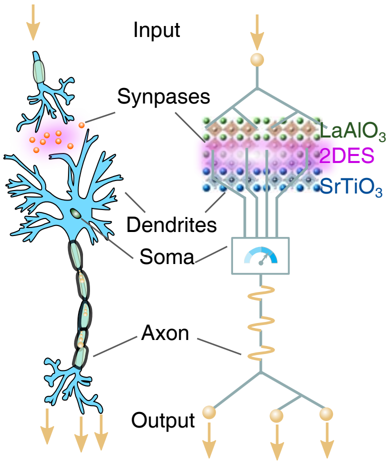

1.1 Background

It is the era fed with big-data, it is the era running in micro-chips. It is the society benefited from information, it is the society polluted by information. It is the world in pursue of efficiency, it is the world consuming time in waiting. It is the planet hungry for energy, it is the planet wasting in energy. Presently scientific and technological progress promotes solutions as well as questions, offers benefits as well as challenges, presents limitations as well as breakthroughs. Today it is on the way towards a fantastic future with a strong intelligence!

In present era of big-data and microprocessor, there are massive achievements always relative to large-scale data processing, such as, the first spectacular image of the black hole captured, which required gathering a big amount of data, about 5 petabyes [1]. As described by Dan Marrone [2], *'it is equivalent to 5000 years of mp3 files'* (at the National Science Foundation/EHT Press

Conference Revealing First Image of Black Hole). Additionally, the recent developments of the data-centric machine learning have been successfully applied in many domains [3], e.g., pattern recognition with much lower error rate [4], speech recognition with industrial application [5], state-of-the-art machine translation [6], natural language understanding [7] and question answering [8], or winning Go game against the world champion [9]. All these astonishing triumphs are based on the machine learning in neural networks, which have the property that *'if you feed it more data, it gets better and better'* notes Andrew Ng [10].

Actually, back in the 1980s and 1990s, many conceptions and algorithms of the machine neural learning have been developed to achieve brain-like function using brain-inspired mechanics [11–13], such as handwritten recognition developed by LeCun [12]. However, rare applications were realized till the last decade. The revival of computing in neural network extremely relies on powerful digital computers, which can operate complex tasks with many parameters and large databases, taking advantage of the enormous progress in technologies based on digital transistors and complementary metal-oxide-semiconductor (CMOS) devices. [14].

To improve the performance and speed of computers, researchers usually attempt to decrease the size of transistors and integrate more transistors per area, sustaining an exponential increase of operation frequency and device density [15]. However, as shown in Figure 1.1 (a), the power density is also increasing with the increasing frequency, finally resulting in large power dissipation that may damage the chip, the so-called thermal wall [16] (seen in Figure 1.1 (b)) . That's the one of the downscaling limitations. Another one is memory wall [17], also known as Von Neumann bottleneck. In the modern computer based on the von Neumann architecture, the central processing units (CPU) and main memory are separated physically and connected by a central bus consisting of a collection of wires [18] (shown in Figure 1.1 (c)). The data and machine instructions shuttle back and forth over a central bus between the CPU and the main memory, resulting in an bottleneck in multi-task devices that compete simultaneously for bus access, leading to performance degradation with increasing dissipation of the power. Thus, this architecture is time- and energy- consuming in the data movement rather than computation.

The performance can be improved through re-engineering the individual components, e.g., making an extensive use of parallelism including, for instance, graphic processing units (GPU), specific processors like Eyeriss as accelerators [20], tensor processing units (TPU) [21] or the introduction of enhanced bandwidth memory [22, 23]. In any case, the main inefficiency of the von Neumann architecture, related to shared interconnections which cannot be accessed simultaneously, has to be overcome. For instance, the supercomputer Titan capable for around 20 petaFLOPS (2×10^{16} floating-ponit operations per second) tackles a complex pattern recognition with an energy consumption as high as $\sim 10^6\ W$ [24]. To perform a cognitive task beyond current supercomputers, astonishingly, human brain just cost roughly 20 W of power [25, 26], relying on a massively parallel and reconfigurable neural network with $\sim 10^{11}$ neurons and $\sim 10^{15}$ synapses [27] (seen Section 1.2). Inspired by the brain, which operates complex tasks efficiently and effectively without any separation between processor and main memory [28], the neuromorphic computing is proposed to process information in situ, where computation and data storage are collocated [29], aiming at mimicking the networks of neurons and synapses in the brain to surpass the von Neumann paradigm.

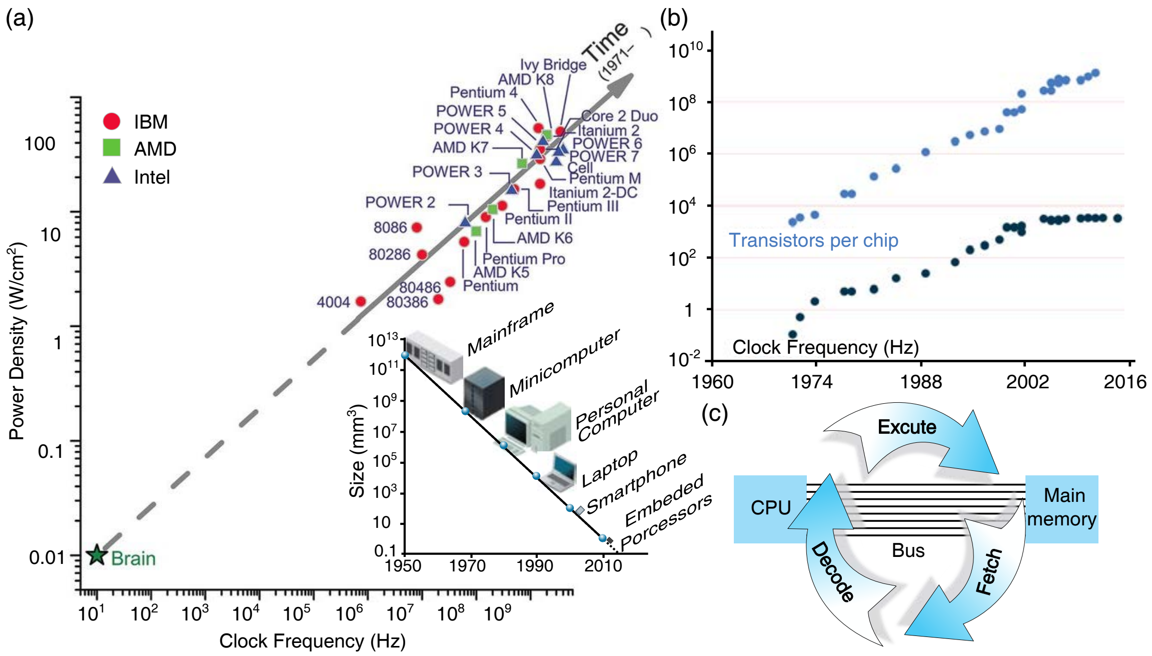

FIGURE 1.1: (a) The trend of increasing clock frequency and power density of today's computers with the sequential and centralized Von Neumann architecture from IBM, Incorporated; Advanced Micro Devices (AMD), Incorporated; Intel, Incorporated. In contrast, the brain, with a parallel, distributed architecture, is more effective and efficient in terms of low power density and operation frequency (**adopted from Ref.** [19]). The inset shows the size reduction in computer and the different computing architectures evolving with time. (b) Increase of density of transistors and clock frequencies. The latter show a slowdown in 2004, due to increased heat dissipation (**adopted from Ref.** [17]). (c) Von Neumann architecture of the modern computer with a bus connected between the CPU and main memory. A circle of executing instructions includes fetch (retrieve instruction from memory to CPU), decode (decode the bit pattern in the instruction resister of CPU) and execute (perform the action required by the decoded instruction in CPU). During operating a task, a considerable amount of data and instruction are fetched back and forth between CPU and the main memory [18].

As an the attempt to develop a hardware implementation of artificial neural networks (ANNs), a team of researchers at IBM built a famous system named TrueNorth [19], which integrated a million silicon spiking-neurons to emulate a neurological system where information is processed in an address-event representation (AER). Running a standard benchmark, at the operating point where neurons fire at 20 Hz and have 128 active synapses, TrueNorth consumes 72 mW, which is 176000 times less than a modern general-purpose microprocessor [19]. Besides the IBM TrueNorth via the DARPA SyNAPSE program [19], more and more projects are making vigorous efforts toward neuromorphic hardware [30], e.g., neuristor built with Mott memristors from HP [31], Loihi system from Intel [32], differentiable neural computer from Google [33], Heidelberg HICANN chip via the FACETS/BrainScaleS projects [34], Stanfords Neurogrid [35], or the SpiNNaker Project [36].

These large-scale spiking neural networks (SNNs) implemented in electronics achieve high power efficiency, orders of magnitude better than standard digital computers with point-to-point links between memory and CPU. However, a neuromorphic processor typically requires

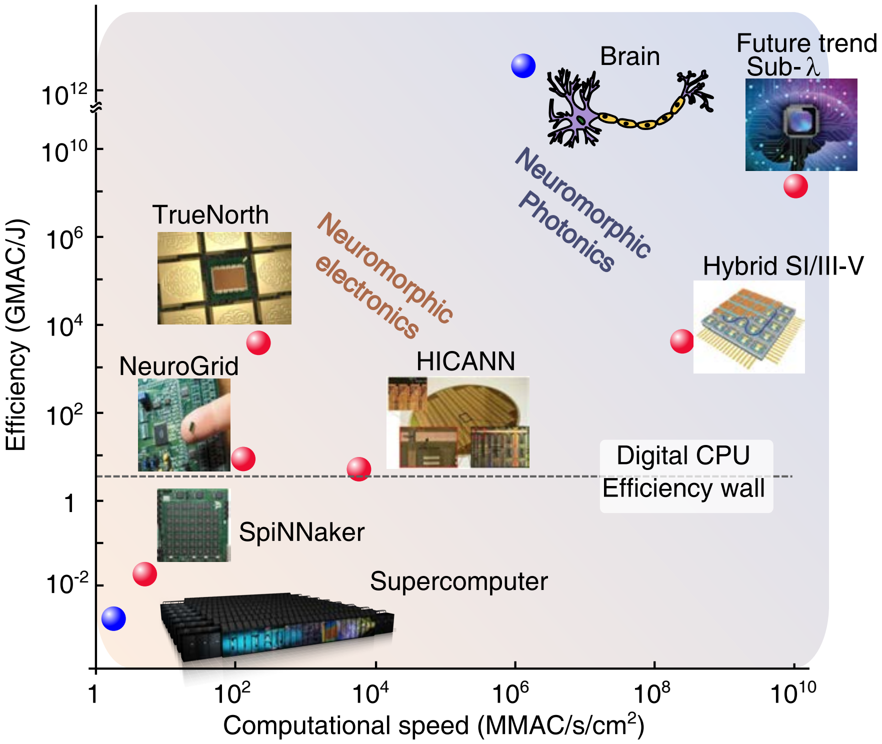

FIGURE 1.2: Speed and efficiency metrics among various neuromorphic hardware platforms. The red points are **extracted from Ref.** [37], standing for recent neuromorphic electric hardware [19, 34–36] and the photonic platform [37]. The computational power efficiency for brain is estimated around 10^{20} MAC/s [37]. The value of the presented supercomputer is not exact, which is evaluated using the floating-point operations per second (FLOPS) at a specific task [19].

a significant number of interconnects (many-to-one fan-in per processor) [25], resulting in a distributed communication burden [37]. The electronic SNNs based on address-event representation (AER) are effective at the associated application from kHz regime [19] to low MHz regime [34], reaching the limitation of neuromorphic processing for high-bandwidth applications that require GHz operation per neuron due to the interconnection.

Therefore, moving towards neuromorphic photonics as shown in Figure 1.2, the computational speed and energy-consumption can be improved further in $6-8$ orders of magnitude [37]. Figure 1.2 shows a digital CPU efficiency wall located at around 10^{10} MAC/W [25], where MAC is the multiply-accumulate-operation which can be used to compare the various neuromorphic platforms. On other hand, the capability of human brain for computing is estimated around 10^{20} MAC/W [37]. The efficiency gap between the biological neuron and the current digital circuits is very large. So far the power efficiency is one of the main drivers for the neuromorphic community. Recent developments of large-scale integration techniques in photonics are pushing towards both the speed and efficiency.

All aforementioned neuromorphic systems built on spiking neural networks require metallic interconnections -- artificial synapses, where the specific weights of synapses can be changed by sparse events (spikes). Thus the electronic or photonic synapses play an important role in the implementation of neuromorphic computers, attracting considerable investigations to emerging memory devices. The following subsections discuss the spiking neural network and artificial synapses implemented by electronics and photonics (Section 1.2), including the optical synapses proposed in this Thesis, based on the phototransport properties of a specific two-dimensional electron system (2DES), located at the $LaAlO_3/SrTiO_3$ interface (Section 1.3). The last section (Section 1.4) gives the outline of this thesis.

1.2 Spiking neural networks

The human brain possesses massively parallel and reconfigurable neural networks of $\sim 10^{11}$ neurons and $\sim 10^{15}$ synapses, operating at ultralow power consumption [27]. The basic unit of the neural network is composed of different parts, as shown in Figure 1.3 (a), including the neuron body soma, dendrites responsible for receiving signal, and axon for transmitting signal out (output). Synapses are located at the junction between the axon and dendrites. Synaptic plasticity is the capability to change the weight of the synapse, so that the connection strength can be enhanced or weakened, and is believed to be responsible for the learning and memory process in the brain. Synapses play the role of adaptable valves at the network nodes. When a signal is excited in a neuron and travels to the axon, it causes the synapses to update the weight and decide (through a threshold value) if the signal must propagate (by firing a spike) into the dendrites of the next neurons. That's the plastic connections driven by spikes, as summarized by Lowel and Singer - 'neurons that fire together, wire together' [38].

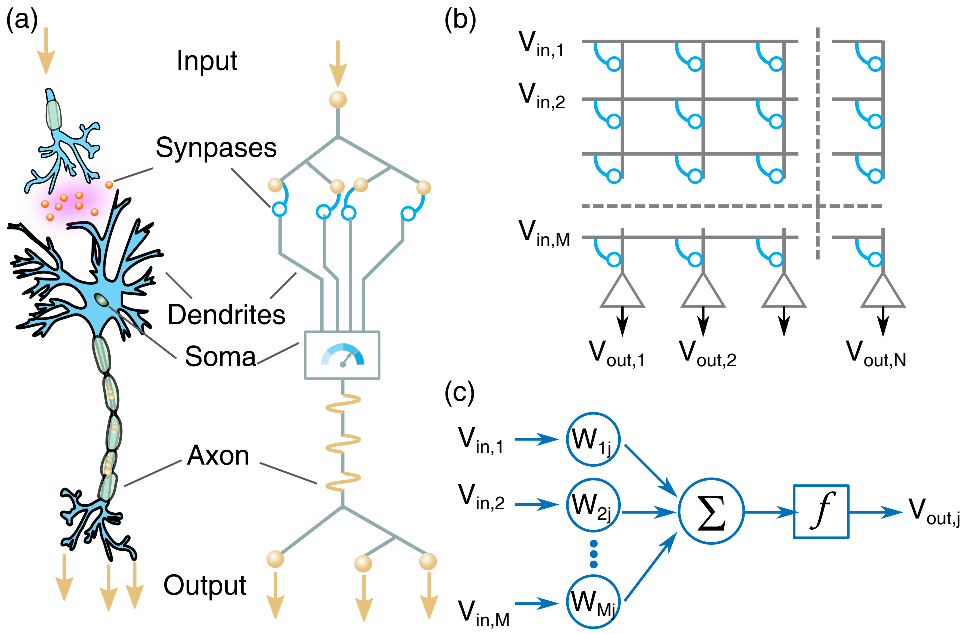

FIGURE 1.3: Brain inspiration and neuromorphic neural networks. (a) Unit neuron and neuromorphic neuron [39]. (b) Schematic of artificial neural networks. (c) Schematic of accumulating weight and threshold operation.

Inspired by biological neural networks, spiking neural networks (seen in Figure 1.3) are employed in neuromorphic computers, where massive metallic devices are linked up in decentralized networks with communication lines between components rather than through a central processor with digital operation [39], mimicking the brain's low-power processing. In the standard computer, a large enough voltage is applied to flip the states representing '0' and '1'. However, small voltages, even lower than the threshold to flip a state, can be used to gather small amount of electrons, which could be accumulated and change some physical property. Based on that, Carver Mead put forward the neuromorphic idea [40]. Under the stimuli with electric or optic pulses, the neuromorphic device receives the input signals through the artificial synapses, which allows the incoming signals to modulate some device properties, e.g., voltage or resistance. If the accumulating states reach a certain threshold, the neuromorphic neuron 'fires' a series of spikes that travel along the wires as electric impulses or as electromagnetic waves [41] or waveguides [42] in photonic neuromorphic devices, which perform the role of axons and dendrites, enabling the communication between neurons. During the process, spikes are either fired or unfired like 'digital', while the fire condition is achieved by integrating inputs in a non-digital way using very low energy. By contrast, a digital computer needs a constant flow of energy to run an internal clock to restricted voltages and currents to a few discrete value as bits, whether or not the chips are computing anything [39].

In other words, a great number of synapses are able to accumulatively pre-process the raw input signal, forming 'digital' spikes of the useful data, resulting in minimizing the amount of data that has to be transmitted and processed. That's the efficiency of the computing driven by event (spike). On the other hand, the speed of the neural/neuromorphic operation is fast due to massive parallel neural networks. The spare events (spikes) are transmitted between neurons via an asynchronous communication protocol -- address-event representation (AER) [43]. As shown in Figure 1.4, the events containing the timing of the spike can be packaged with a sender/receiver neurons address headers, forming a temporal stream to transmit through a shared bus. Then the temporal information is decoded by the postsynaptic neurons and the spike timing is preserved [44].

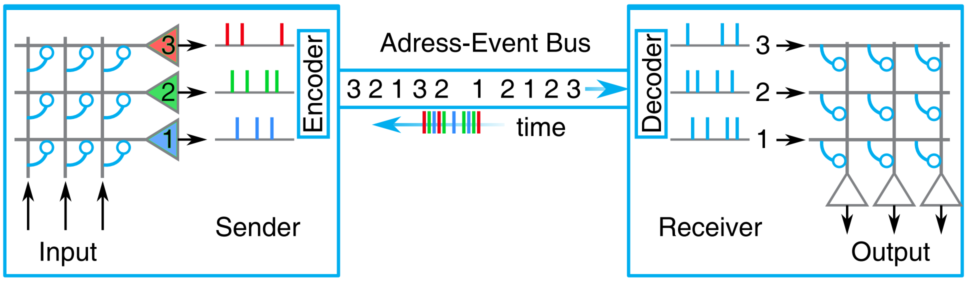

FIGURE 1.4: The address-event representation (**reproduced from Ref.** [44]).

The neural or neuromorphic spike timing is critical for coding or decoding not only in the computing operation but also in the learning process. From the phenomenological point of view, the most promising of the unsupervised learning mechanisms based on synaptic plasticity is Spike Timing-Dependent Plasticity (STDP), where the timing between the spikes actually governs the learning. Lets consider pre-spike neurons with synaptic connections to post-spike neurons (Figure 1.5 (a)). In the case that the pre-synaptic spike is taking place before the post-synaptic spike, it causes an increase of the synaptic weight. This can be understood as implying a "causal relation", so that the system reinforces the synaptic connections whenever pre-synaptic neurons fire before post-synaptic neurons. In the opposite case, if the post-synaptic spike is excited before the pre-synaptic spike, the synaptic weight decreases, implying an anti-causal relation. The connection between two neurons can be strengthened by the causality of the input signals, leading to long-term potentiation of synapses. On the contrary, synaptic strength is weakened by "anti-causal" sequences of inputs, causing long-term depression of synaptic connections. Such delay between the spikes controls the synaptic plasticity to change the interaction, forming various forms of STDP curves, as shown in Figure 1.5 (b), where the rightmost is exactly found in vivo like Hippocampus [45] (seen in Figure 1.5 (c)). STDP can be considered as an adaptable classification function in the unsupervised learning. As Prof. Daniele Ielmini commented, 'You don't really need to elaborate the shape and get the exponential shape that is observed in the biology. What is really needed is just that you have potentiation for positive spike and depression for negative spike'. (At first edition of Artificial Intelligence International Conference [46])

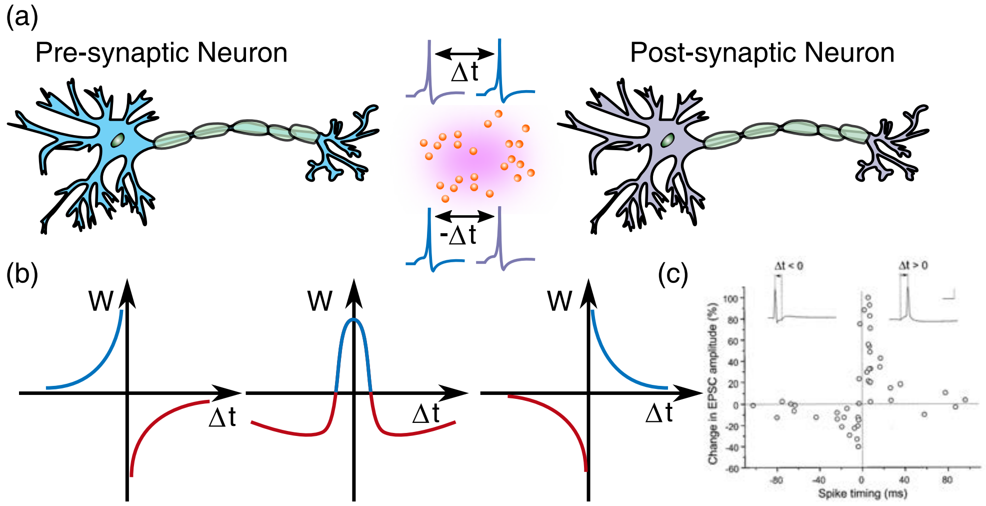

FIGURE 1.5: (a) Schematic of pre-synaptic neuron and post-synaptic neuron. (b) Different forms of the STDP [47]. (c) STDP found in Hippocampus. The EPSP represents excitatory postsynaptic potential (**adapted from Ref.** [45]).

Therefore, building artificial synapses based on devices that simulate plastic connection weights is the core of neuromorphic computing. Interestingly, as discussed in Section 1.2.1, recent developments rely on non-volatile memories that exhibit adjustable physical states by external stimuli. These new memories can remain in the state that is written or erased for long time without external voltage applied, which is similar to the long-term memory in the brain.

1.2.1 Physical implementation of plastic synapses

Based on the biological neuron, the artificial neuron comprises the aforementioned basic components: first, the soma, which operates on the summation. A threshold for neuron firing can be realized using variety of electronic or photonic circuits. Finally, axons and dendrites always act as interconnections, so that simple electronic wires or waveguides [42] can be used to replicate the action of axons and dendrites. The central function of the synaptic weight can be achieved by synaptic devices, which can be implemented via changes of the electric resistance driven by, e.g., electric fields. This subsection discusses electronic memristors and neuromorphic devices that replicate plastic synapses.

Electronic memristor

With electrical stimuli, the in-memory computing can be implemented on a variety of memristors, such as resistance switching random access memory (RRAM), phase change memory (PCM), magnetoresistive RAM (MRAM) and ferroelectric RAM (FrRAM), as shown in Figure 1.6 [14]. These memristors facilitate reading and programing by electric pulses and retention of information for long-term through changing the state, e.g., transport resistance or charge distribution.

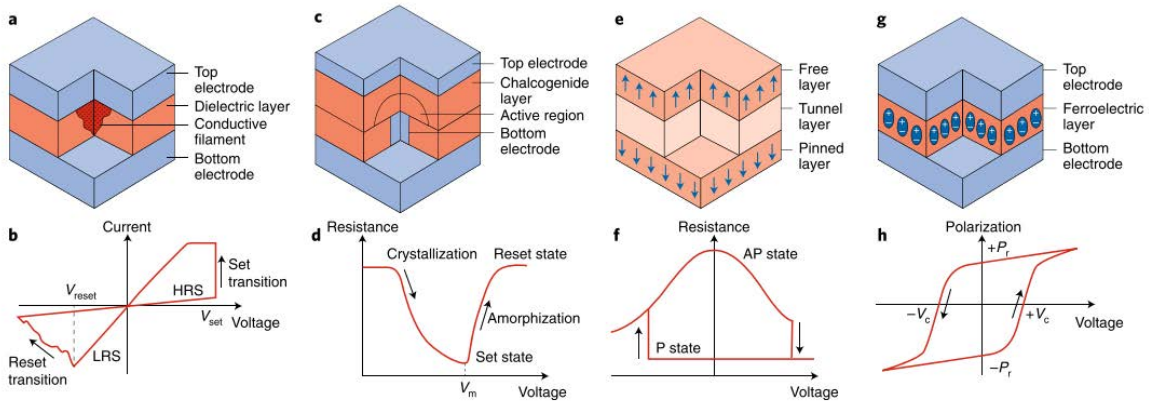
a
Top electrode
Dielectric layer
Conductive filament
Bottom electrode
c
Top electrode
Chalcogenide layer
Active region
Bottom electrode
e
Free layer
Tunnel layer
Pinned layer
g
Top electrode
Ferroelectric layer
Bottom electrode
b
Current
Set transition
V_{reset}
HRS
V_{set}
Voltage
Reset transition
LRS
d
Resistance
Crystallization
Reset state
Amorphization
Set state
V_m
Voltage
f
Resistance
AP state
P state
Voltage
h
Polarization
$+P_r$
$-V_c$
$+V_c$
Voltage
$-P_r$

FIGURE 1.6: (a), (c), (e) and (g) Structure of RRAM, PCM, MRAM and FrRAM, respectively. (b) Currentvoltage characteristic of RRAM. (d) and (f) the resistance change characteristic of PCM and MRAM, respectively. (h) Polarizationvoltage hysteretic characteristic of FrRAM (**adapted from Ref.** [14]).

Basically, the RRAM comprises two electrodes and a dielectric where the resistance state can be reversibly switched. As in Figure 1.6 (b), when a positive voltage exceeds a threshold value, the device is switched from the high resistance state (HRS) to low resistance state (LRS), due to the formation of conductive filaments [48] driven by the field-induced migration and diffusion of defects, e.g., oxygen vacancies causing reproducible resistance switching [49]. When the opposite field is applied, the reverse migration of defects disconnects the filaments, resulting in a transition from HRS to LRS. Additionally, other devices relying on voltage-induced defect migration, such as Schottky or tunneling barriers [50], also can be considered resistor switching memories.

Another route is using PCM. Phase change material, such as $Ge_2Sb_2Te_5$ [51], can be reversibly changed from the crystalline phase (LRS) to the amorphous phase (HRS) induced by Joule heating, as shown in Figure 1.6 (d). Compared to RSM devices, which may involve chemical process due to redox reactions and migration, PCM emerges only under physical phase changes.

Artificial synapses can be also built using magnetic tunnel junction (MTJ). As shown schematically in Figure 1.6 (e), the ferromagnetic polarization in the free layer can be flipped so that it can be parallel or antiparallel with respect to the ferromagnetic polarization in the fixed layer, resulting in a low or high resistance of the MTJ, respectively. Based on the MTJ with control on the ferromagnetic polarization, the device can also use spin transfer torque magnetic random access memory (STT-MRAM), achieving high switching speed, and low-energy operation [52]. Based on STT-MRAM, recently, nanoscale spintronic oscillators were created to mimic neural networks and achieve spoken-digit recognition [53].

In contrast to transport resistance changing in the RRAM, PCM and MRAM, the electric polarization is switched in the FeRAM (seen in Figure 1.6 (g)), which reduces charge distribution in the electrodes, causing changes in capacitance. Instead of two-terminal devices, the resistance change can be achieved via building a ferroelectric field-effect transir (FeFET) [54] where the channel resistance can be altered by the varying polarization controlled by the gate field.

Photonic synapses

As discussed above, the physical implementation of synaptic plasticity is nowadays done with electronic memristors, using electrical stimuli as inputs. However, the electronic interconnectivity could still limit the bandwidth. Photonic neuromorphic devices can display significant advantages, e.g., larger bandwidth, faster propagation and processing, multiplexing (time, space, polarization, angular momentum, wavelength) and lower power computation stimulus. What's more, photonic synapses can be directly applied to visual sensors. Therefore, the future's demand for neuromorphic computers with high speed and performance should benefit from photonic synapses stimulated by light.

As early as in 1980s, neural networks were most readily implemented using optoelectronic neurons with architectures of holographic combinations acting as artificial synapses [55] between light sources (input) and photodetectors with electronic circuits processing threshold (output). Afterwards, uisng photonic circuits on a chip with lasers and photodetectors, various approaches were developed to achieve reconfigurable photonic connectors that could replicate synaptic plasticity, using Mach-Zehnder interferometers (MZI) [42] and micro-ring resonator (MRR) [56]. Yet, such kind of photonic synapses are difficult to be integrated densely on chips to build large-scale neural networks, owing to the size of reconfigurable devices ranging from 625 to $20,000\,\mu m^2$ [57].

Thus, instead of structure-dependent photonic synapses, alternative solutions are suggested to realize artificial synapses. For instance, based on photon-assisted vacancy migration, similar to memristor filaments driven by electric fields, optogenetics-inspired tunable synaptic functions are reported in the $CH_3NH_3PbI_3$ (MAPbI3)-based memristor [59]. On the other hand, recently, optical synapses have been proposed based on the phenomenon of persistent photoconductance (PPC), where carriers can remain for long periods in photoexcited states (more details will be presented in the following Section 1.3). Based on PPC, photonic synapses have been proposed using amorphous oxide semiconductors (Figure 1.7) [58]. In the same vein, a phototransistor synapse has been implemented in heterostructures integrating graphene with single-walled carbon nanutubes [60].

In this Thesis we propose that the persistent photoconductive properties of the $LaAlO_3/SrTiO_3$ interface can be also applied to build artifical optical synapses. In particular, we find that phototransport at the $LaAlO_3/SrTiO_3$ interface is sensitive to wavelength-dependent time-correlated optical pulses in a way that can replicate STDP using optical stimuli instead of electrical (Chaper

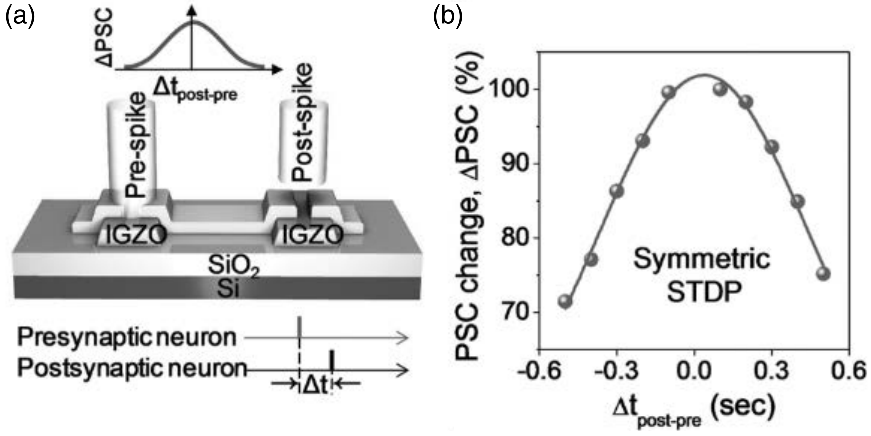

FIGURE 1.7: (a) A schematic of lateral synpase and (b) emulation of spike-timing-dependent plasticity in the IGZO (indium-strontium-zinc-oxide) synaptic devices (**adapted from Ref.** [58]).

4). In Chapter 3 we give a physical explanation of the observed wavelength-dependent time-correlated phototransport. Finally, we show that amorphous $LaAlO_3/SrTiO_3$ interfaces are sensitive to illumination conditions comparable to sunlight environments (Chapter 5). Before proceeding, the following section will briefly present the properties of the $LaAlO_3/SrTiO_3$ interface.

1.3 $LaAlO_3/SrTiO_3$ interface

Symmetry breaking always offers a fertile playground to explore emerging phenomena absent in high symmetry systems and utilized to design novel devices with multiple functionalities. More specifically, atomic and electronic reconstructions can appear at the interface between two different materials, promoting the emergence of new properties. Along these lines, the Nobel laureate Herbert Kroemer coined the sharp and precise phrase that 'The interface is the device', referring to the astonishing success of semiconductor devices [62].

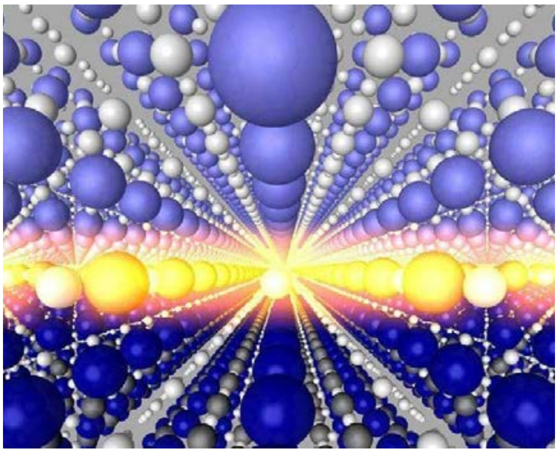

FIGURE 1.8: Conducting $LaAlO_3/SrTiO_3$ interface Image: J. MANNHART (MPI-FKF) & A. HERRNBERGER (UNIV. AUGSBURG) [61]. Thin film $LaAlO_3$ (denoted as the light blue) grows on the substrate $SrTiO_3$ (denoted as the dark blue), yielding a conducting interface shown in the highlighted area.

Over the past decades, advances in complex thin film growth have enabled atomic-scale contol of heterostructures and interfaces, resulting in a considerable number of breakthroughs. One particularly relevant discovery was made by A. Ohtomo and H.Y. Hwang [63], who found a conducting interface between the two insulators ($SrTiO_3$ and $LaAlO_3$), as shown in Figure 1.8. This interface supports a two-dimension electron system (2DES), with carrier densities around $3 \times 10^{13}/cm^2$ and a mobility that may exceed

$10^4\ cm^2V^{-1}s^{-1}$ at low temperature. In addition, a variety of physical properties and phenomena emerge, such as the coexistence of superconductivity and magnetism [64, 65], large spin-orbit coupling [66], or, more relevant in the context of this Thesis, persistence photoconductance [67]. The following subsections will briefly discuss the properties of $LaAlO_3/SrTiO_3$ heterostructure.

1.3.1 Perovskite oxides $LaAlO_3$ and $SrTiO_3$

Perovskite oxides refer to a kind of ceramic oxides with the structure formula ABO_3, where 'A' cations are larger than 'B' cations, and both of them are bonded to 'O' -- oxygen anions. The ideal cubic perovskite (shown in Figure 1.9 (a)) contains A ions at the corners in 12-fold coordinated by oxygen anions, a B ion in the center in 6-fold coordination surrounded by the in oxygen anions in the middle of the faces. Additionally, depending on external parameters like temperature or pressure and internal parameters like cation substitution, pervoskites can experience different structure phases, such as orthorhombic, tetragonal, rhombohedral and monoclinic. Extended to periodic structure, the perovskite can be considered as a BO_6 octahedra network, as shown in Figure 1.9 (b). Along (001) direction, ABO_3 compounds can also be seen as a sequence of alternating AO and BO_2 layers (shown in 1.9 (C)) .

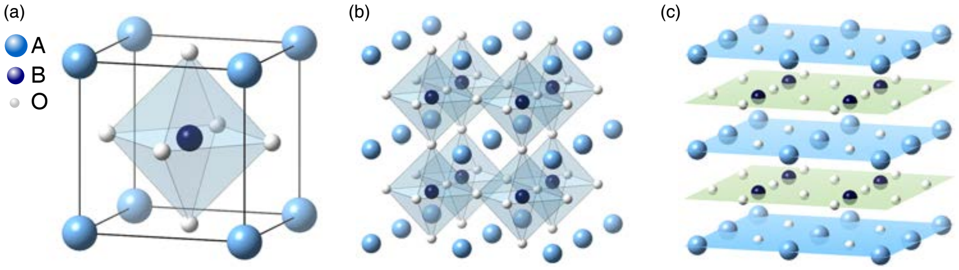

FIGURE 1.9: (a) A cubic unit cell of perovskite structure. (b) a periodic perovskite network of corner-sharing BO_6 octahedra. (c) Alternative AO and BO_2 layers stacking along the (001) direction.

As the blocks of the $LaAlO_3/SrTiO_3$ heterostructure, the perovskite oxides both $LaAlO_3$ and $SrTiO_3$ are band insulators with energy gap $\Delta E = \sim 3\,eV$ and $\Delta E = 5.6\,eV$, respectively.

$LaAlO_3$

$LaAlO_3$ has been extensively studied as a substrate material for the good lattice matching with many oxide materials [68]. In our thesis, the $LaAlO_3$ was a thin film grown on the substrate $SrTiO_3$. At high temperature $LaAlO_3$ crystallizes in the cubic perovskite structure with space group $Pm\bar{3}m$, and at $\sim 813\,K$ undergoes transition to a rhombohedral structure with space group $R\bar{3}c$ [69, 70]. Through the thesis, the measurements were carried out at room temperature, where the $LaAlO_3$ can be considered as a pseudo-cubic perovskite with a lattice constant of 3.791Å [70]. Compared with $SrTiO_3$, lattice mismatch is relatively small and thermal expansion coefficients are similar [71], enabling $LaAlO_3$ films to epitaxially grow on the $SrTiO_3$. In addition, the high value of the dielectric constant ~ 25 at temperature between $300\,K$ and $4\,K$ [68, 72], enables the use of $LaAlO_3$ as thin dielectric films in field effect devices [64, 73].

$SrTiO_3$

$SrTiO_3$ has long captured considerable attention last decades for its attractive physical properties. As a substrate, $SrTiO_3$ can be used to epitaxially grow many other perovskite oxides. $SrTiO_3$ itself also arouses scientific interest, e.g., remarkably, two-dimensional electron is found at the vacuum-cleaved surface of $SrTiO_3$ [74], and $SrTiO_3$ can become superconducting at 0.3 K, as Bednorz and Muller described at 1987 Nobel Prize lecture [75], *'The key material, pure SrTiO3, could even be turned into a superconductor if it were reduced, i.e. if oxygen were partially removed from its lattice...'*. Many of these properties are related to the different possible valences of the Ti ion, and sensitivity of the extrinsic doping.

At room temperature $SrTiO_3$ is cubic (space group $Pm\bar{3}m$) with a lattice constant of 3.905 Å. The intrinsic $SrTiO_3$ with an indirect band gap of 3.25 eV, but it becomes metallic when it is doped with oxygen vacancies [76, 77] or substituting small amounts of the cations [77].

1.3.2 Conductivity mechanism of $LaAlO_3/SrTiO_3$ interface

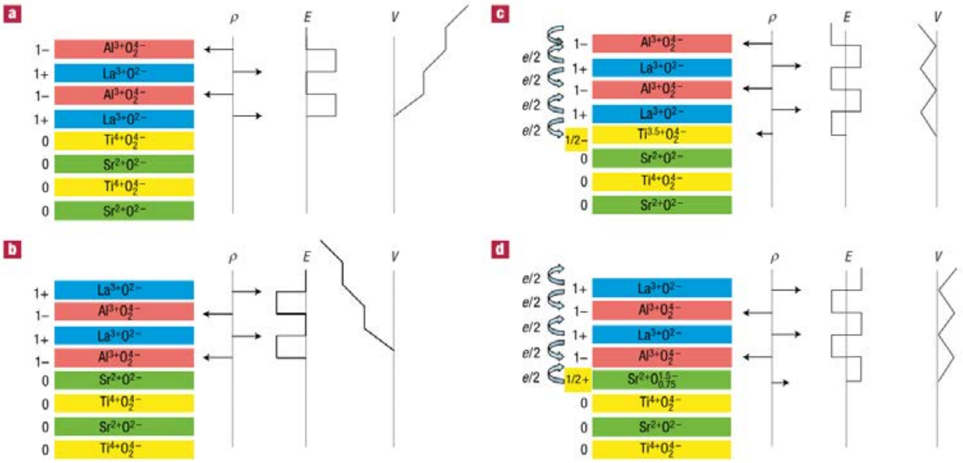
a
ρ
E
V
1−
1+
1−
1+
0
0
0
0
$Al^{3+}O_2^{4-}$
$La^{3+}O^{2-}$
$Al^{3+}O_2^{4-}$
$La^{3+}O^{2-}$
$Ti^{4+}O_2^{4-}$
$Sr^{2+}O^{2-}$
$Ti^{4+}O_2^{4-}$
$Sr^{2+}O^{2-}$
b
1+
1−
1+
1−
0
0
0
0
$La^{3+}O^{2-}$
$Al^{3+}O_2^{4-}$
$La^{3+}O^{2-}$
$Al^{3+}O_2^{4-}$
$Sr^{2+}O^{2-}$
$Ti^{4+}O_2^{4-}$
$Sr^{2+}O^{2-}$
$Ti^{4+}O_2^{4-}$
c
e/2
e/2
e/2
e/2
1−
1+
1−
1+
1/2−
0
0
0
$Al^{3+}O_2^{4-}$
$La^{3+}O^{2-}$
$Al^{3+}O_2^{4-}$
$La^{3+}O^{2-}$
$Ti^{3.5+}O_2^{4-}$
$Sr^{2+}O^{2-}$
$Ti^{4+}O_2^{4-}$
$Sr^{2+}O^{2-}$
d
e/2
e/2
e/2
e/2
e/2
1+
1−
1+
1−
1/2+
0
0
0
$La^{3+}O^{2-}$
$Al^{3+}O_2^{4-}$
$La^{3+}O^{2-}$
$Al^{3+}O_2^{4-}$
$Sr^{2+}O_{0.75}^{1.5-}$
$Ti^{4+}O_2^{4-}$
$Sr^{2+}O^{2-}$
$Ti^{4+}O_2^{4-}$

FIGURE 1.10: Schematic illustration of the perovskite structure (**adapted from Ref.** [63]). Superscripts denote the oxidation numbers. ρ represents the net charge of the layers which reduces an electric field E, resulting in an electric potential V. (a) and (b) The unreconstructed n-type and p-type interface, respectively, lead to a diverging potential – polar catastrophe. (c) The transfer of half an electron can avoid the potential divergence, causing a n-type conducting interface. (d) Transfer of half a hole or removal of half an electron can prevent the divergence.

The origin of the 2DES at the $LaAlO_3/SrTiO_3$ interface is commonly accepted to be related to the so-called "polar catastrophe" [63, 78]. Along the [001] orientation, the interface is at the boundary between a polar $LaAlO_3$ layer with non-polar $SrTiO_3$. As a result, a series of alternating atomic planes, i.e., $La^{3+}O^{2-}$ and $Al^{3+}O_2^{4-}$ are grown on $Ti^{4+}O_2^{-4}$-terminated $SrTiO_3$ substrates. The termination of the $SrTiO_3$ substrate is relevant, as SrO-termination does not yield a 2DES, see Figures 1.10 (a,b). The atomic planes of $LaAlO_3$ consist, therefore, of layers with alternating formal charges +1 and -1 per unit cell, leading to a built-in electric field E. Without reconstruction or uncompensated electric fields, this built-in electric field diverges as the $LaAlO_3$ thickness increases, which is the so-call polar catastrophe. To prevent a diverging potential, 0.5

electrons per unit cell are transfered from the $LaAlO_3$ surface valence band (oxygen 2p bands) to the interface of TiO_2-termined $SrTiO_3$ substrates (Ti 3d states with t_{2g} symmetry), resulting in a conducting interface (Figure 1.10 (c)). The transfer of electrons from the $LaAlO_3$ surface to the interface occurs at a critical thickness of 4 u.c.$\sim$ 1.5 nm, causing an insulator-to-metal transition. In the case of SrO-termination, half a hole (p-type) is required to be transferred and then is counteracted by oxygen vacancies, causing an insulating interface [63] (shown in Figure 1.10 (d)).

The polar catastrophe scenario is valid for crystalline $LaAlO_3$ layers, where the epitaxial arrangement of ions in the lattice structure allows the existence of a built-in electric field. However, it is also found the the interface between amorphous $LaAlO_3$ layers and $SrTiO_3$ substrates can also sustain 2DES [79, 80]. In the case of amorphous interfaces, the mechanism for interface conduction is related to the generation of oxygen vacancies, which dope the interface with carriers [81]. Amorphous $LaAlO_3$ layers are grown at room temperature and low oxygen partial pressures, enabling conditions where oxygen vacancies are formed as n-type doping [81].

Finally, we mention that electronic states at the $LaAlO_3$ surface can influence profoundly the interface properties. As a significant result, a metal to insulator transition can be controlled using voltage applied by conductive AFM on top of $LaAlO_3$ [82]. This metal-to-insulator transition is believed to be related to the disassociation of water which forms protonated surfaces that act as an electrostatic gate that modulates the interface conduction [83–85]. Along the same lines, capping the $LaAlO_3$ surface with metals of different work functions has a strong influence on the interface transport, to the point that the critical thickness for interface conduction can be changed depending on the capping metal [86].

In relation to these observations, we will see in Chapter 3, that photoexcitation of carriers to surface states has a deep impact on the interface properties and is one of the key mechanisms that explain the observed wavelength-dependent time-correlated photoresponses of the $LaAlO_3/SrTiO_3$ interface. Next subsection overviews briefly the phenomenon of persistent photoconductance.

1.3.3 Persistent photoconductance

Persistent photoconductance (PPC) has been extensively investigated since the mid-20th century. A variety of systems exhibit PPC, including III-V semiconductors, such as $Al_xGa_{1-x}As$ [87], $Ga_{1x}In_xN_yAs_{1-y}$ [88] , 2DES at oxide interfaces, such as $NdGaO_3/SrTiO_3$ [89], $LaAlO_3/SrTiO_3$ [67, 90], or graphene [91]. The origin of PPC has been debated in several studies, and sometimes it has been ascribed to the separation of photoexcited electron-hole pairs by macroscopic electric fields, such as those appearing in junctions and surface barriers or microscopic electric fields introduced by impurity atoms with large lattice relaxations [92, 93]. Yet, alternative scenarios have been suggested. One examples is the mechanism of photoexcitation via DX-centers, which has gained wide acceptance [87], and will be described briefly in the following.

DX-centers are point defects, related to insterstitials or ionic substitutions. DX-centers have two possible states that, depending on their charge state, can form either a shallow level with no structural relaxation or a deeper level with structural lattice relaxation around the defect, which traps electrons. As pointed out above, there is a wide consensus that the photoexcitation of trapped electrons in DX-centers is at the origin of persistent photoconductance in many semiconductors. Reported cases are related to anion vacancies (e.g., As vacancy in AlGaAs, oxygen vacancies in ZnO [93]).

The description of DX-centers is facilitated by configuration-coordination (c-c) diagrams [92, 94] as those shown in Figure 1.11. In cc-diagrams, the energy of the electronic states are plotted against the configurational coordinate Q, which, when different from zero, relates to a structural relaxation that deforms locally the lattice, while when Q = 0 refers to an undeformed lattice. Then, in this model, the occupied state which captures an electron is represented as the defect band (DB) with configurational coordinate $Q = Q_s \neq 0$. When an electron is photoexcited leaving behind the DB band, there is a change in the configuration coordinate to $Q = 0$ and, as a result, the lattice relaxation prevents the return of the carrier back to the initial state after photoexcitation, since the electron has to overcome an energy barrier to come back to the original state (Figure 1.11). Consequently, the photoexcited state is long-lived, giving way to a conductance change that persists over extended periods.

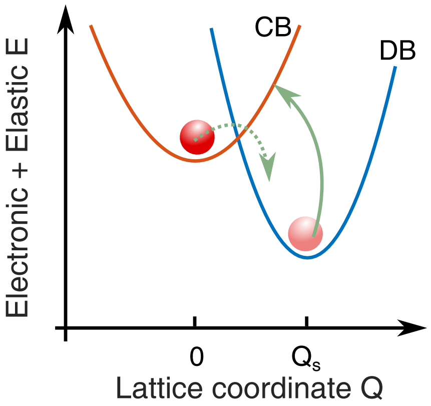

FIGURE 1.11: The total energy of electronic and elastic energies against Q. Curve CB corresponds to the total energy of an unoccupied defect. Curve DB represents the vibrations of an occupied defect which captures an electron, causing a lattice distortion $Q \neq 0$. A photoexcited electron from DB to CB undergoes a large lattice relaxation with a barrier to recover, resulting in PPC.

As described in Chapter 3, there is a second photoexcitation mechanism, relying on the excitation of carriers to surface states via quantum tunneling, which allows to counteract the increased conductivity caused by PPC. The combined action of PPC plus photoexcitation to surface statesis at the origin of the observed wavelength-dependent time-correlated photoresponses at the $LaAlO_3/SrTiO_3$ interface, which pave the way to optical synapses with STDP. More details are given in Chapter 3.

1.4 Outline of the thesis

This chapter has given a brief introduction to artificial synapses. In this Thesis, the physical implementation of artificial optical synapses is based on the persistent photoconductance of the $LaAlO_3/SrTiO_3$ interface. The following chapters present the studied methods, discussing some results and providing explanations, which are organized as follows:

Chapter 2 describes the methods of device fabrication. Samples of epitaxial and amorphous $LaAlO_3$ films are grown on $SrTiO_3$ substrates by pulsed laser deposition, and devices are defined with lithography. The measurements of electric transport under illumination with different visible wavelengths are carried out by advanced programmable spectrometers at the confocal microscopy system. Chapter 2 ends with a brief description of simulations of artificial neuron networks using the Brian simulator [95].

Chapter 3 presents the wavelength-dependent time-correlated photoresponses of the epitaial $LaAlO_3/SrTiO_3$ interface, and a physical explanation is provided to describe these observations.

A Green's function formalism is used to interpret the physical processes, providing insights into the observed asymmetric photoexcitation.

Chapter 4 explores time correlated photoresponses down to the millisecond regime at the epitaxial $LaAlO_3/SrTiO_3$ interface. The wavelength-sensitivity time correlations are proved by a series of detailed experiments and data analysis. Based on the data of the observed novel PPC, simulations of neural networks emulating spatial memory and navigation maps inspired from neurobiological systems is performed with the Brian simulator. We suggest that the observed photoresponse paves the way to an optical implementation of optical artificial spiking neuron networks.

Chapter 5 investigates the sensitivity to the light stimuli at the amorphous $LaAlO_3/SrTiO_3$ interface. As the amorphous $LaAlO_3/SrTiO_3$ interface is getting more insulating from conducting state, the relative photoconductance increases abruptly, even to 1000% under violet light. On the basis of the insulating state, the photoconductance profoundly improves the sensitivity to the light with intensity decreasing to as weak as the sunlight environments, which is of potential interest for the sensor application.

Chapter 6 provides perspectives and outlook on the physical mechanisms of the correlative 2DES and the potential applications on the artificial synapses. The multiple photo-excitation processes provide insight into the distinct properties found in the complex oxide interfaces.

Our brain is definitely as complex as our cosmos. As Carl Sagan said, 'the cosmos is within us. We are made of star-stuff. We are a way for the universe to know itself.' We are also a way for overcoming the limitation of modern computer or other technology and science. When we are looking upon the star, we are looking into ourselves as well. When we feel confused, why not focus on our inner world, including the miracle organic system and unique thought. Because --

We are living in the cosmos with imaginary and curiosity,
Cosmos is spiraling inside us within brain and body.
Creating stars, subsequently, Cosmos created us with star dust,
Exploring Cosmos, can we construct a cosmos, and us?
Our cosmos is complex and elegant,
                coordinating with sparkle body and dark matter.
Our brain is sophisticated and intelligent,
                operating with spiking neuron and hidden consciousness.
Cosmos here, therefore we are being.
We here, therefore cosmos is seeing.
Cosmos is unbounded, we are unlimited.

Chapter 2

Methods: experiments and simulations

To analyze the photoconductive response of the $LaAlO_3/SrTiO_3$ interface and its potential application to artificial synapses, we have prepared a variety of samples and performed on them a series of phototransport experiments that have been analyzed and simulated. This chapter will present the sample fabrication, optical characterization, theoretical background and simulations of the time-dependent photoconductance response.

This chapter starts with the description of sample fabrication in Section 2.1, including deposition techniques in Subsection 2.1.1 and lithography in Subsection 2.1.2. Then the optical characterizations are carried out (see Section 2.2). Finally, simulation is described succinctly in Section 2.3.

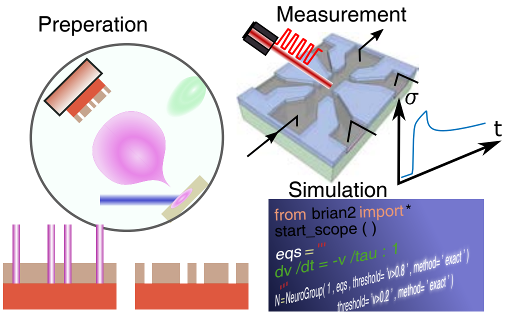

```
from brian2 import *
start_scope ( )
eqs = '''
dv /dt = -v /tau : 1
'''
N=NeuroGroup( 1 , eqs , threshold= 'v>0.8 ' , method= ' exact ' )
                threshold= 'v>0.2 ' , method= ' exact ' )
```

2.1 Sample fabrication

The measurements of the electric transport and photoconductance were carried out in Hall-bar geometry [96, 97]. Alternatively, other geometries were also defined to measure the capacitance of the $LaAlO_3/SrTiO_3$ interface, using the interface as one of electrodes [98–101]. With this purpose, the sample fabrication encompassed a series of techniques including thin film deposition and lithography. We start describing the pulsed laser deposition (PLD) for the growth of $LaAlO_3/SrTiO_3$, metal evaporation for the deposition of metallic layers and atom layer deposition (ALD) to deposit amorphous AlO_x as a hard mask to define the devices. Finally we present the lithography process.

2.1.1 Deposition

Pulsed laser deposition

Pulsed laser deposition is a physical vapor deposition (PVD) technique that uses a high-power laser to vaporize a ceramic target. In our lab, a 248 nm KrF excimer is employed to ablate a target with the required chemical composition located in the chamber with controllable gas pressure and temperature. Then the material plume resulting from the ablation is deposited on the substrate, as shown in Figure 2.1.

For the preparation of the $LaAlO_3/SrTiO_3$ interfaces we benefited from the collaboration with Dr. F. Sanchez (ICMAB). Two types of interfaces were grown, depending on whether $LaAlO_3$ films were grown epitaxially or amorphously on top of as-received $SrTiO_3$ substrates. As discussed in Section 1.3.2, the formation of 2DES in epitaxial films is driven by an electronic reconstruction caused by electrostatic boundary conditions, whereas for amorphous films the mobile carriers come from oxygen vacancies. We will see that these two different mechanisms for conduction have important consequences on the properties of the photoconductive response, an issue that is discussed in detail in Chapter 3.

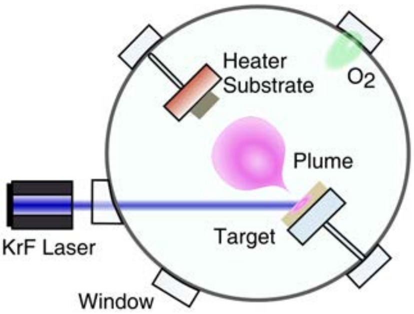

FIGURE 2.1: Sketch of pulsed laser deposition setup. The target material is ablated by laser and the material plume is deposited on the substrate.

For both epitaxial and amorphous films, the growth was done by pulsed laser deposition under oxygen partial pressure $P_{O_2} = 10^{-4}\,mbar$, substrate-target distance 55 mm, repetition rate 1 Hz, pulse energy about 26 mJ, fluence 1.5 J/cm^2. The thickness of the films was controlled by varying the number of pulses. For that purpose, a calibration sample of thickness about 50 nm was grown, for which the thickness could be established by X-ray reflectometry. Epitaxial films were deposited at a temperature $T = 725\,^oC$ and cooled down at 15 $^oC/min$ in oxygen rich atmosphere ($P_{O_2}200\,mbar$, maintained at 600 ^oC for 1 hour and then cooled down to room temperature at 15 $^oC/min$) to minimize the formation of oxygen vacancies, which provide an extrinsic contribution to transport in epitaxial $LaAlO_3/SrTiO_3$ interfaces [66, 81].

Similar growth conditions were used for amorphous $LaAlO_3/SrTiO_3$ interfaces except for the deposition temperature. In this case, the $LaAlO_3$ films were grown on top of the $SrTiO_3$ substrates at room temperature, which precludes the formation of epitaxial films, and forms $LaAlO_3$ amorphous layers. The low-pressure conditions ($P_{O_2} = 10^{-4}\,mbar$) drive the formation of oxygen vacancies that act as donors and generate the carriers that form the conducting layer at this interface [102].

As discussed in Section 1.3.2, the formation of 2DES at epitaxial and amorphous interfaces is driven by different mechanisms. This observation leads to important properties that are used for device fabrication. In particular, under rich-oxygen atmospheres and high enough temperatures, the vacancies formed at the amorphous $LaAlO_3/SrTiO_3$ interface are annealed away and the samples become insulating. On the contrary, the 2DES at epitaxial layers cannot be annealed away. This property enables using annealed amorphous $LaAlO_3$ as a hard mask to isolate electrically Hall-bar devices to measure the electric transport in epitaxial $LaAlO_3/SrTiO_3$. For Hall bars defined in amorphous $LaAlO_3/SrTiO_3$, photoresist or amorphous AlO_x was used as a hard mask to isolate the devices (details about device fabrication are given in Section 2.1.2).

Metal evaporation

Metal/$LaAlO_3$/$SrTiO_3$ structures were prepared to measure the capacitance and also to carry out deep-level transient spectroscopy (DLTS) in collaboration with Dr.Laurence Mechin (GREY-CNRS, University of Caen, France). For that purpose, a variety of metals, including Au and Pt, were grown on the surface of $LaAlO_3$ forming top electrodes. The metal deposition was performed by using thermal evaporation or electron-beam evaporation, which both are physical deposition methods with high quality vacuum system, as seen in Figure 2.2.

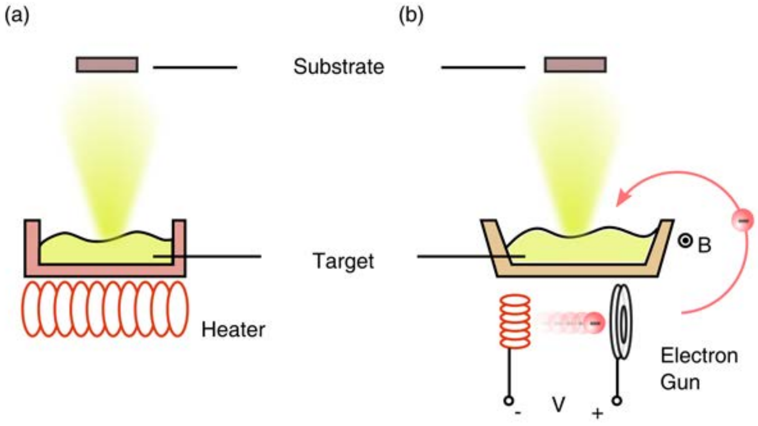

FIGURE 2.2: Sketch of metal deposition through (a) Resistance evaporation and (b) e-beam evaporation.

The Auto 306 Vacuum Coating system was employed to perform thermal evaporation which is a simple and cost-effective deposition method based on heating the target to be evaporated condensing on the substrate in a high vacuum chamber. In contrast, electron-beam evaporation exploits the high kinetic energy of electrons colliding with the target materials, so that their energies are transferred to thermal energy to evaporate the material. In the process, electrons are generated in high vacuum by an electron gun and are accelerated by potentials in the order of $10\,kV$ then are injected into the target located in a crucible so that the material is gaining the thermal energy to the melting point, as a result, the material is evaporated and coats the substrate.

Atomic Layer Deposition

Atomic Layer Deposition (ALD) is a chemical deposition technique that uses discrete pulses of chemical precursors to grow films homogeneous over large areas (more than $5 \times 5\,cm^2$). Deposition of aluminum oxide (AlO_x), using trimethyaluminum (TMA) and water by ALD [103, 104] was used as an alternative to the amorphous $LaAlO_3$ to define the hard mask used to isolate different Hall bar devices of epitaxial $LaAlO_3$/$SrTiO_3$.

Firstly, pulses of TMA were injected and delivered into the substrate (polydimethylglutarimide (PGMI) S1813 photoresist (PR)/$SrTiO_3$ in our case) with native hydroxyl layer ($*OH$, * denotes the surface) generated by pulses of O_3, as seen in Figure 2.3 (a) where the TMA combine with $*OH$ to form bimethylaluminum bound to oxygen ($O - *Al(CH_3)_2$) and methane (step (b)). Then N_2 was pulsed to purge the excess TMA and methane when the surface is saturated with $O - *Al(CH_3)_2$ (step (c)). In the next step (d) , the counter precursor H_2O was pumped into the reactor to forms $*Al - OH$ and then was purged by N_2 again (step (e)). The circle from step (b) to step (e) was completed and repeated until the desired thickness by controlling the number of cycles (Figure 2.3 (e)), e.g., the AlO_x with 50 nm corresponding to about 625 cycles.

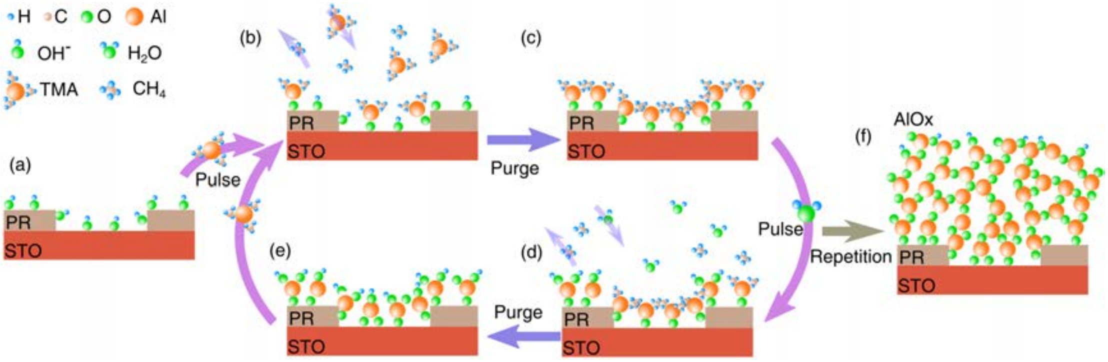

FIGURE 2.3: Sketch of atomic layer deposition. (a) substrate with patterned phoresist/STO, (b) pulsing of TMA , (c) purging of excess TMA and methane, (d) pulsing of H_2O , (e) purging of excess H_2O and methane, and (f) repeating ALD cycles.

The deposition of AlO_x should be conducted in a temperature lower than the stability temperature of our photoresist (S1813). However, there is a compromise, since if the temperature is too low, the reaction is incomplete, so that vapor deposition may occur causing poor quality of AlO_x film. In collaboration with Dr. Mariona Coll (ICMAB) we carried out a study to optimize the growth of AlO_x constrained the aforementioned conditions, and found that the best compromise is to deposit AlO_x at a temperature of 100^oC and the photoresist should be treated with post-heating at $95 - 100^oC$ for $5min$ to prevent volatilizing the photoresist during growth of AlO_x film.

2.1.2 Lithography

Devices with Hall-bar geometry were fabricated through optical lithography using the procedure shown schematically in Figure 2.4. First of all, a layer of polydimethylglutarimide (PGMI) S1813 photoresist (PR) was spin-coated on the surface of as-received $\mathrm{SrTiO_3}$ crystals (Crystec Gmbh) forming a PGMI layer of thickness 1100 nm at the spin-coating speed of 5000 rpm and angular acceleration 0.7 s, which was then soft-baked at 95^oC to solidify the photoresist. Subsequently, a Micro-Writer ML3 lithography system (Durham Magneto Optics Ltd.) was used to expose the PGMI layer by writing directly on it the Hall bar pattern with a 1 μm laser spot of wavelength $\lambda = 385\,nm$ and energy fluence 200 mJ/cm^2 (Figure 2.4 (a)). The exposed areas were then dissolved away by a Shipley MF319 developer to form the Hall bar boundary, leaving behind the unexposed resist with the shape of the Hall bar as shown in Figure 2.4 (b). Then the amorphous $\mathrm{LaAlO_3}$ was deposited by PLD or AlO_x by ALD (Figure 2.4 (c)). In the final stage of lithography, a lift-off was done with hot acetone to remove the remaining resist together with the portion of amorphous $\mathrm{LaAlO_3}$ on top of it (Figure 2.4 (d)). The gap left behind was then filled up by growing an epitaxial $\mathrm{LaAlO_3}$ layer of various thicknesses (2.4 (e)).

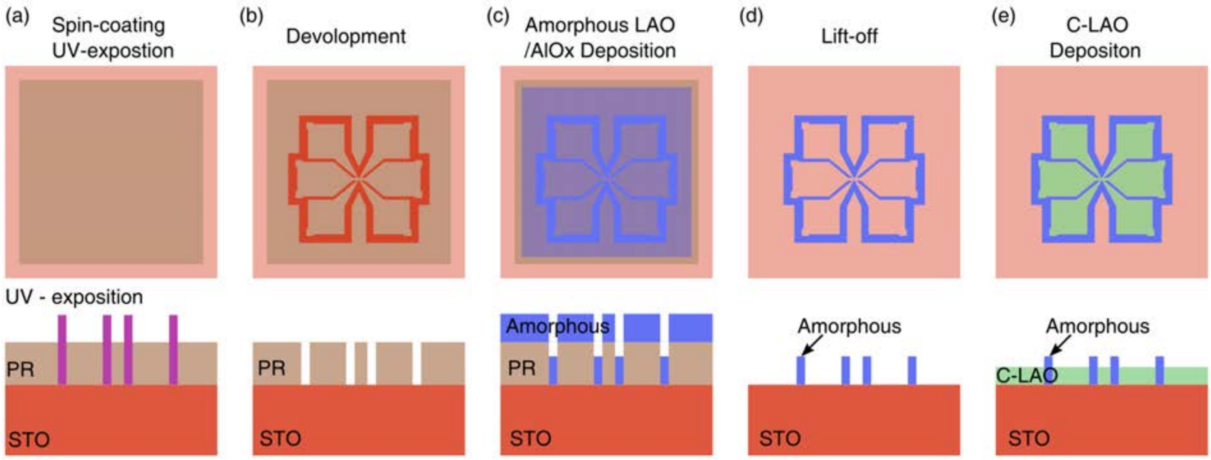

FIGURE 2.4: Schematics of the lithography process. The upper panels show a top view, while lower panels depict cross-sectional views: (a) spin-coating of photoresist and UV-exposition, (b) development of photoresist, (c) deposition of amorphous materials, (d) lift-off of photoresist and (e) deposition of epitaxial $LaAlO_3$ film.

The Software Clevin was used to design the patterns. For typical Hall-bar devices the length and width of the bridge are about 30 μm and $4, 6, 8, 10$ μm, respectively. The size of the pad is around 800 $\mu m \times 800$ μm, which is easy to do wire-bonding (seen in Figure 2.5). These devices are used to measure the electric transport and photoconductance, which are presented in the next section.

2.2 Photoresponse measurement

The photoconductance was measured in Hall-bar devices using a confocal microscope (CFM) to illuminate locally the Hall bar with different wavelengths. In the following, we will describe also the instrumentation used to characterize the transport properties and to control the output power of the laser used in the CFM. The whole setup used for the measurement of the photoconductance is shown schematically in in Figure 2.5. In the next subsection we will describe the confocal microscope and the light source used in the experiments of photoconductance.

2.2.1 Confocal microscopy system

Confocal microscopy (CFM) can reach the fundamental limit of optical resolution by blocking the out-of-focus light and detecting only in-focus light in the image formation [105]. CFM is mainly used to lead the beam to focus over the Hall bar channels. As an illustration, Figure 2.5 (a) shows a picture of one of the measured Hall bars, with chanel witdh and length of 10 and 30 microns, respectively. With the zoom lens and CCD camera the beam is roughly located on sample mounted on the positioner controlled by a piezo scanner. Then the focus is adjusted along the out-of-plane direction by minimizing the beam spot under monitoring by the CMOS camera. Afterwards, while the positioner is scanning in plane, the photodetector measures the intensity of the reflected light at each point. Figure 2.5 (b) shows the image of hall-bar by CFM

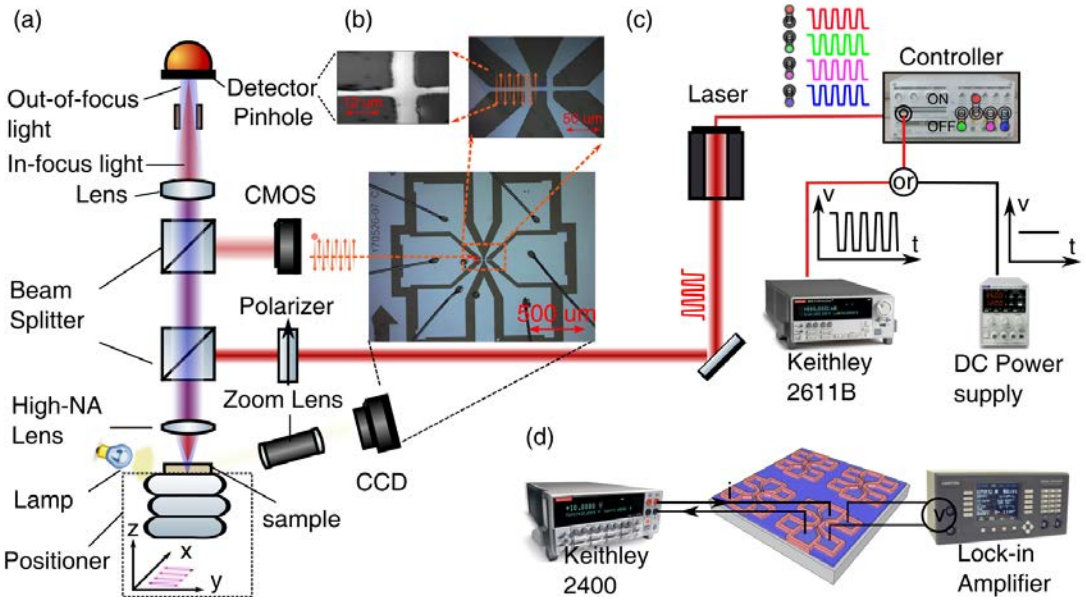
(a)
Out-of-focus light
In-focus light
Lens
Beam Splitter
High-NA Lens
Lamp
Positioner
z
x
y
Detector Pinhole
CMOS
Polarizer
Zoom Lens
CCD
sample
(b)
12 um
50 um
500 um
(c)
Laser
Controller
ON
OFF
or
V
t
Keithley 2611B
DC Power supply
(d)
Keithley 2400
V
Lock-in Amplifier

FIGURE 2.5: Schematics of photoresponse measurement: (a) confocal microscopy system used to locate the sample and guide light with micron-scale spot focus on the surface of sample. (b) Images of a typical Hall-bar device where the photoconductance is measured. (c) The laser used to illuminate the samples is controlled by an eletrometer (Tektronix co. Kethley 2611B for pulse or Aim-TTi co. CPX400SA for DC Power Supply) . In the measurements, the current was applied by Keithley 2400 sourcemeter, while the voltage is measured by a lock-in amplifier (AMETEK co. Model 7270) used as a DC voltmeter with millisecond precision in (d).

in the top-left panel and the photo of the device by optical microscopy in the bottom and its magnification in the top-right.

2.2.2 Controllable Laser source

For the illumination of the samples we used a SpectraTec X system, which includes four lasers of wavelengths 405, 450, 520 and 638 *nm* (Figure 2.5 (c)). In this equipment, the irradiance of the light at the source output can be regulated electronically, for instance, using a CPX 400SA 420wDC power supply (Aimtti Co.). The light can be controlled by voltage pulses supplied by a Keithley 2611B instrument. The width and periodicity of the train of pulses can be regulated down to the limit of 5 μs with the script written by Keithley TSP Express software.

Laser Irradiance regulation

In order to study photoresponse to varying values of irradiance, the power of light reaching the sample has to be estimated when the light goes through the whole optical path. For this purpose, the relation between the real power reaching the sample through the CFM system and the laser power at the output of the source is determined as shown in Figure 2.6. More specifically, the irradiance can be adjusted by an electrometer (Kethley 2611B) according to the tabulated voltage values to the irradiance at each wavelength at the exit of the laser source, which is provided by the manufacturer. The first step is to measure the intensity of the signals reaching the photodetector directly from the laser source, regulated at different power outputs (Figure 2.6 (a)). The data measured at wavelength 638 nm is plotted in (Figure 2.6 (d)). Such a linear relation between the detector signal (V_{PD}) and the power density at the exit of the laser source can be used to extrapolate the real irradiance that reaches the sample through the CFM system (Figure 2.6(c)) and the result data is shown in Figure 2.6(e). From these experiments we found that the real power density reaching the samples is almost almost 1/10th of the irradiance that comes out directly from the laser source, see Figure 2.6 (f).

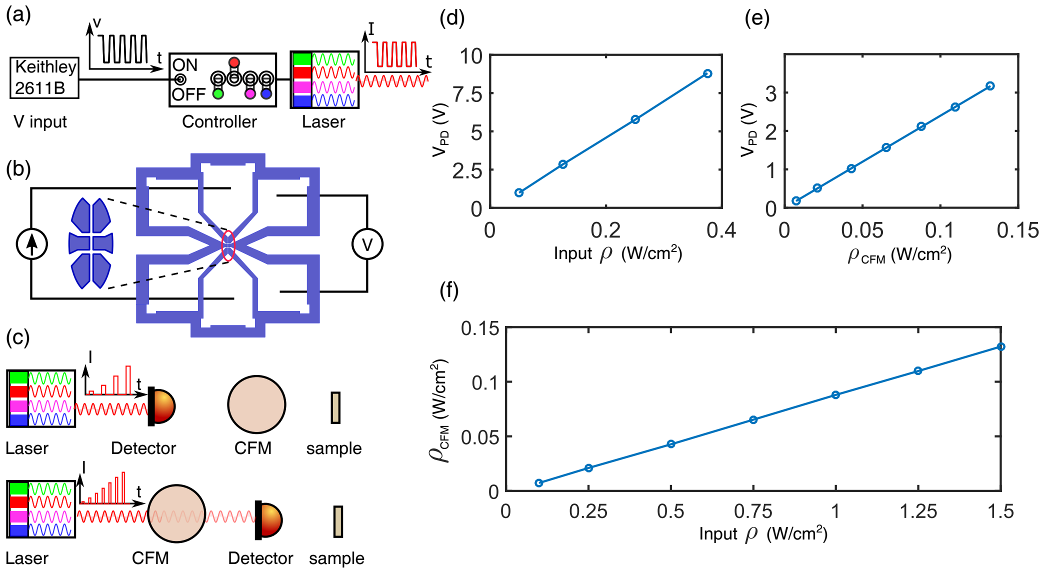

FIGURE 2.6: (a) Schematic representation for the generation of optical pulses. (b) Idem for transport measurements of Hall bars. (c) Schematic representation of the measurement of the real irradiance reaching the sample. (d) Relation between the detector signal and input light irradiance coming directly from the laser source at 638 nm. (e) Detector signal when light goes through the CFM lens system. (f) From these experiments we found that the real power density is almost 1/10 of the irradiance of the light that comes out directly from the laser source.

Laser bandwidth

The light at the output of the laser source is not perfectly monochromatic. Instead, the intensity is distributed within a certain bandwidth, in a range of wavelengths around a central value. We determined the output bandwidth of the laser sources for every wavelength ($\lambda = 405, 450, 520$ and 638 nm) using a StellarNet BLACK-Comet concave grating spectrometer. The results of these measurements are shown in Figure 2.7 (a). The bandwidths defined by the full width at half maximum (FWHM) determined by this procedure are shown in 2.7 (b) for the four wavelengths in the visible. This allows to calculate the values of the illuminance in units of $W \cdot nm^{-1} \cdot m^{-2}$, which were obtained after dividing the irradiance measured as described above by the FWHM obtained from these measurements.

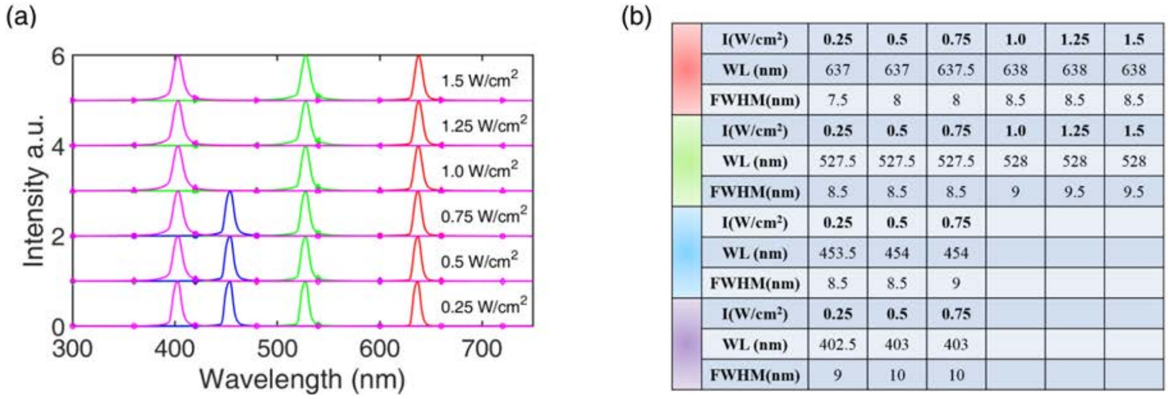

🟥	**I(W/cm²)**	**0.25**	**0.5**	**0.75**	**1.0**	**1.25**	**1.5**
	WL (nm)	637	637	637.5	638	638	638
	FWHM(nm)	7.5	8	8	8.5	8.5	8.5
🟩	**I(W/cm²)**	**0.25**	**0.5**	**0.75**	**1.0**	**1.25**	**1.5**
	WL (nm)	527.5	527.5	527.5	528	528	528
	FWHM(nm)	8.5	8.5	8.5	9	9.5	9.5
🟦	**I(W/cm²)**	**0.25**	**0.5**	**0.75**			
	WL (nm)	453.5	454	454			
	FWHM(nm)	8.5	8.5	9			
🟪	**I(W/cm²)**	**0.25**	**0.5**	**0.75**			
	WL (nm)	402.5	403	403			
	FWHM(nm)	9	10	10			

FIGURE 2.7: (a) Measurements of the spectral distribution of intensity collected from the lasers at every wavelength and for different irradiance values at the exit of the source. From these experiments, the output bandwidth was determined, shown in the table of panel (b). FWHM is the full width at half maximum and WL is wavelength and $I(W/cm^2)$ is the irradiance at the exit of the laser source.

Measurements under low irradiance

The achievement of small values of irradiance on the samples cannot be done by controlling the laser source electrically since a threshold voltage is necessary to activate the laser. Therefore we attenuated the intensity by adjusting the orientation of a polarizer at the exit of the laser source (Figure 2.8) .

We used a similar protocol to calibrate the irradiance that reaches the sample after attenuation with a crossed polarizer. Thus, under direct illumination with a laser $\lambda = 450\,nm$ the signals are captured by the detector after direct illumination of the photo-sensor with a laser beam of different irradiance values at the output source in the range $P_w = 0.25 - 0.75 \times 10^3\ W \cdot nm^{-1} \cdot m^{-2}$ (Figure 2.8 (a)). Afterwards, the beam with almost minimum irradiance controlled by electrometer goes through a polarizer. Figure 2.8 (c) shows the voltage recorded by the photodetector after sensing light pulses of blue light ($\lambda = 450\,nm$) of irradiance $P_w = 0.75 \times 10^3 W \cdot nm^{-1} \cdot m^{-2}$ at the exit of the laser source for different settings of the polarizer within the range of angles $\theta = 0 - 80^o$.

The data displayed in Figure 2.8 (b) (showing the linear relation between the voltage setting V_set at the laser source and irradiance $P_{w,set}$ tabulated by the manufacturer) was fitted to a linear dependence as:

$$P_{w,set} = k_{set} \times V_{set} + \rho_0 \tag{2.1}$$

Where $k_{set} = 3694.1$ and $\rho_0 = 114.1$.

We then proceeded to use the value of k_{set} to obtain a relationship between the irradiance and the voltage V_{PD} sensed by the photodetector:

$$P_w = k_{PD} \times V_{PD} + \sigma_0 \tag{2.2}$$

from where we obtained $k_{PD} = 2058.8$ and $\sigma_0 = 870.6$.

Next, the values of V_{PD} sensed at the photoconductor where plotted against the different orientations of the polarizer (θ) (Figure 2.8 (c)), so that a relationship could be established between irradiance and the polarization setting:

$$P_w = a \times cos(\theta)^s + b \tag{2.3}$$

where $a = 7551$, $s = 2.1$ and $b = 839$.

Eq. 2.3 was used to calculate the real irradiance P_w for polar orientations of the polarizer ranging in the interval $\theta = 0 - 80^o$. This procedure allowed us to vary the illuminance in the range $P_w \approx 2.5 - 15000\, W \cdot nm^{-1} \cdot m^{-2}$.

2.3 Simulations: Brain simulator

In this Thesis the simulations of neuromorphic devices were performed using the Brian simulator [95, 106]. As mentioned in Chapter 1, some of the neurocomputational approches use spiking neural networks. This section describes briefly some concepts and functions of biological neurons (Subsection 2.3.1). Modules are developed in Brian simulator to mimic some of the functions of biological neurons (subsection 2.3.2). Finally, a simple example (subsection 2.3.3) is given to illustrate the simulation performed in Brian (a simulation based on the data measured from epitaxial $LaAlO_3/SrTiO_3$ interface is exhibited in Chapter 4).

2.3.1 Biological neurons

As we know, neurons conduct information using electrical signals carried by ions along axons, which unavoidably confront leakages over long distances. To overcome these constraints,

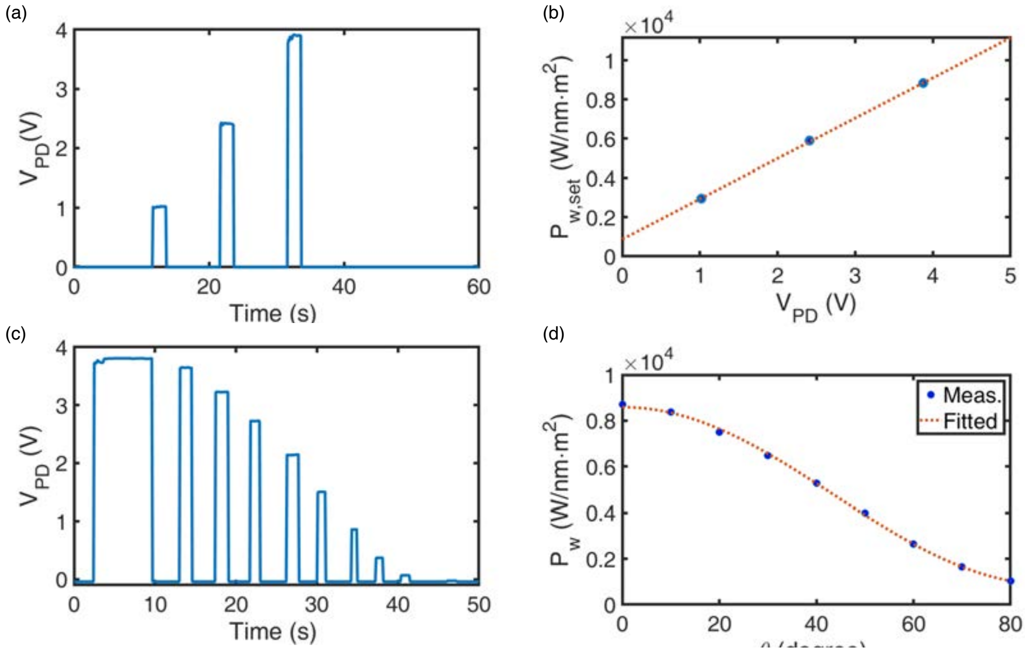

FIGURE 2.8: (a) Signal as measured by the photodetector for direct illumination with a laser ($\lambda = 450mn$) of $P_w = 0.75 \times 10^3 W \cdot nm^{-1} \cdot m^{-2}$ at the exit of the laser source for different settings of the polarizer within the range of angles $\theta = 0 - 80^o$. (b) Values of irradiance as a function of the angle of the polarized.

excitable membranes are able to generate and conduct **action potentials** (also called **spikes**) for long-distance neural communications. Spikes represent sudden, brief changes in **membrane potential** which is the voltage difference between the inside and outside of the neural cells. In the resting neuron without any action potential, the inside surface of the membrane has a negative charge with respect to the outside, resulting in a **resting membrane potential** $Vm \approx -65\,mV$. Upon the arrival of a given stimulus, positive ions cross the membranes in specific channels, causing polarized membranes to be less negative. When the depolarization achieves a critical level – **threshold**–, the membrane will generate an action potential. Once a spike is fired, another spike has to wait for a **refractory period** to be fired (Figure 2.9).

Neurons are connected through synapses through which presynaptic neurotransmitters are conveyed to the postsynaptic neurotransmitter receptors. If neurotransmitters depolarize or hyperpolarize membranes, the membrane potential increases toward or decreases away from threshold for generating action potentials, which is said to be **excitatory** or **inhibitory**, respectively. An **excitatory postsynaptic potential (EPSP)** or **inhibitory postsynaptic potential (IPSP)** means that the presynaptic release of neurotransmitter causes the postsynaptic membrane depolarization or hypolarization, respectively [107].

2.3.2 Description of basic instructions of the Brian simulator

Here we introduce a few basic concepts and syntax related to the simulations using Brian, such as the definitions of the neuron network and synapse. More descriptions can be find in Brian simulators website [95, 106].

Neuron network

Brian simulator allows to define differential equations that characterize the dynamical behavior of spiking neurons [108–110]. A first parameter is the membrane potential related to synaptic plasticity. As described above, once the membrane potential of a given neuron is above a given threshold, a spike is generated by that neuron. Another relevant parameters are the time constants τ_m, τ_n ... that describe the accumulation or decay of membrane potential with time, which correspond to time evolution of the photoconductance of the 2DES at the $LaAlO_3/SrTiO_3$ interface.

In the Brian simulator, neuron networks can be built by commands such as $NeuronGroup$, which represents a group of neurons that share properties defined by same equations and same conditions to emit spikes. The $NeuronGroup$ command has a syntax of the type neurons like: *neurons = NeuronGroup(N, eqs_neurons, threshold=′v>vt′, reset=′v = vr′, method=′exact′)* , where N is the number of the neurons; *eqs_neurons* is the differential equations that describe the dynamics of membrane potential, e.g., *eqs_neurons = ′′′ dv/dt = (I-v)/tau : 1 I : 1 tau : second ′′′*, where tau is the characteristic time of the dynamics, for which a unit has to be defined (e.g., *second*); *threshold* and *reset* are used to define the condition for the emission of spikes and then reset the membrane potential. The command also can add *refractory = 10*ms* to define a refractory time where the neurons cannot fire a spike for a certain period, which in biological neurons is typical of order $10\,ms$.

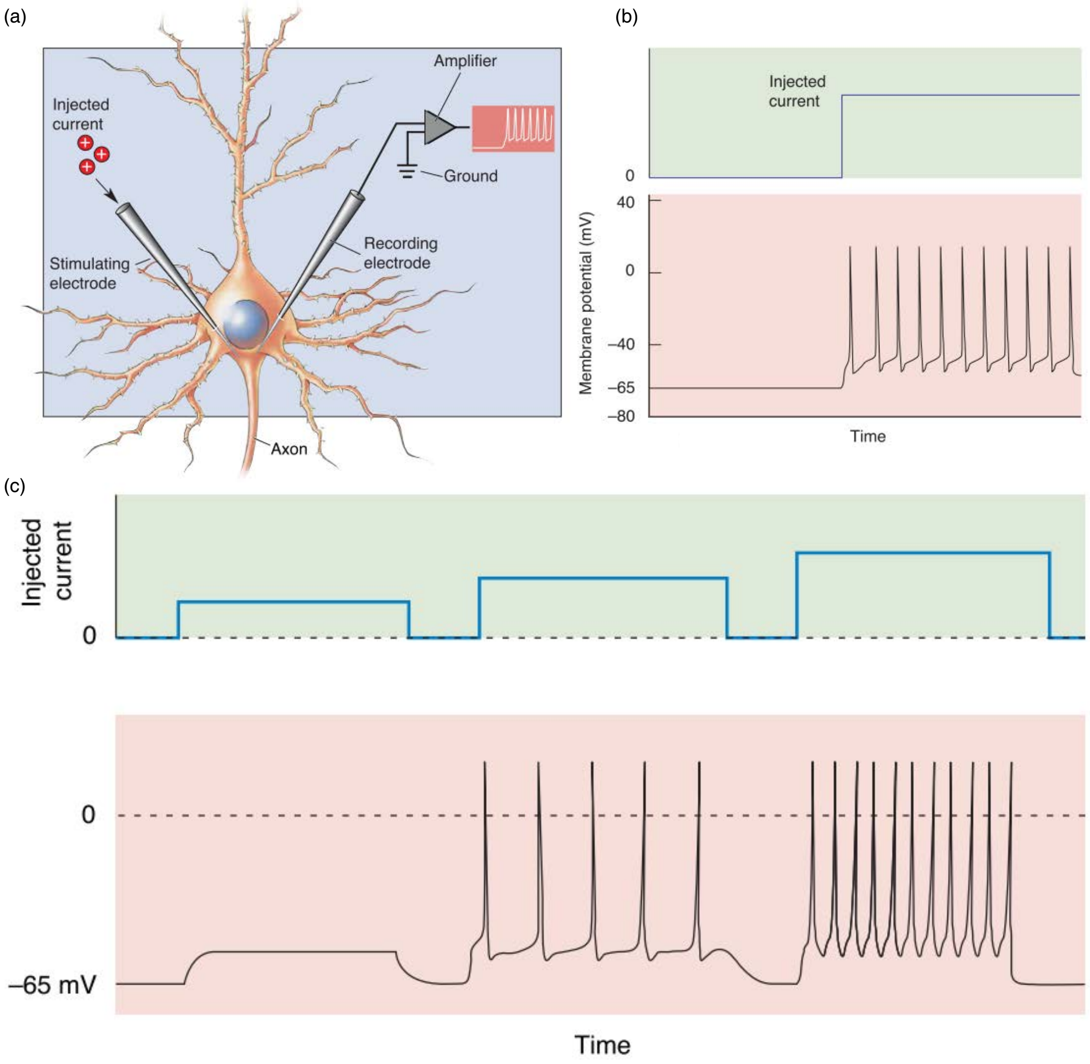
(a)
Injected current
Amplifier
Ground
Recording electrode
Stimulating electrode
Axon
(b)
Injected current
0
40
0
−40
−65
−80
Membrane potential (mV)
Time
(c)
Injected current
0
0
–65 mV
Time

FIGURE 2.9: (a) Schematic illuminations of the injecting positive charge into a neuron and the measuring the membrane potential. (b) Membrane is depolarized sufficiently to fire action potentials. (c) Action potential depends on the level of depolarization (**adapted from Ref. [107]**).

Synapse

Brian also contains instructions that define the characteristics of synapses. The syntax is of the type like *S = Synapses(Npre, Npost, on_pre=v_post += 1*mV, on_pre=v_post += 1*mV)* , where the parameters *Npre* and *Npost* are the pre- and post- Neurongroups defined previously. The following statements define the actions at the defined conditions, here, *on_pre=v_post += 1*mV* means that when pre-neurons emit a spike, the variable of post-neurons increases by 1 mV, similarly, *on_pre=v_post += 1*mV* means the pre-neurons spike causes a increase in the post-neurons.

After building a neuron network, synapses can be connected by instructions like *S.connect (i=2,j=3)*, which means that a synapse is created between the second neuron of the pre-neurons group and the third of post-neurons group. The condition of connection can be complex and probabilistic by adding a *p* argument like *S.connect(i=2,j=3,p=0.1)*.

During run (time) of a Brian code, the state of the neural network can be tracked by *State-Monitor* to monitor the neuron or synapse variables and information about generated spikes information by *SpikeMonitor*. After running the codes, the relative values of the stats monitored can be obtain.

2.3.3 An example of Brian simulation

In Brian simulations, special attention has to be paid to the consistency of the used units. All variables or equations have to be expressed in physical units that enforce dimensional consistency. In the following, we give en example of a Brian simulation that uses some parameters extracted from photoconductance experiments. In particular, we consider the excitation of a post-synaptic neuron as a function of synaptic changes made by incoming pulses of light. The input optical pulses are formally considered as spikes of a pre-synaptic neuron which, consequently, modulate the synapse connecting pre- and post-synaptic neurons. The changes of synaptic weight induced by light pulses are extracted from experiments of photoconductance, where the relative photoconductance is defined as $(\sigma_{ph}/\sigma_0(\%) = \delta(\sigma - \sigma_0)/\sigma_0 \times 100\%)$. Box 2.1 shows the Brian code used to model a firing post-synaptic neuron that spikes regularly as a function of the pulsed photoexcitation (Figure 2.10).

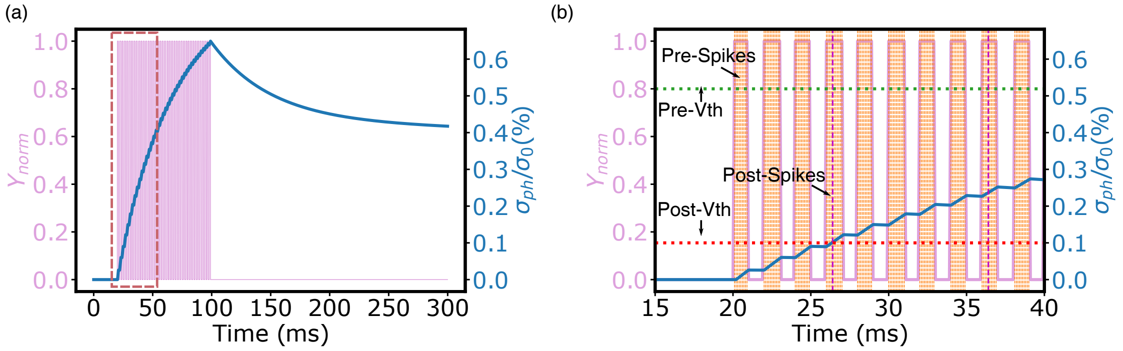

FIGURE 2.10: Simulation of persistence photoconductance based on photo-spikes: (a) The input optical pulse acting as pre-synaptic spikes with 2 ms refractory period and 1 : ms width per pulse, and the threshold value is set as 0.8. The summed spikes causes increase in the photoconductance of the post-synaptic neurons, and the enhancement decreases slowly after termination of the spikes. (b) is the magnification of the square in (a). The post-synaptic threshold value is set as 0.1, when the increasing photoconductance surpasses the threshold, post-spikes are emitted and after a refractory period 10 ms repeat again til the photoconductance decreasing below the post-threshold.

Section #1 in Brian Code 2.1 contains the instructions that generate the pulses with the same width and frequency as the real optical pulses used in experiments. The parameter P defines the periodicity of pulsing; *t_on* and *t_off* define the time that light is switched on and off, respectively, thus giving the range of the pulse train *r = 20 - 100 ms*; The expression *Y =t % P < r*ms : 1* means the remainder is taken from the evolving time $t(ms)$ divided by $P = 2\,ms$ during the pulse train *r = 20 - 100 ms*, yielding the train of pulses and width of each pulse is 1 *ms*.

Section #2 in Code 2.1 contains the instructions that simulate the synaptic changes triggered by the optical pulses. The synaptic weight is linked to the changes of conductances induced by light expressed by $\delta\sigma_{ph}/\sigma_0(\%)$. The rising time of $(\delta\sigma_{ph}/\sigma_0(\%))$ is ruled by two time constants, *tau_1* and *tau_2* which are extracted from the photoconductance experiments. In particular, the rising time is modeled by a bi-exponential function [90]: $s = s_0[aexp(-t/\tau_1) + (1-a)exp(-t/\tau_2)]$, where, s is the relative photo-conductance $\sigma_{ph}(t)/\sigma_0(\%)$, s_0 is the initial value $\sigma_{ph}(t=0)/\sigma_0(\%)$. The last part of section #2 of Box 2.1 defines the relaxation decay time of photoconductance after the light is switched off, which is also inferred from experiments.

Finally, Section #3 of Code 2.1 contains the instructions that define the set of pre- and post-synaptic neurons and the synapses that connect them, with the rules that udpate the synaptic weigth after the pre-synaptic neuron spikes.

```
from brian2 import *
start_scope()
#—— pre−neruon setting——
P = 2 *ms      # period
t_on = 20 *ms    # light on
t_off = 100*ms      # light off
# pulse generation
eqs1='''
r = t<t_off and t>t_on :1
Y =t % P < r*ms : 1
'''
#—— post−neruon setting——
a = 0.6
w = 0.525
tau1 =50*ms
tau2 =5 *second
eqs2 = '''
ds1/dt = −s1/tau1 :1
ds2/dt = −s2/tau2 :1
s = s1+s2:1
'''
#—— weight setting——
tau3 = 100*ms
weight='''
w: 1
'''
#—— neuron defined——
# when light is switched on, the spikes are firing per 0.1 ms
Pre = NeuronGroup(1, eqs1, threshold='Y>0.8', method='exact')
Post = NeuronGroup(1, eqs2, threshold='s>0.1',refractory=10*ms,method='exact')

#—— Synapes——
# when a spike is produced by pre−neuron, the parameter like weight, amplitude are updated.
S = Synapses(Pre, Post, weight, on_pre='''
s1_post += w*0.525
s2_post += w*(1−0.525)
w = 0.004*exp(−t/tau3)
''')
S.connect(i=0, j=0)
#——states and spikes monitor——
```

```
M1 = StateMonitor(Pre, 'Y', record=t_offue)
M2 = StateMonitor(Post, 's', record=t_offue)
Sp = SpikeMonitor(Pre)
#--- Run and plot---
run(300*ms)
figure
plot(M1.t/ms, M1.Y[0], label='Input')
plot(M2.t/ms, M2.s[0], label='Output')
```

CODE 2.1: Simulation of photoconductance under a train of pulses

Chapter 3

Photoinduced tunable carrier accumulation and depletion in a quantum well

---

Here we show that the epitaxial $LaAlO_3/SrTiO_3$ interface exhibits photoresponses that depend on the time order of the arrival of optical pulses of different wavelengths. As a result, the conductance is altered by sequences of pairs of pulses, so that its value with respect to single-pulse excitation can increase or decrease depending on the relative arrival time of photons of different frequencies. In this chapter, we give a physical explanation of the observed photoresponse, which, as developed in Chapter 4, paves the way to the use of the $LaAlO_3/SrTiO_3$ phototransport for optical synapses with spiking-time dependent plasticity.

3.1 Abstract

Intuitively, processes towards equilibrium speed up when they become more favorable energetically. Yet, there are exceptions. For instance, according to Marcus theory, electron transfer in chemical reactions may slow down for particular solvent/reactant configurations, in spite of the energy drop between excited and ground states [111–114]. Persistent carrier photoexcitation via DX-centers bears some parallelism, as the interaction of electrons with phonons defines a configurational coordinate region where the decay of carriers to the ground state is precluded for long periods [87, 92, 115–119]. Here we present a quantum well (QW) where a secondary photoexcitation couples to QW states via quantum tunneling, enabling electrons to scatter into or out of the QW in an asymmetric manner, so that the conductance increases or decreases depending on the relative arrival time of photons of different frequencies. We use Green's function formalism to

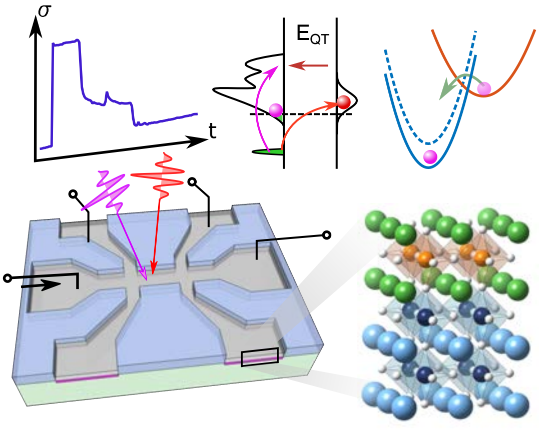

describe this asymmetric photoexcitation, which paves the way to an optical implementation of neurobiologically inspired spike-timing-dependent plasticity [120–122].

3.2 Experimental observations

The system under study is the interface between two wide-bandgap insulators, $SrTiO_3$ and $LaAlO_3$, where an electronic reconstruction, driven by electrostatic boundary conditions, drives the formation of the QW [63, 64] (seen Section 1.3.2). Briefly, $LaAlO_3$ is a polar material with a built-in electric field that needs compensation to reach stability [123, 124]. Below a critical thickness ($t_c \approx 1.5\, nm$), the interface is insulating and counteracting dipoles created by charged surface and interface sates balance the internal electric field (Figure 3.1a). At thickness t_c, surface states transfer electrons to the $LaAlO_3/SrTiO_3$ interface forming the QW (Figure 3.1b). Therefore, two mechanisms underpin the stability of the system: at $t < t_c$, oppositely charged surface and interface states compensate the internal field and the interface is insulating, while at $t \geq t_c$ the charge distributed across the QW also contributes to the field compensation (Figure 3.1a - b).

A perturbation of this subtle electrostatic balance should drive changes in the QW population and, therefore, changes in the transport properties. For instance, interaction with photons may change the occupancy of the QW. In particular, two photoconductive processes may occur in parallel that, as we will see in the following, can increase or deplete the occupancy. On the one hand, a photon can induce a transition from an interface state to the QW (Hamiltonian H_1 in Equation 3.1), which increases the occupancy of the QW (Figure 3.1c). Alternatively, a photon may trigger a transition to a surface state via quantum tunneling across the $LaAlO_3$ barrier (Hamiltonian H_2 in Equation 3.2), which changes the charge of the surface state, breaking the field compensation and leading to carrier depletion (Figure 3.1d).

3.3 Theoretical model

Let us describe the first phototransport process, which increases the QW occupancy and induces a positive persistent photoconductance. The Hamiltonian is:

$$H_1 = \Sigma_q \omega_q a_q^+ a_q + \sum_c \varepsilon_c b_c^+ b_c + \Sigma_q \Sigma_c M_q b_c^+ b_c [a_q + a_q^+] + \sum_k \varepsilon_k c_k^+ c_k \tag{3.1}$$

where the successive terms describe, respectively, lattice modes of vibration $(a_q^+ a_q)$, interface states $(b_c^+ b_c)$, the coupling of phonons to interface states $(M_q b_c^+ b_c [a_q + a_q^+])$ and QW states $(c_k^+ c_k)$. For simplicity, we ignore the polarization of phonons. A canonical transformation $\widehat{H}_1 = e^S H_1 e^S$ with $S = \sum_c b_c^+ b_c \sum_q \frac{M_q}{\omega_g} [a_q + a_q^+]$ simplifies the Hamiltonian to:

$$\widetilde{H_1} = \sum_q \omega_q a_q^+ a_q + \sum_k \varepsilon_k c_k^+ c_k + \sum_c (\varepsilon_c - \Delta)\, b_c^+ b_c \tag{3.2}$$

with $\Delta = \Sigma_q \frac{M_q}{\omega_q}$, where M_q is the dimensionless electron-phonon coupling parameter (see Appendix B.1). We assume that annihilation and creation operators b_c and b_c^+ refer specifically to DX-center states located at the interface. DX-centers have two possible states $c \in (c_0, c_1)$ that,

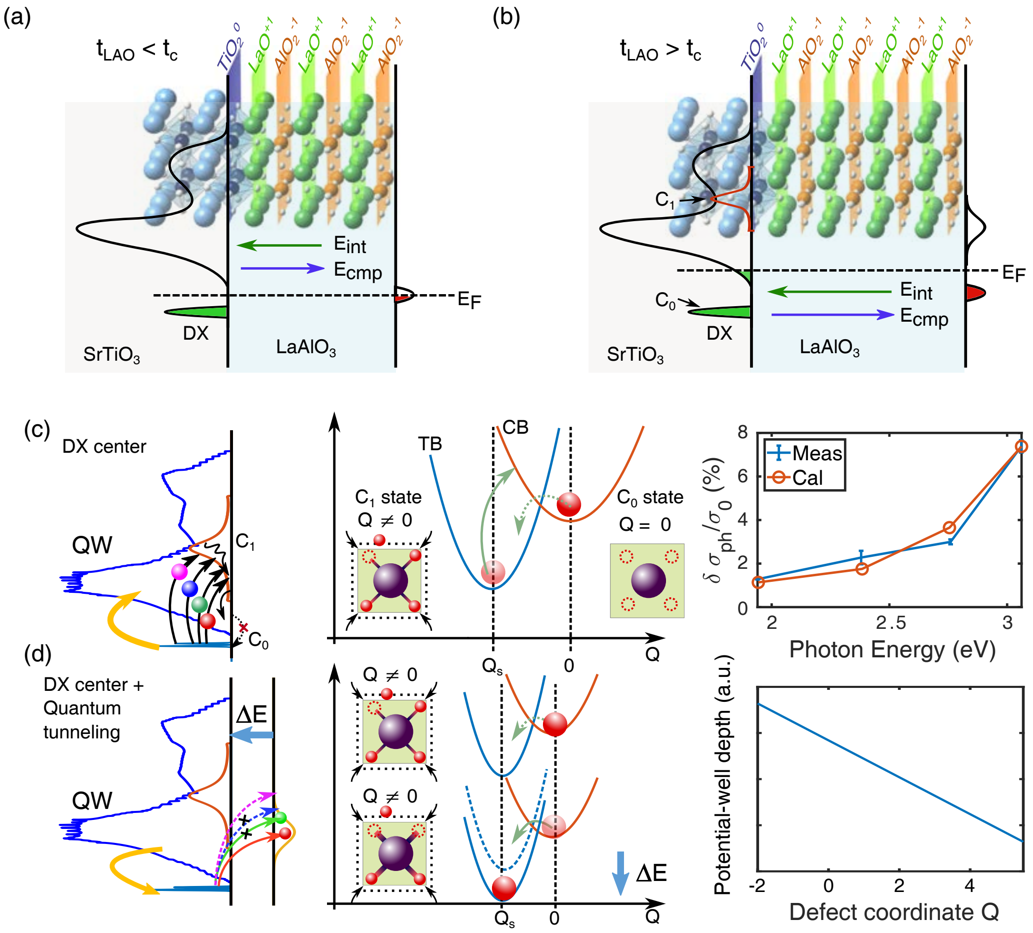
(a)
t_LAO < t_c
TiO2 0
LaO +1
AlO2 -1
Eint
Ecmp
EF
DX
SrTiO3
LaAlO3
(b)
t_LAO > t_c
C1
C0
(c)
DX center
QW
C1
C0
TB
CB
C1 state
Q ≠ 0
C0 state
Q = 0
Qs
0
Q
Meas
Cal
δ σph/σ0 (%)
Photon Energy (eV)
(d)
DX center +
Quantum
tunneling
ΔE
Q ≠ 0
Potential-well depth (a.u.)
Defect coordinate Q

FIGURE 3.1: (a) Charged atomic planes in $LaAlO_3$ $[(LaO)^+ / (AlO_2)^-]$ drive an internal electric field E_{int} that has to be compensated by the field E_{cmp} created by charged interface (DX-centers) and surface defect states. (b) When the thickness is above t_c, electrons are transferred from the surface to the quantum well (QW). (c) (left) Carrier accumulation in the QW via photoexcitation of DX-centers. Initially, the carriers are in the structurally relaxed c_0 state, with lower energy (middle). After photoexcitation, they jump into the unrelaxed state c_1 (right), which lies higher in energy. They are not allowed to jump back to c_0, because of the barrier in the configurational coordinate (Q) dependence of energy. The photoexcitation via DX-centers predicts correctly the spectral dependence of the photoconductance $\delta\sigma_{ph}/\sigma_0$ (see Appendix B.1, B.2, B.3, B.4 for details on calculations). (d) (left) Carrier depletion is triggered by photoexcitation of surface states via quantum tunneling. The process is resonant for red, while negligible for blue. The unbalanced field ΔE shifts the configurational energy landscape (see the rightmost panel and Appendix B.6), lowering the barrier for electrons to jump back to the c_0 state.

depending on their charge, can form either a shallow level with no structural relaxation (c_0) or a deeper level with lattice relaxation, which traps electrons (c_1) (Figure 3.1c). There is a wide consensus that the photoexcitation of trapped electrons in DX-centers is at the origin of persistent photoconductance in many semiconductors [92, 117, 125, 126]. Here we propose that DX-centers are formed also at the $LaAlO_3/SrTiO_3$ interface. Supporting this assumption is the observation that ignoring the mediation of DX-centers leads to a spectral photoresponse in complete disagreement with experiments (Appendix B.5), while models assuming DX-centers describe correctly the experiments (Figure. 3.1c). From deep-level transient spectroscopy (DLTS), we found trap energies located at $\sim\ (0.125 - 0.250)\ eV$ below the conduction band, which we relate to DX-centers (see Appendix B.3).

In the ground state (b_{c_0}, b^{+}_{c0}) the ions surrounding the DX-center are in an equilibrium configuration coordinate given by

$$Q_0 \approx M_q \left(\frac{\hbar}{2M\omega_q}\right)^{1/2} \tag{3.3}$$

where M is the ionic mass density, and $\hbar$ the Planck's constant. Thus, $Q_0 \neq 0$ relates to a structural relaxation that deform locally the lattice (Figure 3.1c). We assume further that the spectrum of excited quasi-particles of the unrelaxed DX-center related to operators $(b_{c_1}, b^{+}_{c_1})$ and configuration coordinate $Q_1 = 0$ lies within the QW. Therefore, in going from the ground to the photoexcited state there is a change in the configuration coordinate $\Delta Q = Q_0 - Q_1 \neq 0$ and, as a result, the lattice relaxation prevents the return of the carrier back to the initial state after photoexcitation (Figure. 3.1c). Consequently, the photoexcited state is long-lived, giving way to a conductance change that persists over extended periods. This phenomenon bears resemblance with inverted kinetic theory, where chemical processes slow down even when they are energetically favorable [111–114]. In Marcus theory, the deceleration of charge-transfer depends on the solvent/reaction configuration space, which plays the role of the configurational parameter space in persistence photoconductance.

A second mechanism relies on photoexcitation via quantum tunneling described by the Hamiltonian:

$$H_1 = \sum_{cl} T_{cl} b^{+}_{c} d_l + h.c. \tag{3.4}$$

where d^{+}_{l}, d_l are creation and annihilation operators of surface states. Note that charged surface states break the interface-surface electrostatic balance, so that photoexcited surface states induce a charge depletion of the QW to restore electrostatic balance (Figure 3.1d) and this entails a reduction of conductance. We will see below that the excitation of surface states is resonant at red and vanishingly small at shorter frequencies (blue and violet). We have therefore two mechanisms that have opposite effects on the conductance, so that the electron occupancy increases or decreases depending on the prevalent mechanism. To describe these counterbalancing processes, we define in-scattering $\Sigma_{in}(\vec{x}, t)$ and out-scattering $\Sigma_{out}(\vec{x}, t)$ functions that give account, respectively, of the inward and outward flux of particles. These functions are assumed to be proportional to differential scattering cross-sections $\frac{d^2\sigma}{d\Omega d\omega} \sim S(\vec{x}, t) = \langle A(\vec{x}, t) A(0) \rangle$, where $S(\vec{x}, t)$ is the autocorrelation function of an appropriate field operator $A(\vec{x}, t)$ [127]. For the in-scattering function, $A(\vec{x}, t)$ we use the current operator $j(\vec{x}, t)$, so that $\Sigma_{in}(\vec{x}, t) \propto \langle Tj(\vec{x}, t) j(0) \rangle$, where T is the Wick's time-ordering operator and finite-temperature Green's functions are used to calculate the correlation function (see Appendix B.1, B.2, B.3, B.4). The reason of using $j(\vec{x}, t)$ is that the increase of electrons in the QW is proportional to the optical absorption rate given by the current-current correlation function [127, 128]. At the end, we arrive at the expression:

$$\begin{gathered}\Sigma_{in}(\omega) \propto P\tfrac{\pi}{\omega}\left[\int \delta\left\{\hbar\omega - \left(\varepsilon^{*}_{jX} - \varepsilon_{DX}\right)\right\}(1- \\ n^{*}_{DX}\left(\varepsilon^{*}_{DX}\right))\, n_{DX}\left(\varepsilon_{DX}\right) d\varepsilon_{DX} d\varepsilon^{\dagger}_{DX}\right] e^{-g\left(2N_q+1\right)} \textstyle\sum_m \delta\left\{h\left(\omega-\omega_m\right) I_m(\gamma)\right\} e^{m\hbar\omega_0}/2k_B T\end{gathered} \tag{3.5}$$

Where ω is the frequency of light, P is the transition element assumed to be energy-independent, k_B the Boltzmann's constant, $n^{*}_{DX}(\varepsilon^{*}_{DX})$ and $n_{DX}(\varepsilon_{DX})$ are, respectively, the density of states of unrelaxed and structurally relaxed DX-center states, g is the electron-phonon coupling and $N_q = N_0 = \left[e^{\hbar\omega_0/k_B T} - 1\right]^{-1}$ gives the phonon occupation assuming an Einstein model where all phonons have the same energy ω_0. The physical interpretation of Equation 3.5 is that the transition from relaxed (ε_{DX}) to unrelaxed (ε^{*}_{DX}) DX-center states involves around m phonons, so that $\hbar\omega_m = \varepsilon^{*}_{DX} - \varepsilon_{DX} - (g-m)\hbar\omega_0$. As a consequence, the amplitude of this transition is modulated for different values of m, which is accounted for by the Bessel function $I_m(\gamma)$, where $\gamma = 2g\sqrt{N_0\left(N_0+1\right)}$.

On the other hand, the out-scattering function (describing the outward flux of particles) is proportional to the differential cross-section for tunneling across the insulating $LaAlO_3$ barrier (described by Equation 3.4). In this case, we require that

$$\Sigma_{\text{out}}(\omega) \propto I_{I-S} = 4\pi e T_0 \int d\varepsilon n_i(\varepsilon) n_s(\varepsilon + \hbar\omega) \tag{3.6}$$

where $I_{(I-S)}$ is the net current from interface to surface states, e is the electron charge, ϵ is the energy, n_s is the density of surface states T_0 is the tunneling matrix assumed to be independent of $\epsilon-$ and ω is the frequency of light.

We use non-equilibrium formalism, where Green's functions $G^{<} = -i\left\langle c_k(t) c^{+}_{k}(0)\right\rangle$ and $G^{>} = -i\left\langle c^{+}_{k}(t) c_k(0)\right\rangle$ describe how the system responds, respectively, to the addition and removal of electrons in QW states. These functions relate to the in- and out- scattering functions as $-iG^{<} + iG^{>} = G^R\left[\Sigma_{in}(\omega) + \Sigma_{out}(\omega)\right] G^A$, where G^R, G^A are the retarded and advanced Green's functions, respectively. In the following, we demonstrate that the photoexcitation process described by $\Gamma\left(\omega_2,\omega_1\right) = \left[\Sigma_{in}\left(\omega_2,\omega_1\right) + \Sigma_{out}\left(\omega_2,\omega_1\right)\right]$ is asymmetric, where a pair of short- and long- wavelength pulses of frequencies $\omega_2 \neq \omega_1$ excites the system at two different times. We can formally describe the whole process by establishing a binary relation between frequency and time $\omega_i \leftrightarrow t_i$, so that the asymmetric scattering function is:

$$\Gamma\left(\omega_2,\omega_1\right)_{t_2>t_1} \neq \Gamma\left(\omega_1,\omega_2\right)_{t_2<t_1}; \quad \omega_2 > \omega_1 \tag{3.7}$$

Let us first consider the process described by $\Gamma\left(\omega_2,\omega_1\right)_{t_2>t_1}$. First, a pulse of light of lower frequency excites electrons to the QW via the unrelaxed DX-center (Figure 3.1c), as well as to surface states (Figure 3.1d). Photoexcitation via DX-centers prevails and the global effect is an increase of electrons in the QW. Subsequently, a second pulse of higher frequency leads to a stronger increase of the QW population. Now we consider the process described by the right-hand side of Equation 3.7, i.e., $\Gamma\left(\omega_1,\omega_2\right)_{t_2<t_1}$. Now a first pulse of higher frequency leads to an increase of the QW population. However, a subsequent pulse of lower frequency decreases the population of the QW (Figure 3.1d), because of the excitation of surface states resonant at longer

wavelengths, which induces a depletion of the QW population. Therefore, time order in pulsed sequences of photoexcitation matters, as it determines whether the QW occupancy increases or decreases.

The data shown in Figure 3.2a-b validate the asymmetric photoresponse described by Equation 3.7 (see Chapter 4, for further experimental details). We first discuss the experiments described by the left-hand side of Equation 3.7, $\Gamma\left(\omega_2,\omega_1\right)_{t_2>t_1}\left(\omega_2>\omega_1\right)$. A first pulse of red light ($\lambda_1 = 632\,nm$) and duration $\Delta\tau_1 = 10$ seconds precedes a second pulse of blue light ($\lambda_1 = 450\,nm$) and duration $\Delta\tau_2 = 10$ seconds. At the end of this two-pulse sequence, the conductance increases by an amount $\Delta\sigma_{1\rightarrow 2} = \sigma\left(t_2\right) - \sigma\left(t_1\right) \approx 0.05\,\mu S$ which is almost 2% of the initial conductance (Figure 3.2a). Now, we consider the reverse process, i.e., $\Gamma\left(\omega_1,\omega_2\right)_{t_2<t_1}\left(\omega_2>\omega_1\right)$, where the timing of pulses is inverted with respect to the previous two-pulse sequence. In this case, a first pulse of blue light reaches the sample, followed by a red pulse, both of them of same duration as before, so that only their relative timing is inverted. Now, we observe that the conductance resets to the initial value, before illumination with the first pulse (Figure. 3.2b). This observation shows that resonant photoexcitation to surface states via quantum tunneling leads to carrier depletion. We further observe that the depletion depends on the wavelength of the second pulse, being strongest for red and absent for blue (Figure 3.2c-d), indicating that the excitation is resonant near red light. This wavelength-dependent asymmetric photoexcitation enables the modulation of the QW conductance through sequences of multiple short-/long-frequency pulses, depending on the relative time arrival of photons of different wavelengths (Figure 3.2g), which we further discuss below in the context of neuromorphic computation.

Two further experiments confirm the relevance of balanced electrostatic boundary conditions in the photoinduced carrier accumulation and depletion. First, we note that the internal electric field exists as long as the $LaAlO_3$ is epitaxial, while it should be absent in amorphous layers [63, 123, 124]. Therefore, the photoexcitation to surface states of amorphous $LaAlO_3$ should not affect the QW population because there is no field to compensate inside the barrier layer. We checked this prediction by measuring the photoconductance of devices defined on interfaces between amorphous $LaAlO_3$ films ($t \approx 3\,nm$) and $SrTiO_3$ (see Figure 3.3a-b). The experiments, shown in Figure 3.3c, confirm that the mechanism for carrier depletion is absent in this case.

Secondly, quantum tunneling decays exponentially with the barrier thickness, so that carrier depletion caused by excitation to surface states should drop fast as the thickness of $LaAlO_3$ increases. To verify it, we measured the difference $\Delta\Xi \equiv \left[\Delta\sigma_{1\rightarrow 2} - \Delta\sigma_{2\rightarrow 1}\right]$ in devices defined with variable $LaAlO_3$ thickness. Figure 3.3c displays the results for $t \approx 5uc \approx 2\text{nm}$ and $t \approx 14\,uc \approx 5\,\text{nm}$, confirming the strong reduction of $\Delta\Xi$ with barrier thickness.

The asymmetric photoexcitation described by Equation 3.7 is of potential interest for neuromorphic engineering, which aims at designing physical systems inspired by neurobiology. In particular, spike-timing-dependent plasticity (STDP), where the relative timing of neuron spikes rules the increase or decrease of plastic synaptic strength, is fundamental to achieve unsupervised learning [120–122]. Inspired by these principles, there has been multiple efforts to implement STDP in physical systems, with a particular success using memristors, where electric impulses mimic the action of neuron spikes [119, 121].

In this work, we show that the asymmetric photoexcitation of the $LaAlO_3/SrTiO_3$ QW may

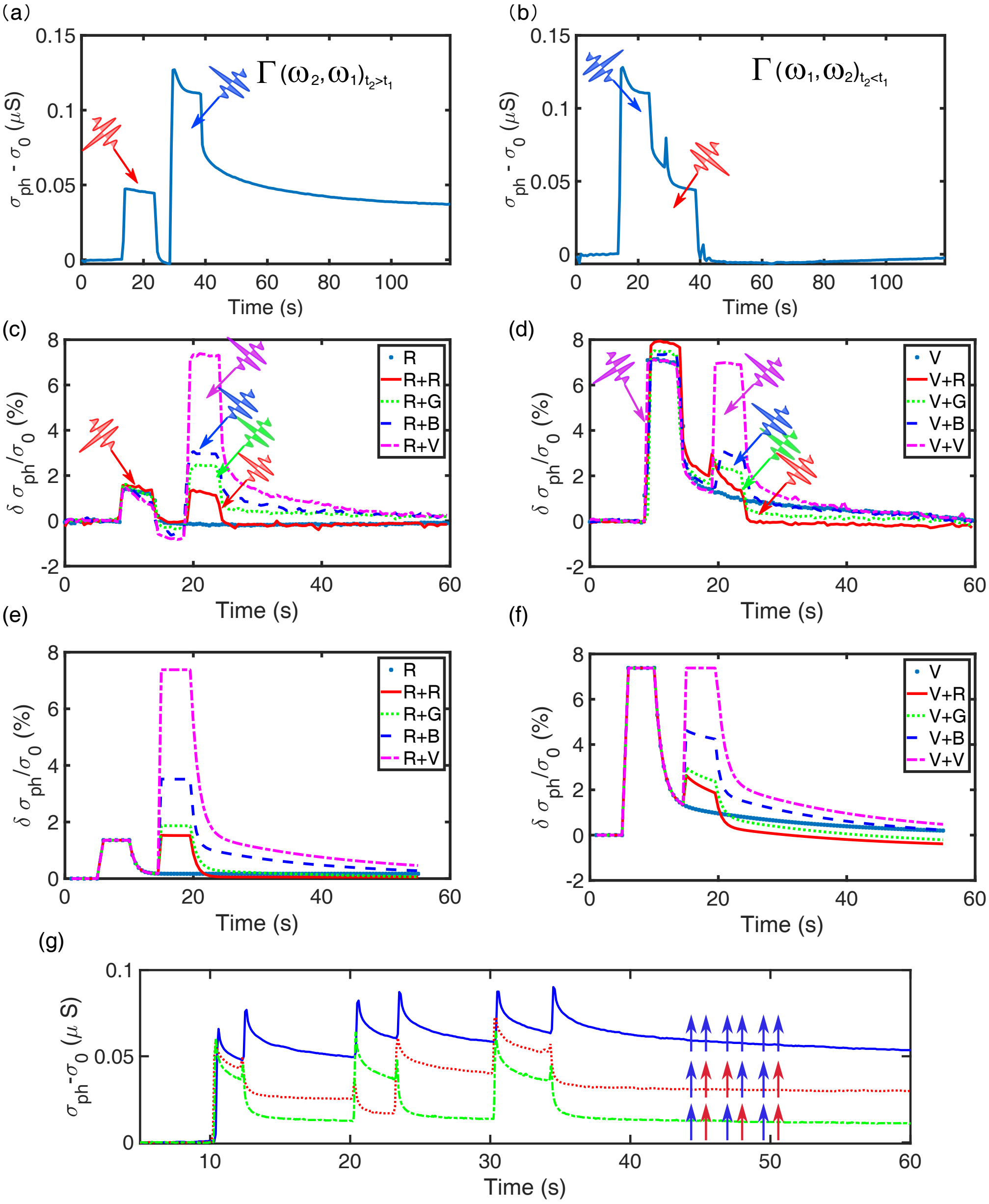

FIGURE 3.2: (a) Photoconductance measured in a two-pulse sequence, where a red pulse comes first, followed by a blue pulse. The situation corresponds to $\Gamma(\omega_2,\omega_1)_{t_2>t_1}$ in Equation 3.7. (b) Photoconductance measured after a first blue pulse, followed by a red pulse, corresponding to $\Gamma(\omega_1,\omega_2)_{t_2<t_1}$. Note that when red follows blue, there is a decrease of conductance, instead of an increase. (c) Photoconductance measured after a red pulse followed by green, blue and violet pulses. In all cases, there is an increase of conductance after the second pulse. (d) The situation is reversed when red follows a violet pulse. In this case, the conductance decreases after the second pulse. The effect is resonant with red, and negligible for blue. Relative changes of conductance after different multiple-pulse sequences. We represent the timing in the upper part of the figure. The blue curve in the figure corresponds to conductance changes induced by multiple an all-blue-pulse sequence, while the red curves displays the photoconductance measured under multiple blue/red-pulse sequence. The whole sequence shows that time-correlated arrival of pulses of different frequencies increase or decrease plastically the conductance.

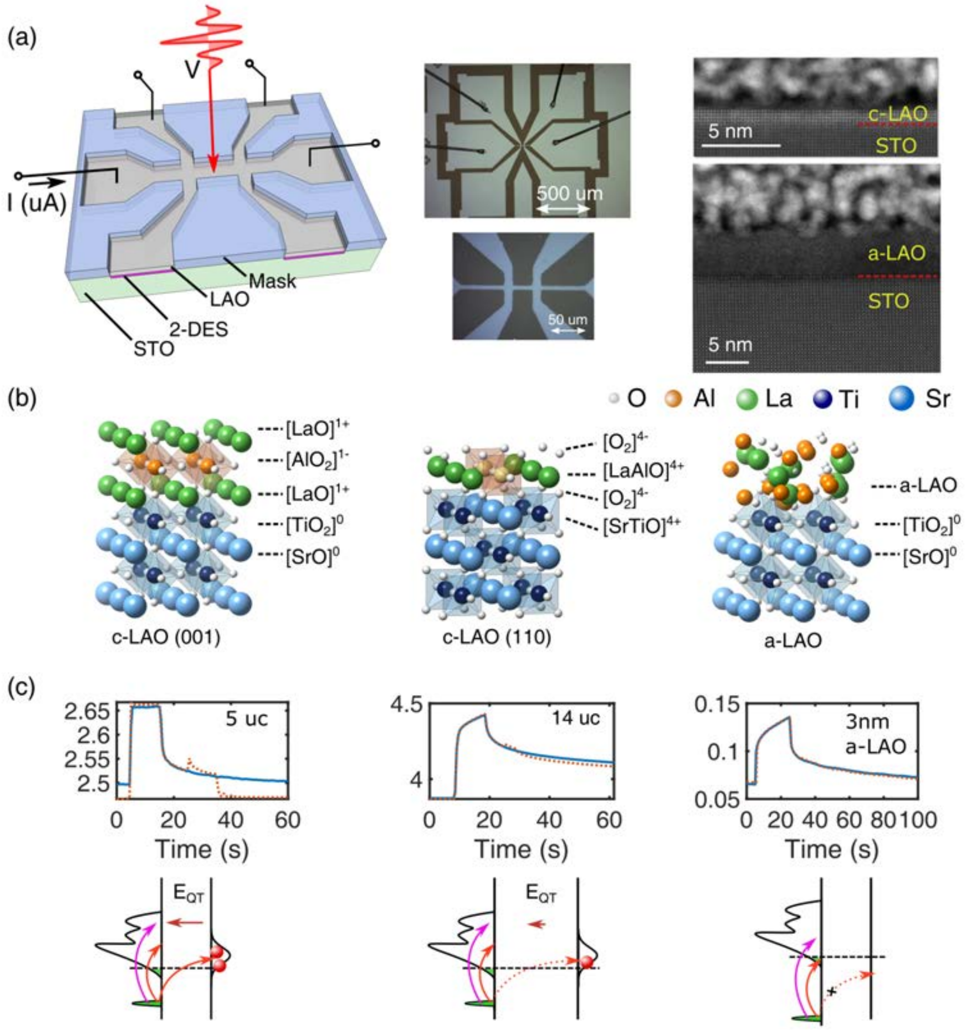
(a)
V
I (uA)
Mask
LAO
2-DES
STO
500 um
50 um
5 nm
c-LAO
STO
a-LAO
STO
5 nm
(b)
O
Al
La
Ti
Sr
[LaO]1+
[AlO2]1-
[LaO]1+
[TiO2]0
[SrO]0
c-LAO (001)
[O2]4-
[LaAlO]4+
[O2]4-
[SrTiO]4+
c-LAO (110)
a-LAO
[TiO2]0
[SrO]0
a-LAO
(c)
2.65
2.6
2.55
2.5
5 uc
0 20 40 60
Time (s)
4.5
4
14 uc
0 20 40 60
Time (s)
0.15
0.1
0.05
3nm
a-LAO
0 20 40 60 80100
Time (s)
EQT
EQT

FIGURE 3.3: (a) Hall devices, pictured here, were used to measure the photoconductance. We fabricated devices with epitaxial (c-$LaAlO_3$) and amorphous (a-$LaAlO_3$) $LaAlO_3$ layers (see the STEM images). In (b) we show a schematic depiction of the corresponding atomic arrangements. (c) Illumination with blue plus red pulses induces carrier depletion in the sample with thin epitaxial $LaAlO_3$ ($t = 5\,uc \approx 1.9\,nm$). However, the depletion is much smaller when the thickness increases to $t = 14\,uc \approx 5.6nm$. Likewise, carrier depletion is absent in the sample with amorphous $LaAlO_3$ layer. Therefore, carrier depletion via quantum tunneling photoexcitation requires thin epitaxial layers of $LaAlO_3$.

implement STDP using optical stimulation instead of electric inputs. More specifically, we demonstrate that multiple-pulse sequences increase or decrease the conductance depending on the relative timing of long- and short-wavelength pulses in a way that is comparable to memristive STDP devices [121], paving the way to optical STDP synapses. To illustrate this point, we refer to the data displayed in Figure 3.2e, which corresponds to a sequence of blue and red pulses. We observe that illumination with red after the first blue pulse entails a significant decrease of conductance, which in this context plays the role of the synapse. A subsequent red pulse decreases even more the conductance with respect to the first red pulse, showing a cumulative effect. The next two blue pulses increase substantially the conductance and, finally, the third and last red pulse decreases once more the conductance. Therefore, appropriate timed combinations of short-/long- wavelength pulses can fine-tune the conductance, featuring spike-timing-dependent plasticity using optical inputs in a similar way as memristive synapses replicate STDP using electric stimuli [121].

3.4 Conclusion

We have explored the persistent photoconductance at the epitaxial $LaAlO_3/SrTiO_3$ interface, which is interpreted with a large lattice relaxation model. Furthermore, we have demonstrated a wavelength-dependent time-correlated photoresponse. This asymmetric photoresponse involves photoexcitation of electrons from defect-related DX-centres at the interface, plus a photoexcitation to surface states via quantum tunneling. The observed photoresponses can be exploited for optical synapses with STDP, which will be developed and explained in Chapter 4. On the other hand, STDP cannot be implemented in amorphous $LaAlO_3/SrTiO_3$ interfaces, due to their non-epitaxial microstructure. However, the relatively large sensitivity of the photoconductance of amorphous $LaAlO_3/SrTiO_3$ interfaces may make them interesting for neuromorphic apllications that do not require STDP, which is discussed in Chapter 5.

Chapter 4

Solid-State Synapses Modulated by Wavelength-Sensitive Temporal Correlations in Optic Sensory Inputs

---

In Chapter 3, we have given a physical explanation of the photoconductance with wavelength correlations at the epitaxial $LaAlO_3/SrTiO_3$ interface. In this chapter, we study in detail the wavelength-dependent time-correlated photoresponses and show that they can be exploited for optical synapses with wavelength-sensitive STDP. Finally, simulations suggest that this capability may stimulate neuromorphic hybrid electronic/photonic systems to construct biomimetic spatial memory and navigation maps inspired from neurobiology.

4.1 Abstract

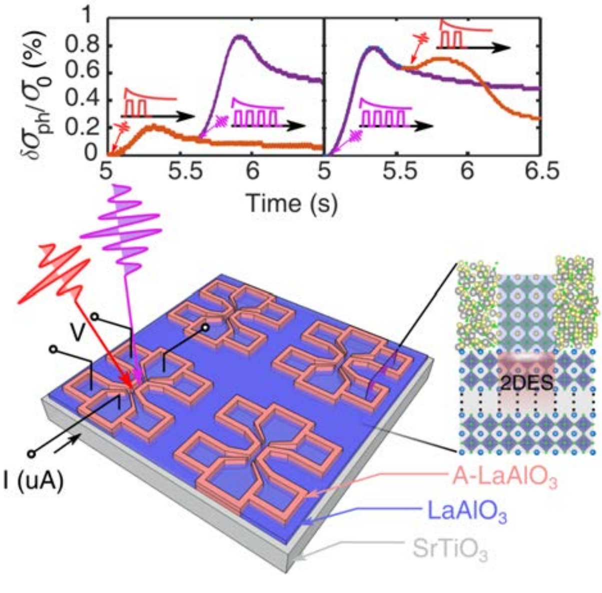

Recently, inspired by neurobiological information processing, correlation-based learning has been expressed physically in nonbiological systems by exploiting time causality of electric signals. Yet, the capability to learn from visual events requires extending these concepts to optical stimuli. Here we show a solid-state system (the epitaxial $LaAlO_3/SrTiO_3$ interface) that is sensitive to 100-millisecond-scale timing of pairs of light stimuli with complementary short/long visible wavelengths, causing asymmetric changes of photoconductance. This property endows optical signals with time causality, leading to wavelength-sensitive time correlations with timescales comparable with those of perceptual recognition. Based on these observations, we propose that complex information can be extracted from visual patterns imprinted as spatiotemporal modulations of persistent photoconductance. We suggest that this capability may stimulate neuromorphic hybrid electronic/photonic systems to construct biomimetic spatial memory and navigation maps inspired from neurobiology.

4.2 Introduction

In nervous systems, sensory neurons convert stimuli into action potentials that send information to the brain. Inspired by these neurobiological processes, neuromorphic engineering has emulated cognitive functionality in several nonbiological systems, including memristors [129, 130], phase-change materials [131], spin oscillators [53, 132] or ferroelectric junctions [122]. Similarly, biological transduction has inspired technological developments, e.g., the emergence of neuromorphic vision chips [133, 134], which enable real-time analysis of high-speed movements unattainable by conventional technologies [135, 136]. Underlying brain cognitive capabilities is the concept of synaptic plasticity [121], whereby the strength of excitatory (inhibitory) synapses can increase (decrease) over time in response to changes in neuron activity. A particularly relevant case occurs when synaptic modulation is driven by the correlated activity of pre- and postsynaptic neurons, which was initially postulated to stabilize neuronal activity patterns in the brain that imply learning [137]. Inspired by such principles, time-correlated synaptic changes in the form of spike-time-dependent-plasticity (STDP) was first suggested in computational neuroscience [121] and experimental evidence accumulated in biological systems [138–140]. Along these lines, solid-state synapses based on memristors have been demonstrated to exploit causality of electric signals and enabling unsupervised learning [122]. Yet, the development of artificial neural networks interacting with a variety of environmental inputs requires the extension of time-correlations beyond electric signals. Particularly, correlated timing of optical stimuli would enable a whole new perspective on biomimetic artificial vision, where learning rules could be applied to complex visual events [141].

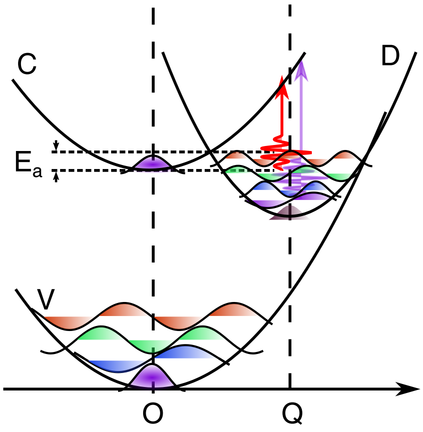

FIGURE 4.1: The persistence photoconductance in terms of the space of configurational coordinates [92]. Before photoexcitation, the electron is in a deep DX center (D). When D is occupied, the strong coupling to the lattice induces a rearrangement of the ion positions in its immediate vicinity, and the strain associated with such distortion is represented by $Q \neq 0$. An incident photon induces an electronic transition from D to the 2DES (C), while a structural lattice relaxation drives a change of the DX center to $Q = 0$. The irreversible shift in Q implies an energy barrier (E_a), precluding the return of the electron back to the initial state. The energy levels of the vibronic state of D corresponding to quantum levels of a harmonic oscillator are graphically depicted.

In this work we show that causally correlated potentiation and depression of synaptic plasticity can be replicated in a solid-state system that exhibits persistent photoconductance (PPC) [58, 92], where the conductance suddenly changes after illumination with visible, or ultraviolet light or X-rays [142] and the effect persists over long periods after the light is off. This phenomenon, observed in many semiconductors, is generally caused by DX centers [87], whereby shallow donors undergo a large lattice relaxation, thus preventing the return of the carrier back to the initial state after photoexcitation [92] (Figure 4.1). Our study reveals that the conductance of the PPC system can be increased or decreased in a controlled way by external optical stimuli formed by combinations of short-/ long-wavelength pairs of visible light pulses, where the control is done at 100 millisecond-scales, comparable with timescales for perceptual recognition. The synaptic modulation can be fine-tuned by the order of the time arrivals of the light pulses as well as by their duration and, most remarkably, it is wavelength-sensitive, namely, the particular selection of the wavelengths of the light pulses is critical to the synaptic modulation. We posit that wavelength-sensitive time-correlations in optical stimuli can be exploited to use information encoded in light to build spatial memory and navigation maps akin to processes occurring in brains, with timescales comparable with cognitive processes.

The system under study is the interface between $SrTiO_3$ and $LaAlO_3$, two wide-bandgap semiconductors. As described in Chapters 1 and 3, despite the insulating character of the constituent materials, a highly-conductive two-dimensional electron system (2DES) develops across an nm-thick region around the interface [63]. This 2DES hosts a number of properties including superconductivity [64], large spin-orbit fields [66] and, importantly for the context of this work, PPC [67].

4.3 Results

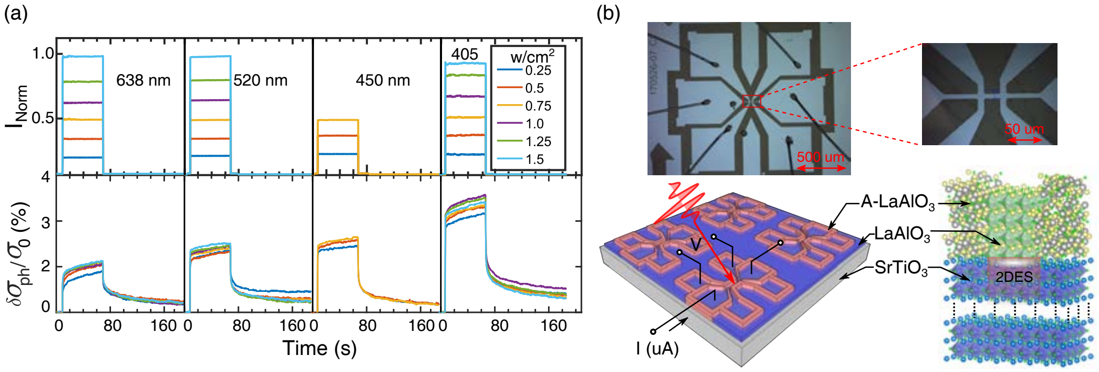

FIGURE 4.2: a) The upper panels show optical micrographs of a Hall bar. The lower panels show a schematic depiction of the Hall-bar geometry (left) and a cross-sectional graphic view of the $LaAlO_3/SrTiO_3$ device used in the experiments. A-$LaAlO_3$ and C-$LaAlO_3$ stand, respectively, for amorphous and epitaxial $LaAlO_3$ (right) (see Methods for details on sample and device preparation). b) Schematic depiction of the Hall-bar geometry.

Our study comprises epitaxial $LaAlO_3$ thin films with thickness $t \approx 1.1 - 5.3\,nm$ ($3 - 14$ unit cells, u.c.) grown on (001)-oriented $SrTiO_3$ crystals. By way of illustration, Figure 4.2a summarizes the main features of PPC by displaying data extracted from measurements done with wide pulses (tens of seconds in contrast to millisecond-range pulses studied below) at four wavelengths in the visible red ($\lambda = 638\,nm$), green ($\lambda = 520\,nm$), blue ($\lambda = 450\,nm$) and violet

($\lambda = 405\, nm$) and different irradiance values. In these experiments, Hall-bar devices where defined by optical lithography (Figure 4.2b). The transport was characterized by injecting currents (typically $I \approx 1\, \mu A$) along two contacts, and measuring the longitudinal resistance by probing the voltage on two other contacts (typical resistance values were $R \approx 100 - 500\, k\Omega$, see also Supporting Information Section 4.7.8 for more details on the voltage readout). Photoexcitation experiments were carried out at room temperature using high-numerical-aperture (high-NA) focusing. After switching the light on, there is a sudden increase of conductance (Figure 4.2a) that we quantify as $\frac{\delta\sigma_{ph}(t)}{\sigma_0} = \frac{\sigma_{ph} - \sigma_0}{\sigma_0}$, where σ_0 is the conductance prior to switching the light on and σ_{ph} is the time-dependent conductance.

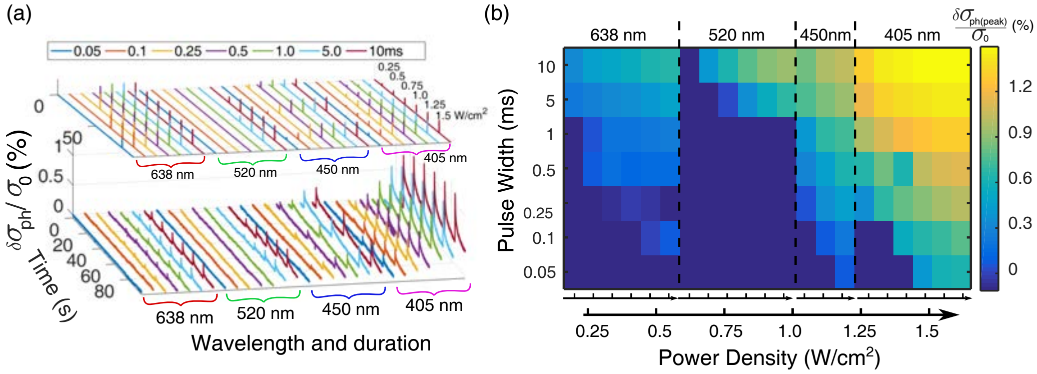

FIGURE 4.3: a) Photoconductance measured under illumination with trains of pulses of different wavelength (638, 520, 450 and 405 nm), width ($W_p \approx 0.05 - 10\, ms$) and irradiance ($0.25 - 1.25\, W/cm^2$). b) Two-dimensional maps where the photoconductive response is mapped against wavelength, irradiance and pulse width.

The analysis of the time-dependent response shows that light stimuli can be detected down to milliseconds for visible wavelengths (Figure 4.2 and Figure 4.3). The photoconductance was measured under illumination with different wavelength, width and irradiance (Figure 4.3a), and the photoconductive response $\frac{\delta\sigma_{ph}(t)}{\sigma_0}$ is mapped against wavelength, irradiance and pulse width in the 2-dimensional maps shown in Figure 4.3b.

Furthermore, measurements of $\frac{\delta\sigma_{ph}(t)}{\sigma_0}$ after illumination with light pulses of varying durations and different illumination conditions demonstrate a plastic PPC response that can be fine-tuned by controlling the cumulated illumination time (Figure 4.4a,b). This is also shown in Figure 4.4c,d. In particular, Figure 4.4c displays the reflected intensity measured by the photodetector replicating the shape of the incoming light pulses of cumulated times spanning the range of $5 - 250$ milliseconds. In Figure 4.4d we plot the full time evolution of the photoconductance over the whole period of analyzed time, after illumination with light pulses of cumulated times spanning the range $5 - 250$ milliseconds. The middle panel shows a zoom of the data around the initial times, while the right panel displays the data for a time interval $\approx 156 - 160$ after the light is switched off. As Figure 4.4d shows, in spite of some occasional irregularity (see, e.g., right panel of Figure 4.4d corresponding to data indicated by the arrow in Figure 4.4b), the photoconductance response can be fine-tuned by the cumulated time, as can be seen in Figure

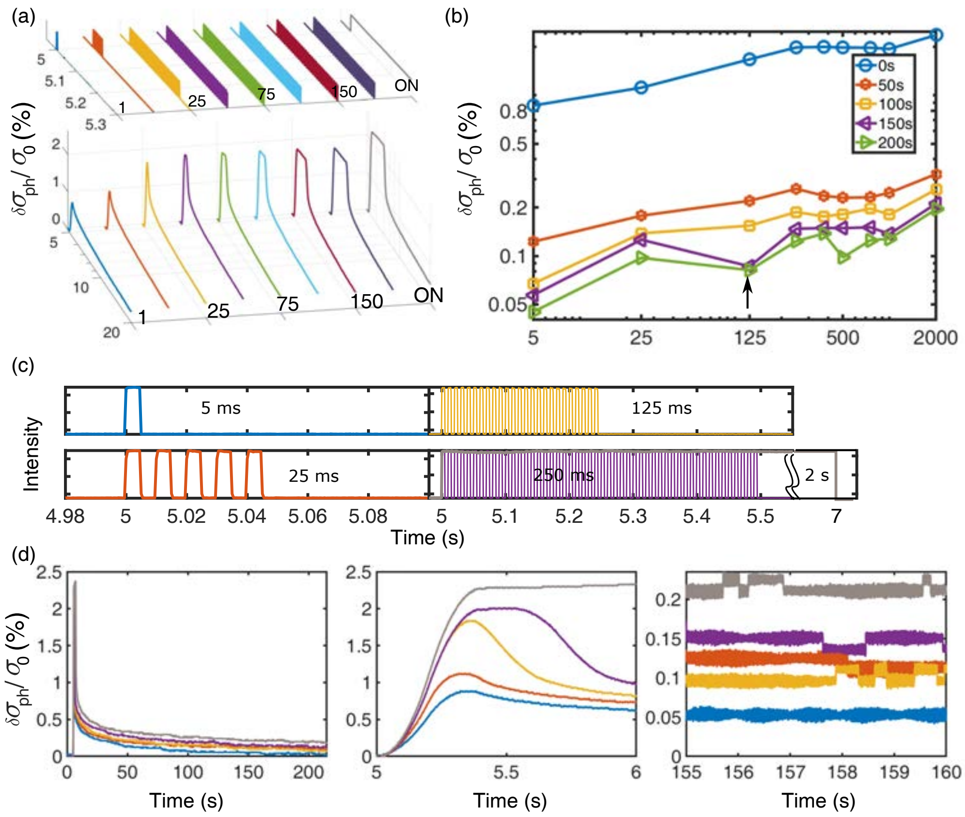

FIGURE 4.4: (a) and (b) show the tunability of the photoconductance by exposing the sample to violet ($\lambda = 405nm$) light pulses of different timespans. In particular, (b) shows the changes in photoconductance $\frac{\delta\sigma_{ph}(t)}{\sigma_0}$ measured at different probe times ($\tau = 0, 15, 30$ and $45\, s$) as a function of the cumulated illumination time. In particular, (c) displays the reflected intensity measured by the photodetector replicating the shape of the incoming light pulses of cumulated times spanning the range of $5 - 2000\, ms$. In (d). we plot the full time evolution of the photoconductance over the whole period of analyzed time, after illumination with light pulses of cumulated times spanning the range of $5 - 250\, ms$. The color code identifying the cumulated time in the $5 - 250\, ms$ range is the same as in panel (c). The middle panel shows a zoomed-in portion of the data around the initial times, whereas the right panel displays the data for a time interval of $\sim 155 - 160s$ after the light is switched off.

4.4c. We also note that the photoconductive response shows an uneven dependence on wavelength, with an apparent unexpected smaller responsiveness to green light (Figure 4.3b). We suggest that the particulars of the spectral response are related to the details of the density of states linked to the energy landscape of the involved defects, as well as to the features of the conduction band. Below we elaborate further on these aspects in connection with the plausible microscopic mechanisms at work for the observed PPC response.

Motivated by computational approaches to use visual patterns for learning similar to time correlations observed in biological systems [141, 144], we explored the possibility to express physically such concepts using persistent photoconductance. The basic idea is to combine light pulses (sensory inputs) of two complementary wavelengths that have opposite effects on the

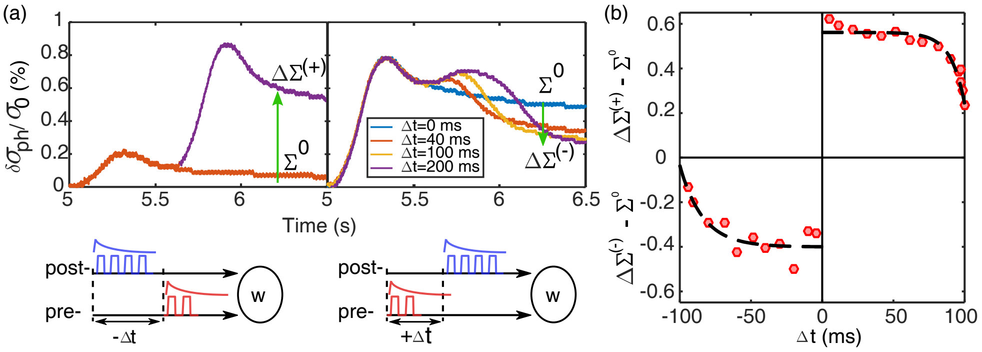

FIGURE 4.5: a) (Left upper panel) Photoconductance measured after a single pulse of red ($\delta T_r = 60\,ms$, red line) and after a two-pulse sequence of red ($\delta T_r = 60\,ms$) plus violet ($\delta T_v = 40\,ms$), purple line. The two-pulse sequence increases the photoconductance from Σ^0 to $\Sigma^0 + |\Delta\Sigma^{(+)}|$. (Right upper panel) The order of the pulse timing is reversed: violet pulses ($\delta T_v = 40\,ms$) are followed by red pulses ($\delta T_v = 0 - 200\,ms$); the conductance now *decreases* from Σ^0 to $\Sigma^0 - |\Delta\Sigma^{(-)}|$. The results displayed in a) enable a formal equivalence between red/violet pulse timing and causality of pre- and post-synaptic neurons, as shown schematically in the lower panels. b) Plots the causal ($|\Delta\Sigma^{(+)}(\Delta t)|$) and anti-casual ($|\Delta\Sigma^{(-)}(\Delta t)|$) branches of the learning curve derived from experiments in a). For clarity, the data of the branch is magnified by 5. Dashed lines in b) are a fitting to Equation 4.1 . Two-pulse sequences are used to simulate a map model for head direction [143]. At every orientation, just a small number of synapses are potentiated, while synapses unrelated to that orientation are depressed.

plasticity of PPC. With this in mind, we tried different combinations of wavelengths in the visible. First, we consider the illumination with short pulses of red, green or blue followed by violet. In this case, in agreement with the cumulative effect discussed in the previous discussion, illumination with the second pulse just increases the photoconductance above the value set by the first pulse (see the left upper panel of Figure 4.5a for red followed by violet). However, the outcome is different when we reverse the timing: if violet pulses are followed by green or red, the photoconductance is decreased with respect to the first pulse (right upper panel of Figure 4.5a and Chapter 3). These observations are in line with the time-correlated wavelength-dependent photoresponses discussed in Chapter 3. The decrease after the second pulse depends on the wavelength used for the the second pulse: the suppression of photoconductance is the largest for red and diminishes progressively towards blue (Figure 4.10 and Chapter 3). This observation hints at the use of time correlations between long and short wavelengths to drive synaptic changes. Indeed, multiple-pulse sequences of long-/short- wavelength timed pulses can be used to modulate the conductance enabling spike-timing-dependent plasticicity (see Figure 4.18 in Supporting Information Section 4.7.9). To exemplify this approach, we select red and violet wavelengths to establish a formal equivalence with pre- and post-synaptic neurons [121], respectively (see the sketches in Figure 4.5a). The first pulse, red or violet, sets the initial photoconductance $\Sigma^0 \equiv \dfrac{\delta\sigma_{ph}(\Delta t^0)}{\sigma_0}$. Subsequently, depending on the relative timing of the short-/long-wavelength in the two-pulse sequence, the second pulse either increases ($\Sigma^{(+)} \equiv \Sigma^0 + |\Delta\Sigma^+|$, Figure 4.5a left upper panel or decreases the conductance ($\Sigma^{(-)} \equiv \Sigma^0 - |\Delta\Sigma^{(-)}|$, Figure 4.5a right upper panel). This allows defining causal ($\Sigma^{(+)}$) and anti-causal ($\Sigma^{(-)}$) learning branches, respectively, using sub-100 millisecond pulses (Figure 4.5b) that, in our case, can be described approximately by:

$$\Delta\Sigma^{(\pm)}(\Delta t) = \begin{cases} \propto [+|A_{+,0}| - |A_{+}|e^{+\frac{\delta t}{\tau_{+}}}] & \text{for } \Delta t > 0 \\ \propto [-|A_{-,0}| + |A_{+}|e^{-\frac{-\delta t}{\tau_{-}}}] & \text{for } \Delta t < 0 \end{cases} \tag{4.1}$$

where $A_{+,o}$, A_{+}, $A_{-,o}$, A_{-} reflect, respectively, the amplitudes of potentiation and depression and τ_{+},τ_{-} are the corresponding time constants.

Summarizing, our study reveals that the conductance can be accurately increased or decreased by a combination of three basic factors: (i) *time arrival*: if short-wavelength pulses arrive earlier than long-wavelength pulses, the conductance increases with respect to the first pulse (case *i.1*), while the conductance decreases with respect to the first pulse if short-wavelength pulses arrive later than long-wavelength pulses (case *i.2*), (4.6a,b); (ii) *cumulated time*: the increase of conductance case *i.1* or its decrease case *i.2* is modulated by the cumulated time of the light pulses. This is shown in 4.6a,b where the precise amount of decrease or increase of conductance depends on the duration of the combined pair of pulse trains; (iii) *wavelength*: as shown in 4.6c-e, for fixed cumulated times, the decrease of conductance in short-/long- wavelength pairs is modulated by the wavelength of the second train of pulses. In particular, the decrease of conductance is largest for second pulses of red light, smaller for green and negligible for blue.

Before proceeding, we make an important observation regarding our approach to time correlations using optical inputs. Our work reveals that if we consider time correlations of optical stimuli that change the synaptic weight between a first (pre-synaptic pulse) and a second (post-synaptic) pulse, a new concept that uses also the wavelength of light can be exploited to achieve spiking time dependence plasticity. This concept enables the replication of inhibitory or excitatory synapses encompassing a wide diversity of functional dependences [143, 145]. As described below, we propose that this these wavelength.-sensitive time correlations can be also exploited to use information encoded in light to build spatial memory and navigation maps akin to processes occurring in biological brains, with timescales comparable with biological processes.

4.4 Discussion of the potential for neuromorphic engineering

The application of correlation-based rules for synaptic update is interesting, as it enables unsupervised learning [141], which in this case would apply to visual inputs [141, 144]. Indeed, neuron models based on memristive devices that implement STDP have been already demonstrated to show unsupervised learning [122, 146]. Here we shifted our attention away from known applications of time-correlated synaptic changes to explore alternative possible implementations into new domains. More specifically, we explored the feasibility of exploiting the observed phenomenon to emulate the coexistence of excitatory and inhibitory synapses which is indispensable to build brain-like cognitive maps [147–149]. As an exemplary illustration, we consider the construction of one-dimensional attractor map models for head direction, in which neuron firing rates evoke the direction along which the head is facing [147]. With this in mind, we

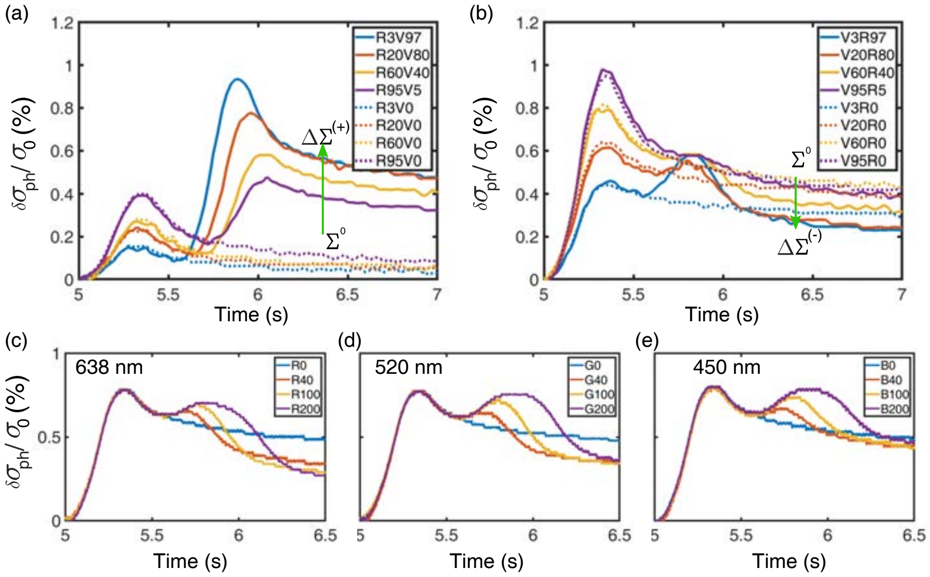

FIGURE 4.6: The ensemble of panels display the changes $\Sigma^0 \pm |\Delta\Sigma^{(\pm)}|$ of the conductance measured after two-pulse sequences of red ($\Delta T_r = 0 - 95\ ms$) plus violet ($\Delta T_v = 0 - 95\ ms$).The value of is set after the first pulse. a) The two-pulse sequence Σ^0 increases the photoconductance from Σ^0 to $\Sigma^0 + |\Delta\Sigma^{(+)}|$ when red pulses come before violet. b) When the order of the pulse timing is reversed, i.e., violet pulses are followed by red pulses, the conductance decreases from Σ^0 to $\Sigma^0 - |\Delta\Sigma^{(-)}|$. The timing and duration of the first and second pulses determine quantitatively the increase or decrease of conductance. Labels R(X)V(Y)/V(Y)R(X) in panels a) and b) display the conductance changes after combined pulses of red and violet light of duration X and Y milliseconds. The measured changes in photoconductance ($\pm|\Delta\Sigma^{(\pm)}|$) are used to plot the causal and anti-causal branches of the plot shown in Figure 4.5. Panels c)-e) show the photoconductance measured after a single pulse of violet ($\Delta T_v = 40\ ms$) followed by red, green and blue pulses of varying duration $\Delta T_{(r,g,b)} = 0 - 200 ms$. Since longer-wavelength pulses come after short-wavelength pulses, the synaptic strength is decreased with respect to the first pulse (we are in the $\Sigma^0 - |\Delta\Sigma^{(-)}|$ anti-causal branch of Figure 4.7 a. Yet, the value of the decrease of conductance ($-|\Delta\Sigma^{(-)}|$) depends on wavelength: the suppression is the largest for red, smaller for green and negligible for blue.

simulated leaky integrate-and-fire neurons driven asynchronously by two input sensory cells, corresponding to red and violet stimuli (see Experimental Section 4.6 and Supporting Information Section 4.7.3 for extensive details). Figure 4.7a shows graphically the time evolution of the synaptic strengths of selected neurons for two simulated consecutive head movements along two orientations in space. We stress that for the sake of realistic modeling, the calculations take care of the experimental decay times of conductance after photoexcitation with red or violet light pulses (Figure 4.5a and Supporting Information at the end of this Chapter). In the simulated process, illumination with violet pulses potentiates the synaptic strength of the small neuron cluster connected to a particular orientation in timescales shorter than 200 ms (Figure 4.7b). Note that during the transient to a new orientation, red pulses are indispensable to inhibit the strength of synapses unrelated to the new position. Indeed, as shown in Figure 4.7b (middle panel) and Figure 4.11 (Supporting Information Sections 4.7.2, 4.7.3) the use of red pulses is crucial to speed up the inhibition of firing activity to timescales of a few 100s ms. Finally, Figure 4.7b displays the firing activity of the simulated neurons for the given threshold of synaptic strength. We stress that although we focus our discussion to two specific wavelengths, our results suggest that the full spectrum can be exploited to achieve causality between pairs of short-/long- wavelength pulses, with varying degrees of intensity of potentiation and depression (Figure 4.10 and Supporting Information Sections 4.7.2). Based on these observations, we propose that the transcription of optical flow from scenes captured in silicon retinas [135, 136] may be used in the LaAlO$_3$/SrTiO$_3$ system to emulate cognitive maps from temporally-correlated sensory inputs on the 100s millisecond range, comparable to timescales for perceptual recognition [150].

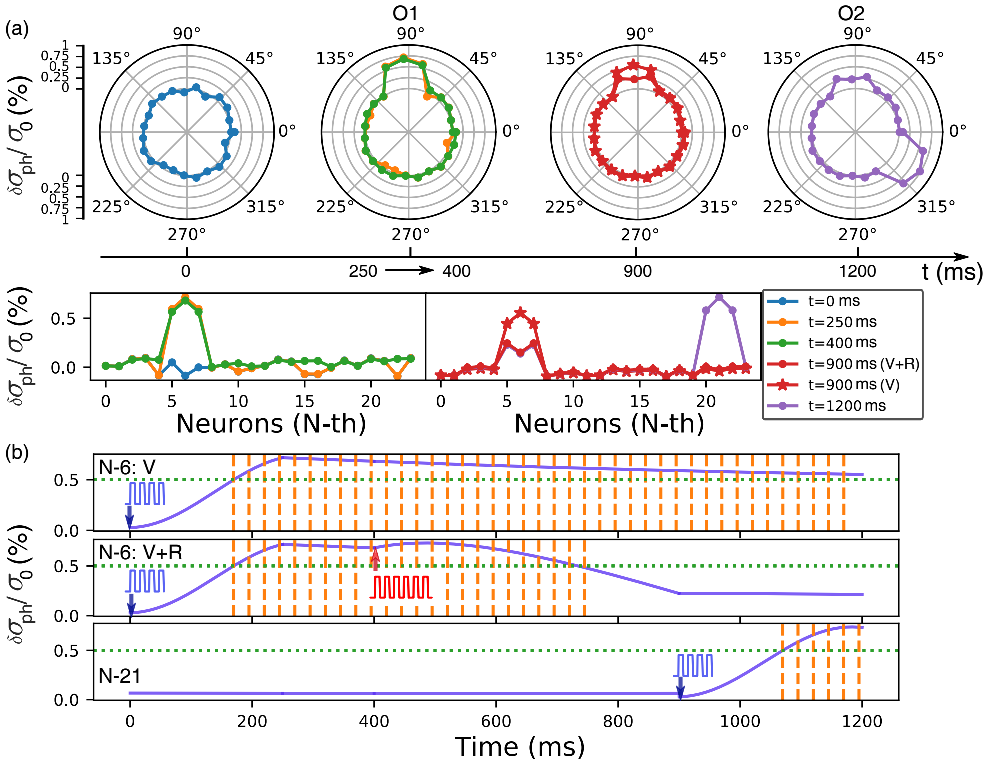

FIGURE 4.7: a) Radial and linear plots of the calculated synaptic strengths for two head movements (*O*1 and *O*2). c) Firing activity (vertical dashed lines) of selected simulated neurons for orientation *O*1, given the threshold of synaptic strength (dotted horizontal line), stimulated either using a single violet pulse (upper panel) or two-pulse sequences (middle panel). The lower panel displays the activity of a selected neuron for orientation O2.

4.5 Conclusion

We conclude by stressing that the results described here may profit from recent developments in artificial vision that, inspired by neurobiology, rely on image acquisition triggered *asynchronously* by per-pixel log-scale changes in brightness, which increase dramatically the dynamic performance by suppressing data redundancy [135, 136]. We envision that this progress, together with outstanding advances in silicon integrated photonics including the development of on-chip optical modulators and laser sources [151] provides a unique opportunity to use the kind of time-correlated plasticity described here to expand todays neuromorphic vision technologies. Interestingly for this context, the creation of two-dimensional electron systems in $LaAlO_3/SrTiO_3$ has been demonstrated on top of silicon [152]. Bearing these advances in mind, we envision that integrated electronic/photonic circuitry can be purposely designed to encode optic flow from neuromorphic retinas that can be used to build representation maps reminiscent of those that underpin the ability of self-localization and object motion detection in the brain [147].

4.6 Sample preparation and simulations

4.6.1 Sample Preparation

Using the aforementioned lithography processes (Chapter 2), Hall bars were defined with channel widths typically in the range $\sim 5 - 10\,\mu m$ and lengths $\sim 80 - 100\,\mu m$ (Figure 2.4). The conductive 2DES at the interface only emerges when $LaAlO_3$ films are above a critical value [153, 154]. Indeed, the lithography process is designed so that the 2DES is constrained within the Hall bars and, therefore, different Hall bridges defined in a same sample should be ideally isolated electrically. This point was checked out by measuring the resistance between contacts of different Hall bars. We also measured the temperature dependence of the resistance in the Hall bars, showing a metallic behavior all the way down to low temperatures (see one representative data in Figure 4.8). The measurements of the carrier density and mobility yielded values $n_s \approx 10^{13}\,cm^{-2}$ and $\mu \approx 1400\,cm^{-2}/s(\text{at}\,4\,K)$, respectively, comparable to those reported in the literature [153].

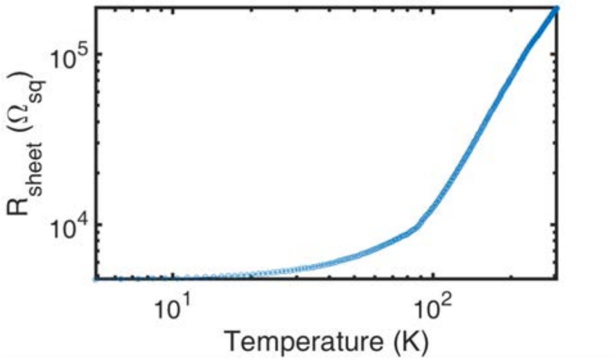

FIGURE 4.8: Temperature dependence of the sheet resistance measured along the Hall-bar of a 5 uc thick epitaxial $LaAlO_3/SrTiO_3$ interface.

4.6.2 Simulations of neural networks

The simulations of temporally correlated input sensory neurons (Figure 4.13) were performed using the Brian Simulator open source code, which is written in the Python programming language [95]. We considered the problem of replicating the firing activity patterns of neurons building cognitive maps in the brain. In particular, we focused on attractor map models for heads direction, where a small cluster of neurons spike at a given head orientation. Crucial to this point is the fact that the formation of cognitive maps in biological brains related to, e.g., spatial memory, self-location and self-motion in the environment require imperatively both excitatory and inhibitory actions on the synaptic strength [122, 133, 150]. This prerequisite suits well to the sort of potentiation and depression observed in our experiments using time correlated optical inputs.

4.7 Supporting Information

4.7.1 Structural characterization of epitaxial $LaAlO_3/SrTiO_3$ samples

We collaborate with J. Gazquez for structural measurements using transmission electron microscopy. Figure 4.9 shows an image captured using scanning transmission electron microscopy (STEM) from an epitaxial $LaAlO_3/SrTiO_3$ layer grown under identical conditions as the ones reported in the manuscript. This image was obtained using a high angle annular detector, giving Z-contrast imaging. Additionally, we acquired images from an annular bright field (ABF) detector, which allows the imaging of lighter elements, such as oxygen. With this technique we have been able to probe the distortions of A, B and O sub-lattices across the heterostructure. Figures S1a and S1b show a simultaneously acquired Zcontrast and ABF images of a 7 *u.c* thick $LaAlO_3$ layer grown on $SrTiO_3$, respectively. Both images were acquired along the [110]-zone axis in order to view the characteristic O octahedra rotation of the $LaAlO_3$ layer. The arrows mark the interface, formed at the boundary between the last TiO_2 plane of the $SrTiO_3$ substrate. A schematic view of $LaAlO_3/SrTiO_3$ interface with La in green, Al in blue, Sr in red and Ti in ellow is shown in Figure 4.9c.

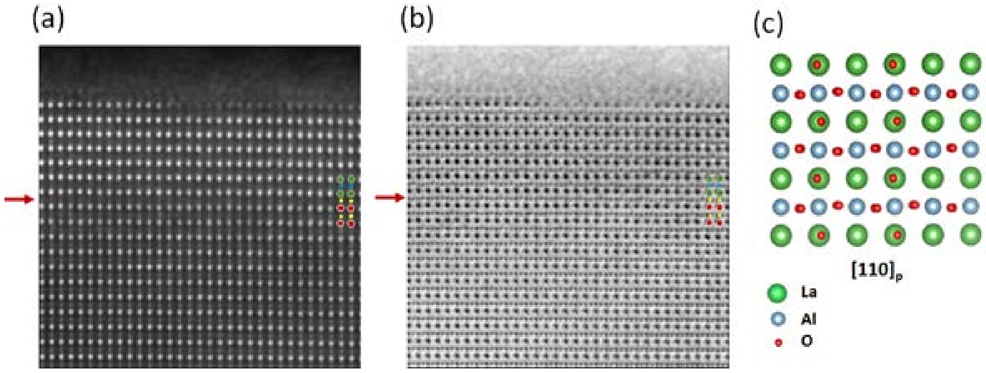

FIGURE 4.9: (a) and (b) show simultaneously acquired Z-contrast and annular bright field (ABF) images of a 7 *u.c* thick $LaAlO_3$ layer grown on $SrTiO_3$, respectively. Both images were acquired along the [110]-zone axis in order to view the characteristic O octahedra rotation of the $LaAlO_3$. Along this zone axis, the projection of this rotation appears as a O sub-lattice rippling, as can be seen in the ABF image. The arrows mark the interface, corresponding to the last TiO_2 plane of the $SrTiO_3$ substrate. (c) Schematic view along the [110]-zone axis of the $LaAlO_3/SrTiO_3$ interface with La in green, Al in blue, Sr in red and Ti in yellow.

4.7.2 Long-term depression of photoconductance induced by illumination with two-pulse sequences

As discussed in Section 4.3, the observed two-pulse temporal correlations depend critically on the inhibitory action of illumination with second pulses of wavelength longer (e.g., red) than the one used in the first pulse (violet). In these conditions, the measurements of the conductance after the second pulse show a decrease ($\Sigma^0 - |\Delta\Sigma^{(-)}|$) with respect to the conductance measured after the first pulse (Σ^0). This decrease depends on the wavelength used for the second pulse: the suppression of photoconductance is the largest for red, smaller for green and vanishingly small for blue (Figure 4.10a). As discussed in Chapter 3, this spectral dependence is assigned to resonant photoexcitation of surface states with red light, while blue or violet are off-resonance.

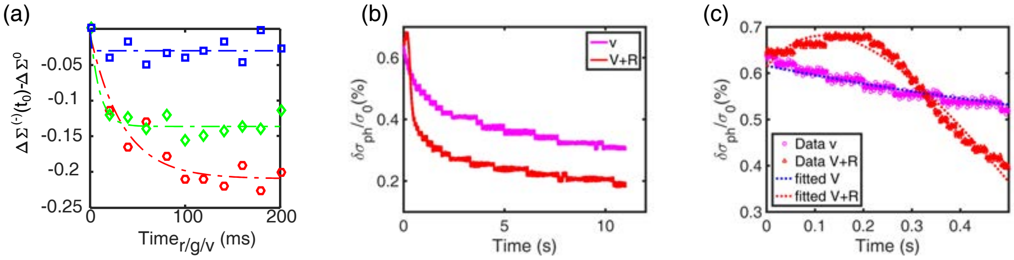

FIGURE 4.10: (a) Photoconductance measured after a single pulse of violet ($\Delta T_v = 40\,ms$) followed by red, green and blue pulses of varying duration ($\Delta T_{r,g,b} = 0 - 200\,ms$). The conductance is decreased after the second pulse from Σ^0 (just after the first pulse of violet) to $\Sigma^0 - |\Delta\Sigma^{(-)}|$ after the second pulse. The decrease in conductance, quantified by $\Delta\Sigma^{(-)}|$ measured at time $t_0 = 500\,ms$ after switching off the second pulse. We see that $\Delta\Sigma^{(-)}|$ depends on wavelength: the suppression is the largest for red, smaller for green and negligible for blue. (b) Time dependence of the photoconductance change obtained after a single pulse of violet ($\Delta T_v = 40\,ms$) and also after a two-pulse sequence of violet ($\Delta T_v = 40\,ms$) followed by red ($\Delta T_r = 60\,ms$). (c) The data shown in (b) are zoomed in around the initial time lapse after switching off the second pulse.

Figure 4.10b shows the time dependences of the photoconductance measured after a single pulse of violet ($\Delta T_v = 40\,ms$) and also after a two-pulse sequence of violet ($\Delta T_v = 40\,ms$) followed by red ($\Delta T_r = 40\,ms$). When we compare both curves we see that the illumination with red in the last step of the two-pulse sequence suppresses the conductance with respect to the value obtained with the one-pulse sequence. Figure 4.10c shows a zoom of the data displayed in Figure 4.10b around the initial time lapse after switching off the second pulse. We observe that after an initial overshoot, the conductance is steadily decreasing for time lapses $\Delta t > 300\,ms$. The data in Figure 4.10c is fitted to biexponential functions $\sigma = \sigma_0[Aexp(-\frac{t}{\tau_{dec,1}}) + (1-A)exp(-\frac{t}{\tau_{dec,2}})]$ used to fit the decay time of the photoconductance after illumination with violet or red light. The values of $\tau_{dec,1}$ and $\tau_{dec,2}$ are used for the simulations of leaky integrate-and-fire neurons described below.

The potentiation/depression caused by complementary pairs of short-/long-wavelength two sequence pulses is a phenomenon observed across the visible spectrum. To show this point, we carried measurements of the conductance after combinations of light pulses other than violet/red pairs. Figure 4.11 shows the change of photoconductance after one single pulse of green and after a two-pulse sequence of green followed by red. Figure 4.11b displays the change of photoconductance after a single pulse of blue and after two-pulse sequences of blue + green and blue + red. The data in Figure 4.11 shows that the two-pulse sequences of green + red and blue + red cause a strong suppression of conductance. Therefore, we conclude that the effect of time correlations of optical stimuli can be observed for a wide range of wavelengths across the spectrum, provided that appropriate pairs of short-/long-wavelength pulses are used.

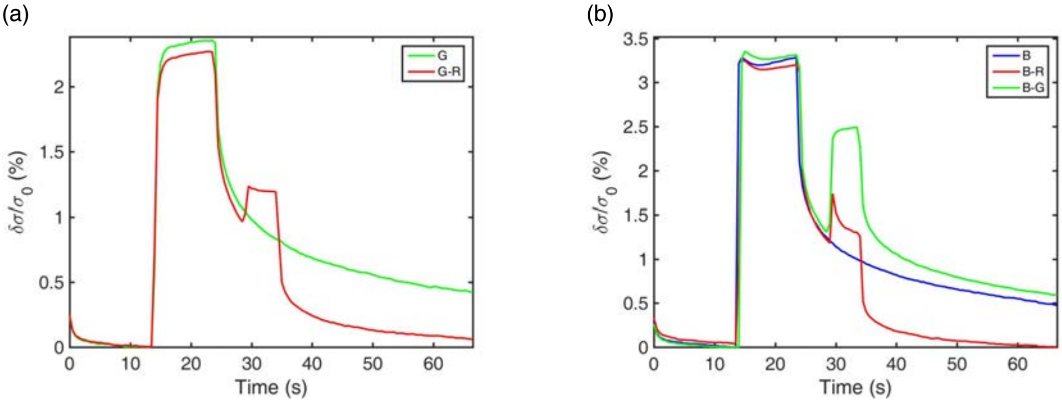

FIGURE 4.11: (a) Photoconductance measured after a single pulse of green (solid green line) and after a two-pulse sequence of green followed by red (solid red line). (b) Photoconductance after a single pulse of blue (blue line) and after two-pulse sequences of blue + green (green line) and blue-red (red line).

Note that the data of Figure 4.11 shows that wavelength-sensitive temporal correlations enable resetting the value of the conductance to the initial pristine state. This strategy can be also applied using shorter pulses, as shown in Figure 4.10b.

4.7.3 Simulations of neural networks

The simulations of temporally correlated input sensory neurons (shown in Figure 4.7) were performed using the Brian Simulator open source code, which is written in the Python programming language [95]. We considered the problem of replicating the firing activity patterns of neurons building cognitive maps in the brain. In particular, we focused on attractor map models for heads direction, where a small cluster of neurons spike at a given head orientation. Crucial to this point is the fact that the formation of cognitive maps in biological brains related to, e.g., spatial memory, self-location and self-motion in the environment require imperatively both excitatory and inhibitory actions on the synaptic strength [122, 133, 146]. This prerequisite suits well to the sort of potentiation and depression observed in our experiments using time correlated optical inputs.

The purpose of the simulations is to show that, based on the experimental data, causally correlated optical stimuli of violet and red pulses can be exploited to excite or inhibit selectively a collection of neurons that constitute the cognitive map. By way of exemplary illustration, we considered two consecutive neuronal firing patterns corresponding to successive head movements along two different orientations. The models are built on spiking input and output neurons. Two input neurons $i = 1, 2$ [corresponding to the causally correlated optical stimuli] send spikes at times $t_i^{(n)}$ to an output neuron O [linked to cognitive neural network]. By sending spikes, the input neurons modulate the output potential synaptic strength as follows:

$$u_0(t) = \sum_n \epsilon_{oi}(t - t_i^{(n)}) \tag{4.2}$$

where ϵ_{oi} is the contribution of input neurons i to the output potential strength of neuron O. Note that the value of ϵ_{oi} is related to changes in conductance after consecutive pulses of red and violet, and its value can be increased or decreased depending on their relative timings (Figure 4.6a in Section 4.4). Firing occurs whenever the strength $u_0(t_f)$ reaches a threshold value $\theta$from below at time t_f

$$u_0(t_f) = \theta \tag{4.3}$$

whereby the output neuron O sends a spike at that time. In Figure 4.13 spike events are separated by 20 ms, which is comparable to the refractory time found in biological neurons. An important point is that calculations take care of the time dependence of the conductance after photoexcitation. As shown in Figure 4.6a in Section 4.4, after photoexcitation the conductance decays with time, which has to be taken into account in the calculations. This is done by fitting the experimental data as shown in Figure 4.10c. In our case, we use bi-exponential functions $\sigma = \sigma_0[Aexp(-\frac{t}{\tau_{dec,1}}) + (1-A)exp(-\frac{t}{\tau_{dec,2}})]$ to fit the decay time and the values of $\tau_{dec,1}$ and $\tau_{dec,2}$ are used for the simulations of leaky integrate-and-fire neurons.

The simulations of two consecutive head movements (O1 and O2) are encoded as follows:

(1) All synaptic strengths are set initially to an arbitrary random noise level, well below the threshold θ (2) A small cluster collection of synaptic strengths are selectively excited with short pulses of violet to raise their value above the threshold θ (so that they indicate the heads direction along $O1$), while the rest remain with the initial random values. The long-term potentiation is based on the experimental data obtained from the changes of conductance after illumination with violet pulses (upper panel of Figure 4.6a in Section 4.4), and is mathematically expressed as:

$$\epsilon_{oi}(t) = a_{pot}[b_{pot}exp(\frac{t}{\tau_{pot,1}}) + (1-b_{pot})cos(\frac{t}{\tau_{pot,2}})] \tag{4.4}$$

where a_{pot}, b_{pot} , $\tau_{pot,1}$ and $\tau_{pot,2}$ are determined from fittings to the experimental data. The parameters are a bit different for the varying duration of violet pulses (Figure 4.12c). The cosine function is considered due to the application of the periodic pulsed light. In the simulation, neuron-6 is excited by 40 ms violet pulses, while the neurons 5 and 7 are excited by 20 ms violet pulses. In this way, we end up with a small cluster of firing neurons with their synaptic strength above threshold, signalling orientation $O1$ (Figure 4.12).

(3) At the end of the short violet pulses, the excited synaptic strengths evolve with time, decaying in intensity according to:

$$\epsilon_{oi}(t) = a_{dec}\left[b_{dec}e^{-t/\tau_{dec,1}} + (1-b_{dec})\,e^{-t/\tau_{dec,2}}\right] \tag{4.5}$$

where a_{dec}, b_{dec} , $\tau_{dec,1}$ and $\tau_{dec,2}$ are determined from fittings to the experimental data.

(4) After exciting the neuron cluster for orientation $O1$, the following steps are taken to depress the synaptic strengths related to orientation $O1$ so that their firing activity ceases and to excite the cluster corresponding to orientation O2. This is done by the action of two serial actions:

(4a) Red pulses are applied to those synapses that were excited for the orientation along $O1$. The timings of red pulses required to depress the synapse strength are taken from experiments

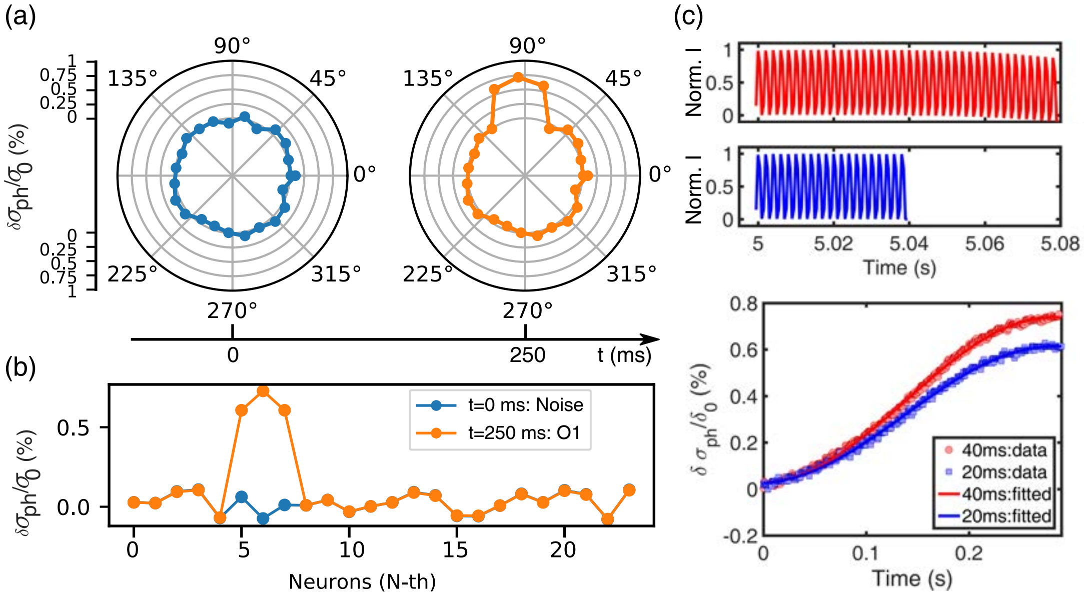

FIGURE 4.12: (a) and (b) show the synaptic strengths in radial and linear plots, respectively, of the simulated neurons for orientation O1 on the timescale of 250 *ms*. (c) The upper panel shows the normalized intensity after reflection on the sample surface (Norm. I) measured for a train of violet pulses with different durations, 40 *ms* (red) and 20 *ms* (blue). The lower panel shows the corresponding photoconductance changes over time, with a fitting to Equation 4.4. The results of this fitting are used in the simulations to calculate the photoconductance evolution over time.

(lower panel of Figure 4.5a in Section 4.4). The depression process is based on:

$$\epsilon_{oi}(t) = a_{dep} + b_{dep,1} e^{-t/\tau_{dep,1}} + b_{dep,2} e^{t/\tau_{dep,2}} \tag{4.6}$$

where a_{dep}, $b_{dep,1}$, $b_{dep,2}$, $\tau_{dep,1}$ and $\tau_{dep,2}$ are determined from fittings to the experimental data of violet plus red pulses. We stress the extreme relevance of using the depression of conductance induced by red pulses after violet. Without this time causality it would not be possible to quench rapidly the synaptic strength below the threshold value. This is visualized in Figure 4.13, which shows the firing activity of one of the spiking O1 output neurons. If not depressed by the action of red pulses, the synaptic strength only decays to the threshold value after periods of $time \gg 1$ second. On the contrary, after pulsing with red light, the firing activity of the O1 neuron can be stopped in the range of 100s milliseconds, providing the means of exciting and inhibiting the synaptic strengths on timescales comparable to those of biological perceptual recognition.

(4b) The output neuron cluster related to orientation $O2$ is excited according to the equation 4.5. Finally we end up with a small output neuron cluster corresponding to heads direction along $O2$.

Firing activity patterns resulting from these simulations are displayed in Figure 4.7b in Section 4.4.

4.7.4 Emulation of inhibitory synapses with two-pulse sequences

After photoexcitation with a single pulse of violet light, the conductance decays slowly with time, which typically would require timescales of several seconds to suppress the firing activity (Figure 4.13a). To emulate the coexistence of excitatory and inhibitory synapses we thus need to speed up significantly the suppression of conductance. This can be achieved by illuminating with red pulses after violet. Figure 4.13b shows that, for the given threshold of synaptic strength, the suppression of the firing activity of neurons can be achieved on the scale of a few 100's of millisecond, much faster than it would be just relying on the time decay of photoexcitation of a single pulse of violet (Figure 4.13a).

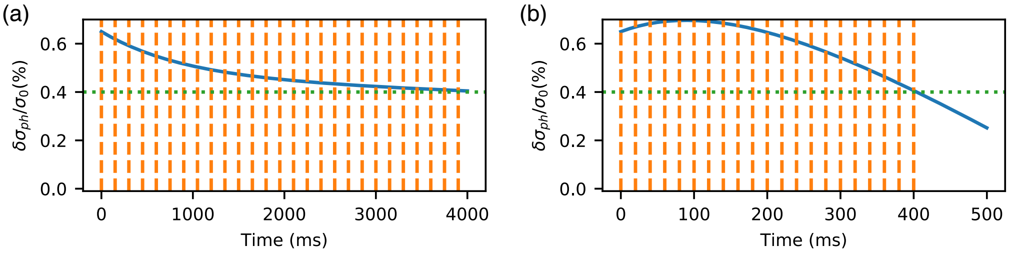

FIGURE 4.13: Here we represent over time the firing activity of a selected simulated neuron in two situations: (a) the synaptic strength is excited with a single pulse of violet light ($\Delta T_v = 40\,ms$) and it decays slowly after photoexcitation. Correspondingly, the firing activity persists for timescales of many seconds; (b) the synapse is illuminated with a two-pulse sequence of violet followed by red ($\Delta T_v = 40\,ms$, $\Delta T_r = 60\,ms$), which enables stopping the firing activity within a few hundreds of milliseconds. The solid lines show the evolution of synaptic strength. The horizontal dotted lines indicate the threshold value of synaptic strength to trigger the firing activity. The vertical dashed lines represent the spiking times.

4.7.5 Photoconductive spectral response of epitaxial versus amorphous interfaces

We have measured the spectral photoconductive response of amorphous $LaAlO_3/SrTiO_3$ interfaces using the same method used for epitaxial interfaces. This way, Hall bar devices were prepared using an optical lithography process similar to that described for epitaxial samples. For that purpose, a layer of photoresist S1813 was spin-coated on as-received (001) oriented $SrTiO_3$ substrates, using the same conditions of exposure and the same developer as described for the epitaxial interfaces (see the Experimental Section 4.3 and Figure 4.10). The main difference is that the exposed areas were defined as Hall-bar shapes instead of boundaries. At the last stage amorphous $LaAlO_3$ layers of thickness $3-6\,nm$ were deposited at room temperature by pulsed laser deposition with oxygen partial pressure $P_{O_2} = 10^4\,mbar$, laser repetition rate $1\,Hz$, substrate-target distance $55\,mm$, and laser pulse energy and fluence of about $26\,mJ^2$ and $1.5\,J/cm^2$, respectively. Note that in this process the photoresist surrounding the Hall bars was not removed. In these samples, two dimensional maps where acquired, where the photoconductive response was mapped against wavelength, irradiance and pulse width. Figure 4.14 b shows the tunability of the photoconductance by exposing the sample to light pulses of different timespans. In particular, Figure 4.14b shows the changes in photoconductance $\delta\sigma_{ph}(t)/\sigma_0$ measured at different probing times as a function of the cumulated illumination time, showing a spectral dependence that is smoother that the one corresponding to epitaxial samples (Figure 4.2). In particular, the magnitude of the photoconductance follows a gradual evolution across visible wavelengths. As argued in Chapter 3, we hypothesize that the photoconductance observed for the epitaxial interface arises from the interplay between electrostatic boundary conditions of the epitaxial $LaAlO_3$ layer and the formation energy of interface defects. Such electrostatic boundary effects are critically dependent on the epitaxial character of the crystalline structure of $LaAlO_3$. Obviously, these mechanisms are absent in the amorphous $LaAlO_3$ layer, which may explain also the different spectral photoconductance dependence observed for the amorphous layers.

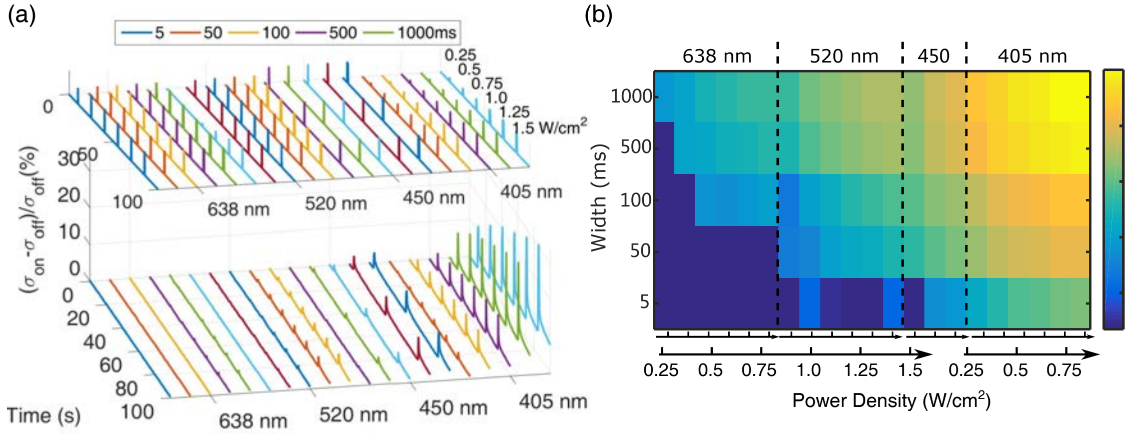

FIGURE 4.14: (a) Photoconductance of an amorphous $LaAlO_3/SrTiO_3$ interface measured under illumination with trains of pulses of different width ($\approx 5 - 1000\,ms$) and irradiance ($0.25 - 1.25\,W/cm^2$). (b) Two-dimensional map where the photoconductive response is mapped against wavelength, irradiance and pulse width.

4.7.6 Reproducibility of photoconductance response

We discuss the reproducibility of the changes of conductance with light for experiments repeated under identical conditions. With this in mind, we show in Figure 4.15 the photoconductance measured after illumination of three consecutive nominally identical light pulses, responding to violet light of cumulated time of 40 milliseconds. Due to the plastic photoconductance response, the initial conductance state before each of the three measurements is different (see Figure 4.15a), so that the measured values of conductance differ between experiments. Nevertheless, although the three measurements displayed in Figure 4.15a started at different initial conductance states, the normalized photoconductance, quantified as $a\frac{\sigma_{ph}}{\delta_0} = \frac{\sigma_{ph} - \sigma_0}{\sigma_0}$, shows little variation (Figure 4.15b), underlining the stability and reproducibility of the experimental data. We can evaluate the error bar at each recorded point $n = 1, \cdots,$ (corresponds to the number of records across the whole interval of time) for experiment J as $\delta_{n,j} = max|L_{j,n} - L_{j\neq j,n}|$, where $L_{j,n}$ represent the dataset of the three consecutive experiments $i = 1, 2, 3$. Figure 4.15c presents the data corresponding to the experiment $L_{2,n}$, including the set of error bars $\delta_{n,2}$. The inspection of Figure

4.15c reveals that the error as defined previously is $|\delta_{n,2}| < 5\%$ for the whole range of measured the data.

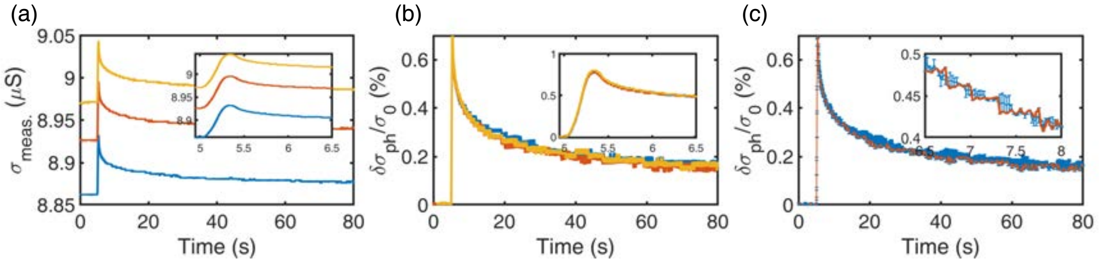

FIGURE 4.15: (a) As-measured conductance of the $LaAlO_3/SrTiO_3$ interface for three consecutive identical runs of experiments, each responds to a pulse of viole light of 40 milliseconds of cumulated time. The inset shows a zoom around initial time stages. (b) The data of panel (a) is plotted as normalized photoconductance $\delta\sigma_{ph}(t)/\sigma_0$, with the inset showing initial time stages. (c) The data of experiment run $L_{2,n}$is plotted together with error bars calculated as described in the text. The inset shows a zoom of the data.

4.7.7 Time relaxation of conductance after photoexcitation

In our experiments, the relaxation time of the conductance after photoexcitation with millisecond rage pulses is in the order of tens of seconds (Figure 4.16). This is two orders of magnitude larger than the timescales for biological perceptual recognition. Alternatively, the timescales of our simulations to model cognitive-like maps using experimental data are also much shorter than the relaxation time of the photoconductance. As expected, illumination with long wavelength pulses leads to a drastic reduction of the time constant (Figure 4.16).

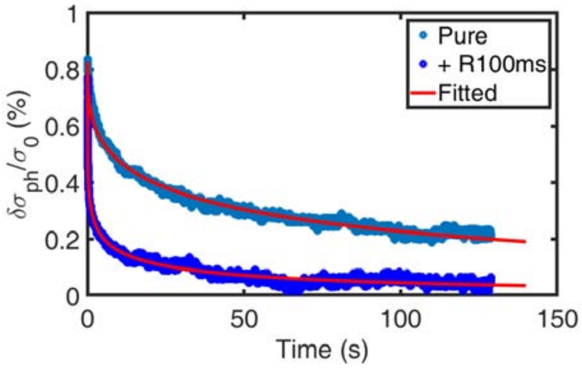

FIGURE 4.16: Conductance changes after photoexcitation with a single violet pulse (50 milliseconds) and a two-pulse sequence of violet (50 milliseconds) plus red (100 milliseconds). The solid lines are a fitting to an extended exponential function given by $A_0 exp[-(\frac{t}{\tau})^k]$. The relaxation time extracted from the fittings is: 50.5 seconds for a single violet pulse. As expected, when violet is followed by red, the depression of the conductance induces and drastic reduction of the time constant to $\tau \approx 1.6\,s$.

The value of the time constant after photoexcitation is relevant in regard to the classification of the synaptic potentiation/depression as long- or short- term. We stress that the boundary classification into long-term and short-term effects in synaptic weight is not well-defined and should be considered with respect to the timescale required for a specific task [121]. If changes in synaptic weights are much longer than timescales necessary to do a specific task, then the potentiation/depression of synapses can be considered effectively long-term. In this respect, as the observed relaxation times observed in the photoconductance are typically above two orders of magnitude longer than specific tasks (e.g., perceptual recognition or formation of cognitive maps), we can consider that the changes of the synaptic strength driven by wavelength-sensitive time-correlations of the optical pulses are effectively long-term.

4.7.8 Voltage readouts in photoconductance measurements

The conductance was measured by injecting currents, typically $I \approx 1\mu A$, and changes in conductance were inferred from changes measured in the output voltage. Figure 4.17 shows a typical experiment in which two datasets are displayed, corresponding to two two-pulse sequences, namely, (violet 95 ms + red 5 ms) and (violet 20 ms + red 80 ms). As expected from the studied wavelength-correlated photoresponses, longer exposure to red light after illumination with violet leads to a lower value of the relative photoconductance (Figure 4.17a). Relative changes in conductance are in the order of 1%. As mentioned above, the changes in conductance are detected by measuring changes of the output voltage, which are shown in Figure 4.17b for the data displayed in Figure 4.17a. We see that voltage readings vary in the millivolt range, and the noise is much smaller than the detected changes in voltage.

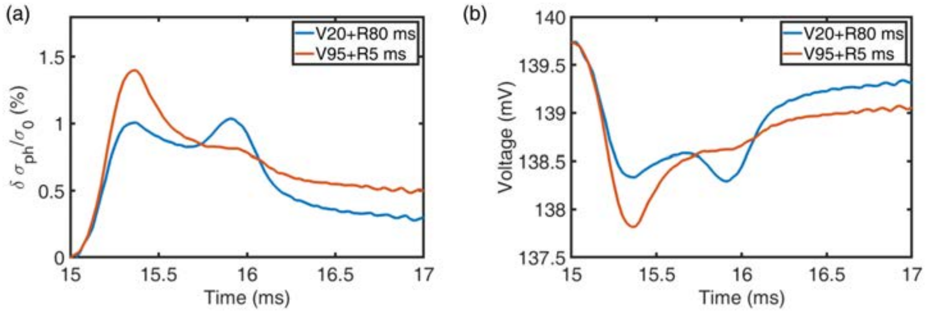

FIGURE 4.17: (a) Relative changes of conductance after two two-pulse sequences consisting, respectively, of (violet 95 ms + red 5 ms) and (violet 20 ms + red 80 ms). (b) Voltage output detected in the experiments displayed in panel (a).

4.7.9 Conductance modulation under multiple-pulse sequences

The data displayed in Figure 4.18 corresponds to a sequence of blue and red pulses of width 50 ms and irradiance 1 W/cm^2. The blue curve shows the changes of conductance after a sequence of multiple blue pulses, leading to a global increase of conductance at the end of the whole sequence. We repeated the experiment, but now combining blue and red pulses with the same width and timing as the all-blue pulse sequence (red curve in Figure 4.18). We observe in this Figure that the illumination of the first red pulse after the first blue pulse entails a significant decrease of conductance with respect to the first blue pulse, in agreement with all the experiments described in the manuscript. Interestingly, a subsequent red pulse decreases even more the conductance with respect to the first red pulse. Therefore, the decrease after different red pulses is cumulative. As expected, the next two blue pulses increase substantially the conductance and, finally, the third and last red pulse decreases once more the conductance. A comparison between the multiple all-blue and blue/red pulses (blue and red curves in Figure 4.18, respectively) shows that appropriate combinations of short-/long- wavelength pulses can fine-tune the conductance.

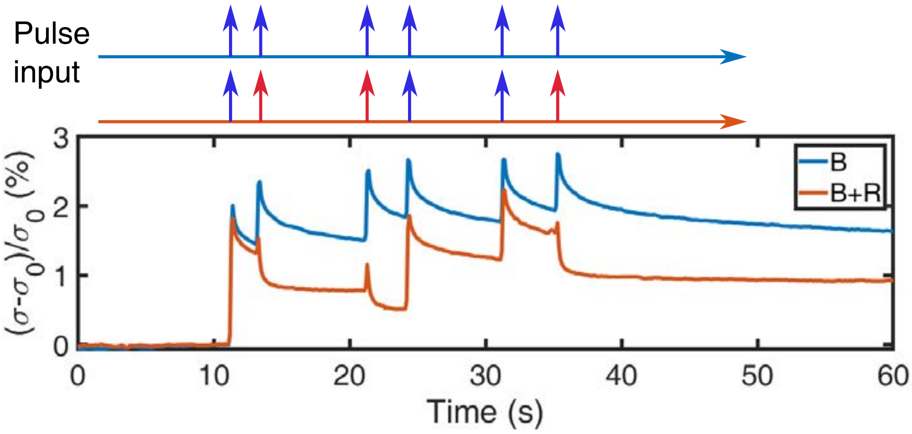

FIGURE 4.18: Relative changes of conductance after two different multiple-pulse sequences. All pulses have a width of 50 ms, and the irradiance is 1 W/cm^2 and their timing is represented schematically in the upper part of the figure. The blue curve in the figure corresponds to conductance changes induced by multiple an all-blue-pulse sequence, while the red curves displays the photoconductance measured under multiple blue/red-pulse sequence.

Chapter 5

Plasticity of persistent photoconductance of amorphous $LaAlO_3/SrTiO_3$ interfaces under varying illumination conditions

---

In Chapters 3 and 4 we have analyzed the wavelength-dependent time-correlated photoresponses of the epitaxial $LaAlO_3/SrTiO_3$ interface. In Chapter 4, we have explored the potential of these responses to emulate some brain-inspired functionality based on the spiking time-dependent plasticity model (STDP). Understandably, a large sensitivity to enviromental illumination conditions is desirable for any application. Facing this issue, we have explored the sensitivity of amorphous $LaAlO_3/SrTiO_3$ interfaces to different luminance conditions, as generally, photoresponses of amorphous layers are larger than those of epitaxial interfaces. We note that, although STDP-like photoresponses are absent in amorphous layers, the plasticity is nonetheless still present, and could find interest for some applications.

5.1 Abstract

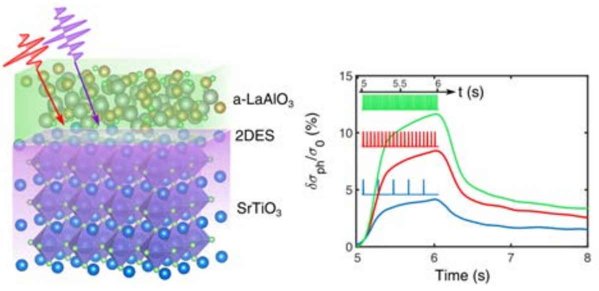

We report on electric transport measurements under optical stimulation of the persistent photoconductance (PPC) at the interface between amorphous $LaAlO_3$ thin films and $SrTiO_3$ single crystals. The spectral response of PPC in the visible was analyzed under varying illumination conditions and exposure times down to the milliseconds range. The PPC is plastically modulated by optical stimuli of varying strength and duration, demonstrating fine-tuned photoconductive responsivity over a diversity of cumulated timespans. Interestingly, under optimal conditions, illumination

over periods on the second timescale the photoconductance is sensitive to intensity contrasts under conditions comparable to bright-sunlight environments. The prospects of exploiting photoconductance − including potential strategies to reach higher sensitivity to dimmer environmental conditions− are discussed in this chapter.

5.2 Introduction

As discussed in Chapter 1, Section , the two-dimensional electron system (2DES) emerging at the $LaAlO_3/SrTiO_3$ interface shows a variety of properties, including high electrical mobility [63], two-dimensional superconductivity [64] and strong Rashba spin-orbit fields [155]. The epitaxial $LaAlO_3/SrTiO_3$ heterostructure, where the mechanism for the generation of the metallic interface is driven by electrostatic boundary conditions [123] , has grabbed most of the attention. Interestingly, a 2DES can be also generated at the interface between amorphous $LaAlO_3$ (a-$LaAlO_3$) films and $SrTiO_3$ single crystals due to the creation of oxygen vacancies which act as electron donors under the reductive conditions during the growth [156–158]. In spite of the different origins, similar transport properties are observed in both systems, e.g., the values of electron mobility are comparable for both epitaxial and a-$LaAlO_3/SrTiO_3$ interfaces [159] . This raises the interest in amorphous interfaces, as the sample preparation can be done at room temperature, enabling an easier integration into well-developed semiconductor technologies.

In this chapter, we analyze the properties of a-$LaAlO_3/SrTiO_3$ interfaces in relation to its persistent photoconductance (PPC) [67]. As presented in Subsection 1.3.3, this is a phenomenon observed in many other semiconductors and two-dimensional systems [91, 160], whereby the conductance is increased after excitation with visible or ultraviolet light, so that the initial value prior to the photoexcitation is only fully recovered after prolonged periods of time [87, 92]. PPC has been studied in both epitaxial [67, 161–163] and amorphous interfaces [90], and different physical mechanisms have been proposed for each type of interface, being oxygen vacancies suggested playing a fundamental role in a-$LaAlO_3/SrTiO_3$ interfaces[90]. In Chapter 4 we have explored the potential to exploit the PPC modulation to emulate the plasticity of biological synapses using optical inputs as stimuli, as proposed for other materials [58, 164–166]. This would be of interest in photonic circuits where integrated light sources may be exploited to drive plastic photoresponses. Alternatively, artificial retinas [167] would also benefit from incorporating plastic photoresponses [168]. In contrast to other neuromorphic developments, this particular application would require sensitivity to ambient illumination in visual scenes.

Here we focus our study to the a-$LaAlO_3/SrTiO_3$ interface to seek the sensitive threshold and find that, under optimal conditions, this system is sensitive to contrasts approaching the peak of solar terrestrial irradiance. Although this threshold forbids the application in dynamic sensing of natural scenes, it could be of interest for other applications where this limitation is less severing, as in recognition of quasi-static visual patterns of large enough irradiance or as photoresponsive synaptic elements in integrated photonic systems, where non-natural light sources are used for optical stimulation. In this respect, the simplicity of a-$LaAlO_3/SrTiO_3$ sample preparation can be an important asset for its integration into existent semiconductor technologies.

5.3 Experiment

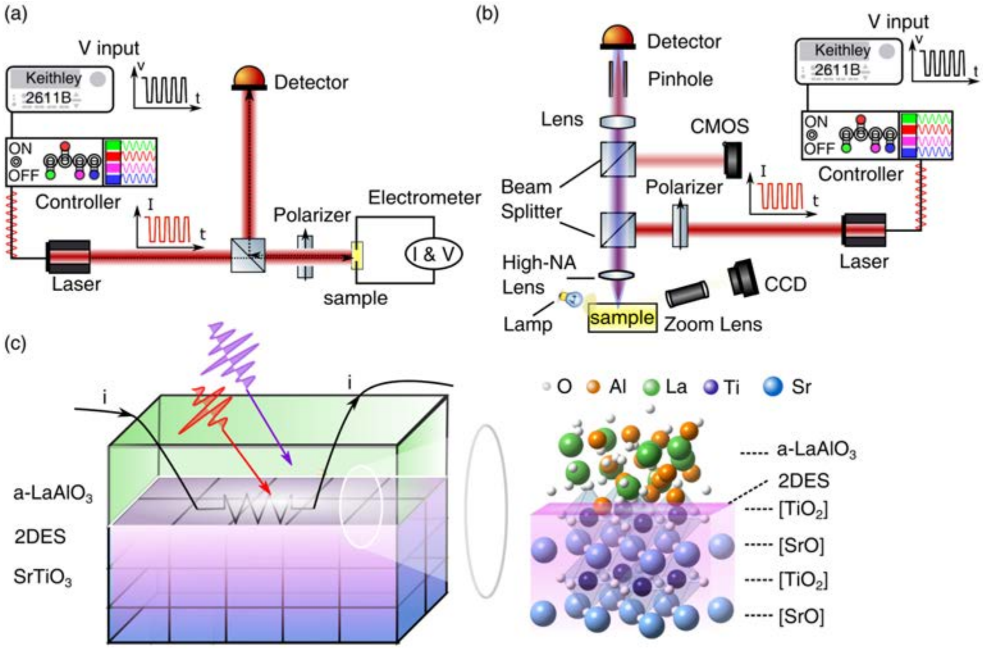
(a)
V input
Keithley 2611B
ON
OFF
Controller
Laser
Detector
Polarizer
Electrometer
I & V
sample
(b)
Detector
Pinhole
Lens
CMOS
Beam Splitter
Polarizer
Controller
Laser
V input
Keithley 2611B
High-NA Lens
Lamp
sample
Zoom Lens
CCD
(c)
i
a-LaAlO3
2DES
SrTiO3
O Al La Ti Sr
a-LaAlO3
2DES
[TiO2]
[SrO]
[TiO2]
[SrO]

FIGURE 5.1: (a) Sketch of the experimental setup used to measure the photoconductance of a-$LaAlO_3/SrTiO_3$ under direct illumination. Appropriate instrumentation is used to generate short pulses of light of different wavelengths (violet, blue, green, red). The polarizer is used to vary the illumination on the sample. The voltage is measured under illumination. The intensity of reflected light is measured by a photodetector. (b) In some experiments, the photoconductance is also measured by illuminating the sample through a high-numerical-aperture lens. The CCD camera is used to locate the beam spot on the sample, while a CMOS detector is used to adjust the focus location along the out-of-plane direction. (c) Crosssectional view of the amorphous $LaAlO_3/SrTiO_3$ interface.

All things considered, this work is intended to explore the sensitivity of the PPC in a-$LaAlO_3$/ $SrTiO_3$ to short pulses of light down to millisecond timescales under varying illumination conditions approaching terrestrial conditions of solar irradiance. The tunability of the conductance is also analyzed by measuring the cumulative effect of optical stimuli on the plastic PPC response. With this in mind, we contacted the interface between the amorphous $LaAlO_3$ layer and the $SrTiO_3$ substrate by Al wire bonding (Figure 5.1 (c)). Amorphous layers with thickness $3-6\,nm$ were deposited at room temperature by pulsed laser deposition in an oxygen partial pressure $P_{O_2} = 10^4\,mbar$. The conductance was measured with injected currents typically in the range of $I \approx 1\,\mu A$ for lower resistance devices ($R < 10^6\,\Omega$) or $I \approx 1nA$ for higher resistance ($R > 10^6\,\Omega$) . The photoexcitation experiments were carried out at room temperature using lasers of different wavelengths in the visible red ($\lambda = 638\,nm$), green ($\lambda = 520\,nm$), blue ($\lambda = 450\,nm$) and violet ($\lambda = 405\,nm$). Under direct illumination conditions (Figure 5.1 (a)), the laser beam was steered via a mirror directly towards the sample, illuminating an area of size $1cm2$ and the irradiance on the sample was varied in a range of values down to $P_w \approx 2.5W \cdot nm^{-1} \cdot m^{-2}$ (see Section 2.2.2 for the determination of the output bandwidth of the laser source and the illuminance in units of $nm^{-1} \cdot m^{-2}$). This value is relatively close to the peak of solar spectral irradiance in the visible at ground level ($\approx 1.4 - 1.6\, W \cdot nm^{-1} \cdot m^{-2}$ for green light) [169]. Alternatively, high focusing through a high-numerical-aperture objective was also performed in some experiments (Figure 5.1 (b)).

5.4 Plastic photoresponse of amorphous $LaAlO_3/SrTiO_3$ interfaces

We first discuss the impact on the photoconductance of the change in transport properties over time, which is known to occur in a-$LaAlO_3/SrTiO_3$ interfaces [170]. The origin of these changes can be traced back to the refilling of oxygen vacancies by dissociation of O_2 molecules from the environment, resulting in a continuous and gradual decrease of conductance over long periods [170]. As expected, the same phenomenon is also present in our samples, as confirmed by monitoring the resistance over a timescale spanning up to $\Delta t \approx 2 \times 10^7\, s$ ($\approx$ 8 months) after the time of growth. The results, plotted in Figure 5.2 (a), show that the resistance measured in darkness goes from an initial value $R \approx 6 \times 10^4\, \Omega$ up to $R \approx 8 \times 10^8\, \Omega$ about eight months later, exhibiting a highly nonlinear dependence on the time elapsed from growth (aging time in Figure 5.2 (a)). Importantly, these effects influence the photoconductance, which also changes shows a highly nonlinear increase due to aging. To see this, we measured the relative change of conductance with illumination quantified as $\frac{\delta\sigma_{ph}(\tau_{il})}{\sigma_0} = \frac{\sigma_{ph}(\tau_{il}) - \sigma_0}{\sigma_0}$, where σ_0 is the initial conductance and$\sigma_{ph}(\tau_{il})$ denotes the conductance measured immediately after being illuminated through a time τ_{il} (illumination time). Figure 2a plots the values of $\frac{\delta\sigma_{ph}(\tau_{il} = 10s)}{\sigma_0}$ measured with irradiance $P_w \approx 10^3\, W \cdot nm^{-1} \cdot m^{-2}$ at different wavelengths and aging times $\leq 2 \times 10^7\, s$. The inspection of this Figure reveals a remarkable enhancement of $\frac{\delta\sigma_{ph}(\tau_{il})}{\sigma_0}$ with strong nonlinear dependence on the aging time (see also Figure 5.2 (b)). Indeed, as we discuss below, the rapid growth of the photoconductance due to aging also increases the sensitivity to illumination contrast of optical stimuli, which is beneficial for applications aimed at sensing visual inputs from the environment. We stress that the strong increase of the relative conductance is due to the large decrease with aging of the initial conductance σ_0 . This observation is born out in Figure 5.2 (c), where the absolute changes of conductance, i.e., not normalized to the initial value σ_0, are shown. Clearly, with increased resistance the absolute changes are much smaller than for fresher samples with lower resistance. Nevertheless, as discussed below, in spite of the much smaller value of $\frac{\delta\sigma_{ph}(\tau_{il})}{\sigma_0}$, the rapid growth of the normalized photoconductance $\frac{\delta\sigma_{ph}(\tau_{il})}{\sigma_0}$ due to aging also is correlated with an increasesd the sensitivity to illumination contrast of optical stimuli, In the ensuing discussion we will refer to $\frac{\delta\sigma_{ph}(\tau_{il})}{\sigma_0}$ rather than $\delta\sigma_{ph}(\tau_{il})$.

At this point it is important to observe that the phenomenon of persistent photoconductance has been observed in a wide range of semiconductors, where it is widely accepted to be caused by DX-centers [87, 92]. As discussed in Section 1.3.3, DX-centers are defect states due to, e.g., interstitials or vacancies, that induce donor states that are coupled to the lattice. Changes in the in the occupancy of such states induced by light may cause large lattice relaxations in the lattice around the defects. Thus, when one electron leaves behind the defect state, the structural relaxation prevents the return of the carrier to the initial state after photoexcitation, causing the

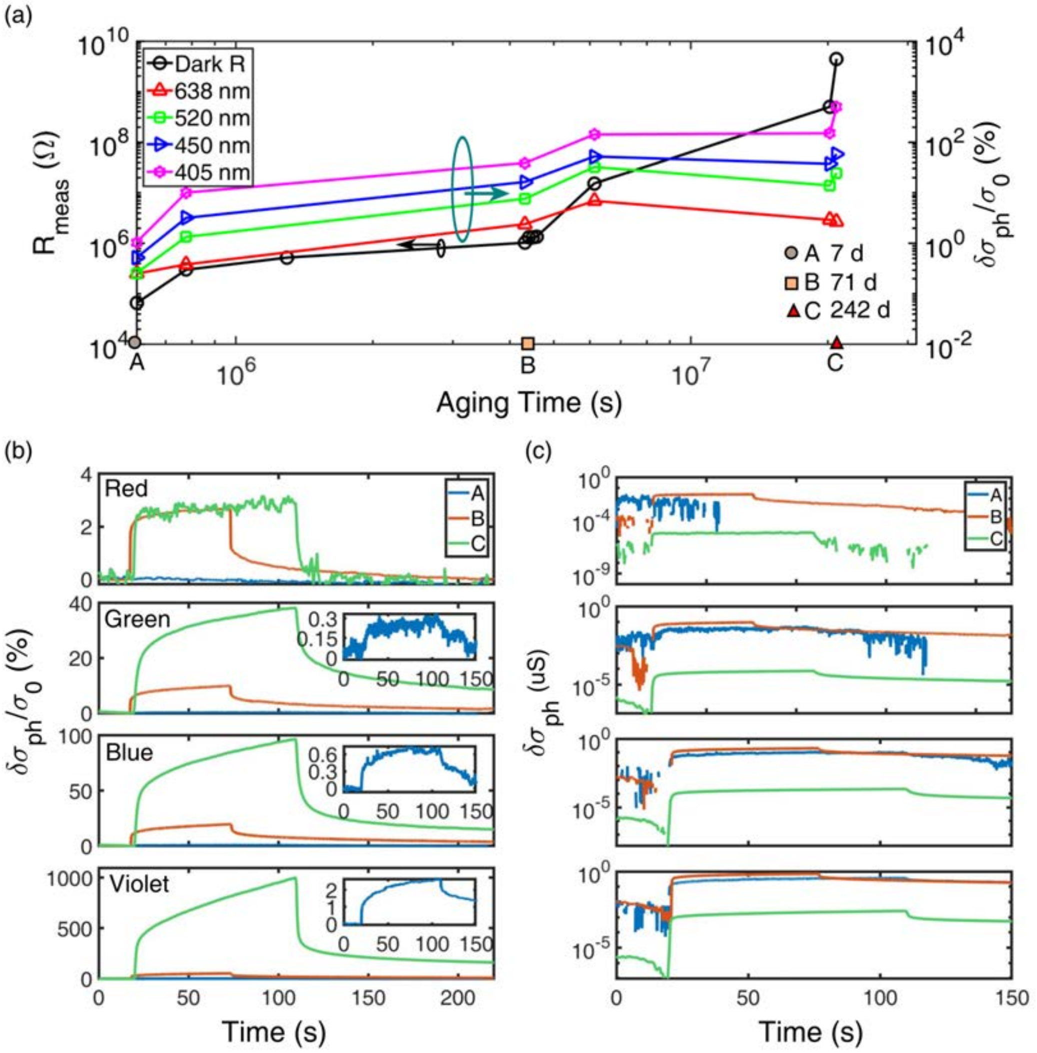

FIGURE 5.2: (a) Resistance measured in darkness (black circles) at different times elapsed from the deposition of the amorphous LaAlO$_3$ layer (up to roughly 8 months). The figure also includes the photoconductance $\frac{\delta\sigma_{ph}(\tau_{il})}{\sigma_0}$ measured at different wavelengths under illumination time $\tau_{il} = 10\,s$. The steady nonlinear increase of resistance and photoconductance is related to the aging of the amorphous LaAlO$_3$/SrTiO$_3$ interface, plausibly because of refilling of oxygen vacancies by dissociation of O$_2$ molecules from the environment. (b) Time dependence of the conductance under illumination of irradiance $P_w \approx 10^3\ W \cdot nm^{-1} \cdot m^{-2}$ and different wavelengths. A, B, and C refer to different aging times indicated in panel (a). The strong nonlinear increase of photoconductance caused by aging is shown in these figures. The insets display a zoom of the photoconductance at aging time A. (c) Plot of the absolute changes of conductance ($\delta\sigma_{ph}(\tau_{il})$) corresponding to the data in (b).

persistent change in conductance. Note that the decrease of the absolute value of photoconductance observed in high-resistance samples ($\delta\sigma_{ph}(\tau_{il})$ in Figure 5.2 (c)) is compatible with the identification of oxygen-related vacancies as DX-centers. More specifically, a reduction of vacancies due to aging should cause a decrease of active DX-centers, so that the absolute change of conductance would be smaller, as observed in the experiments (Figure 5.2 (c)).

Before proceeding, we note that a control of the aging process is needed to reach a stable state, preventing further evolution of the transport properties with time. Interestingly, a possible strategy towards this objective may be provided by the observation that the deposition of an additional a-$LaAlO_3$ film grown at a O_2 pressure higher than that used for the first a-$LaAlO_3$ layer reduces the aging process by orders of magnitude [170], which could be a promising route to achieve the required stability. Importantly, growth conditions e.g., oxygen pressure or the thickness of the amorphous layer can be used to control the resistance state of the sample.

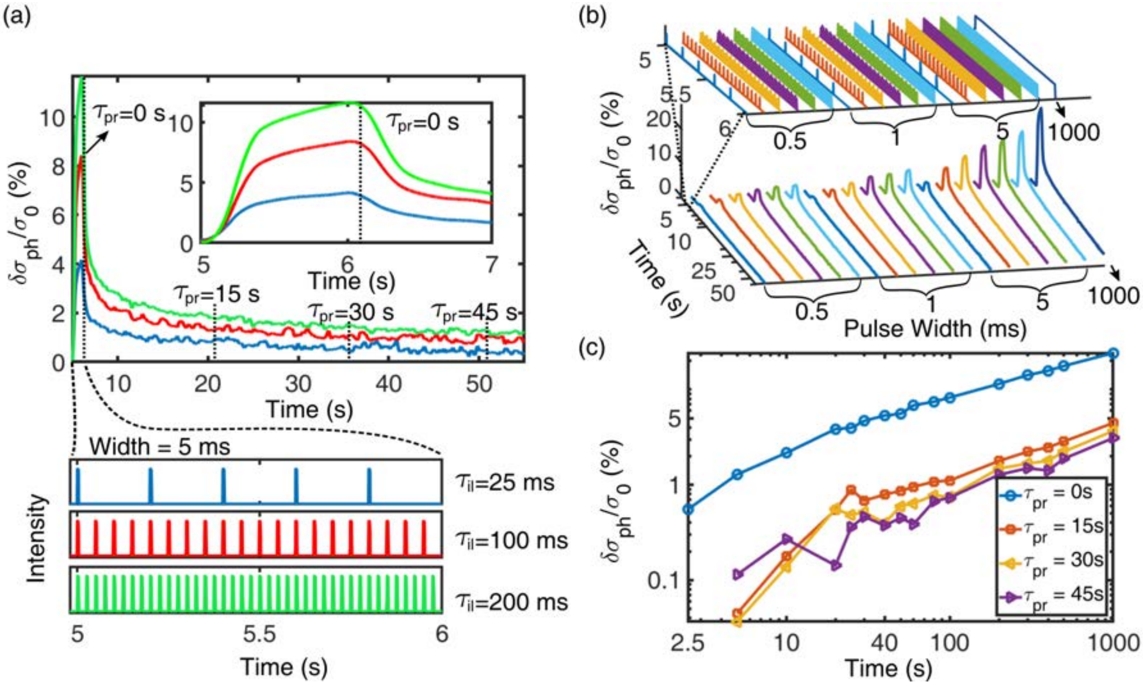

FIGURE 5.3: (a) Photoconductive response of the amorphous $LaAlO_3/SrTiO_3$ interface under illumination time $\tau il = 25 - 200\,ms$ with violet light ($\lambda = 405\,nm$) and irradiance $P_w \approx 10^3\,W \cdot nm^{-1} \cdot m^{-2}$. The lower graph displays the detected intensity (arbitrary units) of light reflected from the sample during the illumination with the light pulses. The illumination time is defined by $\tau_{il} = N_p \times W_p$, where N_p is the number of pulses, and W_p is the width of every individual pulse ($Wp \approx 5\,ms$ in the data shown in this panel). The figure also indicates different probe times τ_{pr} where the photoconductance is measured, which are used in data presented in panel (c). (b) The upper panel displays the detected intensity of light reflected from the sample after illumination with pulse trains defined by $Np = 5 - 100$ and $W_p \approx 0.5 - 5\,ms$, resulting in illumination times spanning the interval $\tau_{il} = 2.5 - 1000\,ms$. The lower graph displays the time evolution of photoconductance corresponding to the response to every particular pulse train. (c) Photoconductance measured at different probe times ($\tau_{pr} = 0, 15, 30,$ and $45\,s$) as a function of the illumination time.

Now we address the potential for neuromorphic applications, which requires a functional response that emulates the plasticity of biological synapses [150]. To analyze this aspect, we measured $\frac{\delta\sigma_{ph}(\tau_{il})}{\sigma_0}$ after impinging the samples with trains of light pulses of irradiance $P_w \approx (150 - 1000)\,W \cdot nm^{-1} \cdot m^{-2}$, defined by the number of pulses ($N_p = 1 - 10$) and the width of every single pulse $W_p \approx 0.5, 1, 5\,ms$ (Figure 5.3b). In this case, the illumination time is defined as the cumulated time resulting from all light pulses, i.e., $\tau_{il} = N_p \times W_p$. Since we need to quantify the plasticity of the PPC response, we define an additional parameter, the probe time τ_{pr} at which

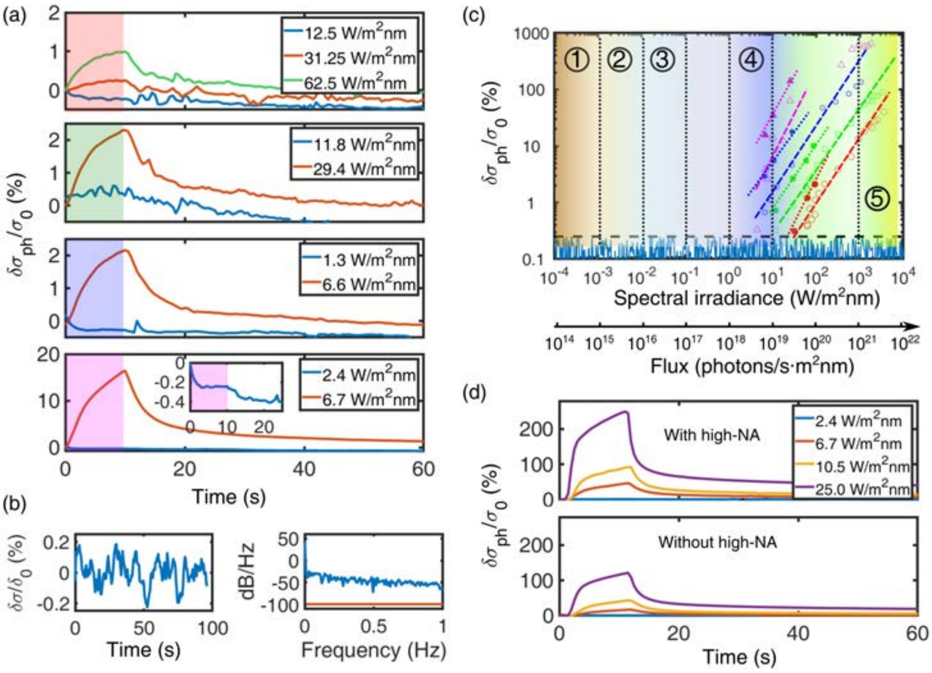

FIGURE 5.4: (a) Photoconductance measured under low irradiance ($P_w < 10^2\ W \cdot nm^{-1} \cdot m^{-2}$) at different wavelengths (from top to bottom: red, green, blue, violet) and illumination time $\tau_{il} = 10\,s$. (b) Left: Conductance measured in darkness over an interval of a few tens of seconds, displaying random noise, where refers to deviations of conductance with respect to the average 0. Right: Power spectral density (PSD) of the measured noise calculated from eq 5.2 and spectral density of thermal noise calculated from eq 5.1 are shown as the blue and red lines, respectively. (c) Photoconductance measured after illumination time $\tau_{il} = 1500\,ms$ (probe time $\tau_{pr} = 1500\,ms$) as a function of the photon arrival rate calculated for green light. Numbers in this Figure denote regimes of photon arrival rates for different environmental conditions: (1) light from sky in a dull day ($A_r \approx 10^{15} photons/s/m^2/nm$); (2) natural scenes $A_r \approx 10^{15} - 10^{16} photons/s/m^2/nm$); (3) brightness of computer monitors ($A_r \approx 10^{16} - 10^{17} photons/s/m^2/nm$); (4) bright mid-day sun on land ($A_r \approx 10^{18} - 10^{19} photons/s/m^2/nm$); (5) damage to the eye ($A_r \geq 10^{21} photons/s/m^2/nm$). These estimations are extracted from the literature [150, 169]. For illustrative purposes, the random noise shown at the bottom of the Figure was generated by the MATLAB function *rand()* with the same amplitude as the one obtained from experiments. (d) Photoconductance measured under direct illumination with different irradiance values (upper graph) or under high-numerical-aperture focusing (lower graph).

the photoconductance $\frac{\delta\sigma_{ph}(\tau_{il})}{\sigma_0}$ is measured after switching the light off. Both the illumination (τ_{il}) and probe (τ_{pr}) times are defined in Figure 5.3a, which displays data from measurements of the photoconductance in response to selected pulse trains. The latter are visualized in the lower panel as the intensity detected from light reflected off the surface, while the main panel of Figure 5.3a displays the photoconductance measured after photoexcitation. From this Figure we clearly see that: (i) after photoexcitation with short pulses ($\tau_{il} < 200\,ms$) the conductance is not recovered to the initial state over periods extending several tens of seconds, and (ii) the value of the persistent conductance measured at different probe times ($\tau_{pr} < 70\,s$ in Figure 5.3a) increases with the illumination time τ_{il}, hinting at the plastic character of the photoconductive response.

To have a complete picture of the plastic response, we extended these results to all wavelengths and a wide range of illumination times. Accounting for the number of pulses and their individual width, the ensemble of our measurements covered cumulated illumination times that spanned over almost three orders of magnitude ($\tau_{il} \approx 2.5 - 1000\, ms$). The results of this extensive study are summarized in Figure 5.3c, which plots the values of the photoconductance $\frac{\delta\sigma_{ph}(\tau_{il})}{\sigma_0}$ measured at different probe times ($\tau_{pr} = 0$ s, i.e., immediately after switching the light off and at $\tau_{pr} = 15$, 30 and 45 s). The outcome of this study reveals that the photoconductance $\frac{\delta\sigma_{ph}(\tau_{il})}{\sigma_0}$ can be modulated over two decades for the cumulated illumination timespan $\tau_{il} \approx 2.5 - 1000\, ms$ (Figure 5.3c). Therefore, the data shown in Figure 5.3 demonstrates that the cumulated illumination time in pulse trains can be used to fine-tune the plastic PPC response in the a-$LaAlO_3/SrTiO_3$ system.

Now, can this fine-tunability be used under conditions approaching ambient illumination environments? To gauge this possibility, we have to tackle the responsiveness of the system to illumination conditions that imply low enough irradiance ($P_w \ll 10^2\, W \cdot nm^{-1} \cdot m^{-2}$, see Figure 5.4c). In this context it is relevant to quantify the noise level and estimate the sensitivity threshold for a detectable change in conductance. For that purpose, we measured the photoconductive signal after photoexcitation with irradiance $P_w < 10^2\, W \cdot nm^{-1} \cdot m^{-2}$ and illumination time $\tau_{il} = 1500\, ms$ see Figure 5.4a for data acquired in a sample about 10^6 s after its growth, when its resistance was $R \approx 8 \times 10^5\, \Omega$(see Figure 2a). The results show that the photoconductance is larger at short wavelengths, i.e., $\frac{\delta\sigma_{ph}(\tau_{il})}{\sigma_0} > 15\%$ at $\lambda = 405\, nm$, while $\frac{\delta\sigma_{ph}(\tau_{il})}{\sigma_0} \approx 1\%$ at $\lambda = 638\, nm$, see Figure 5.4a. It is also observed that the photoconductance is not increasing linearly with irradiance, and it appears to show a sudden increase at a threshold value that for blue-violet light is $P_w \lesssim 6W \cdot nm^{-1} \cdot m^{-2}$ (Figure 5.4a). To evaluate the noise amplitude, we measured the conductance in darkness for periods of several tens of seconds (Figure 5.4b). We see that the random fluctuations in conductance give rise to noise amplitude $\frac{\delta\sigma_{ph}(\tau_{il})}{\sigma_0} \approx 4\%$, as calculated from the root mean square value over the analyzed time interval. This value has to be compared with the amplitude of the photoconductance $\frac{\delta\sigma_{ph}(\tau_{il})}{\sigma_0} \approx (0.4 - 900)\%$ under illumination time $\tau_{il} = 1500\, ms$ for a sample of aging time $2 \times 10^7\, s$ (Figure 5.4c).

We compared the observed noise amplitude with the noise due to thermal motion of electrons in conducting media. The spectral density of thermal noise is given by [171]

$$G_v(f) = \frac{2Rh|f|}{exp(h|f|/k_BT) - 1} \approx 2Rk_BT \tag{5.1}$$

where f is the frequency, R the resistance, T the temperature and h and k_B are the Planck and Boltzmann constants, respectively. The right hand of Equation 5.1 is valid for frequencies$|f| \ll \frac{k_BT}{h}$, which is fulfilled at room temperature up to $f \approx 10^{12} Hz$, well above the bandwidth of conventional electrical instrumentation. The spectral density $p_{rnd}(f)$ was calculated via discrete-time Fourier transform as

$$p_{rnd}(f) = \frac{1}{Lf_s} \left| \sum_{n=0}^{L-1} v_L(n) e^{-j2\pi nf/f_s} \right|^2 \tag{5.2}$$

for a signal $v_L(n)$, corresponding to a finite number of L voltage readings and f_s is the sampling frequency ($f_s = 2\,Hz$ in our measurements). The spectral density calculated from Equation 5.2 is displayed in Figure 5.4b, yielding a value $p_{rnd}(f) \approx -45\,dB/Hz$. The spectral density of thermal noise associated with the resistance $R \approx 8 \times 10^8\,\Omega$ calculated from Equation 5.1 is $G_v \approx -99\,dB/Hz$, see Figure 5.4b. Therefore, for the highest resistance state which, as discussed above, has the largest sensitivity to photoconductance the spectral density of the random signals measured with the used instrumentation (described in Supporting information Section 5.6.1) is considerably larger than the intrinsic thermal noise of the device resistance (Figure 5.4b, right panel). This is an important observation towards optimizing the signal-to-noise ratio. Indeed, we show that the use of lock-in amplifiers for voltage detection -using phase-sensitive detection to single out signals at specific frequencies results in noise amplitude much closer to the theoretical estimation for thermal noise (see Supporting information Section 5.6.1).

We address now the sensitivity of photoconductance to different illumination conditions. The discussion is focused on data extracted from experiments carried out with resistance $R \approx 810^8\,\Omega$ after photoexcitation with illumination time $\tau_{il} = 1500\,ms$ and varying illuminance conditions spanning a broad range $P_w \approx 2.5 - 15000\,W \cdot nm^{-1} \cdot m^{-2}$. This range of illuminance can be translated into a range of photon arrival rates A_r that, for the case of green light ($\lambda = 520\,nm$), is equivalent to $A_r \approx 6.6 \times 10^{18} - 3.95 \times 10^{22}\,photons/s/m^2/nm$. To put these values in context, we note that photon arrival times in the visible can be estimated for different habitat illuminance conditions from references in the literature, such as light from sky in a bright midday sun on land ($A_r \approx 10^{18} - 10^{19}\,photons/s/m^2/nm$), brightness of a computer monitor ($A_r \approx 10^{16} - 10^{17}\,photons/s/m^2/nm$), brightness from natural scenes ($A_r \approx 10^{15} - 10^{16}\,photons/s/m^2/nm$), light from sky in a dull-day ($A_r \approx 10^{15}\,photons/s/m^2/nm$) or mid-dusk on land ($A_r \approx 10^{13} - 10^{14}\,photons/s/m^2/nm$), while the damage to the eye happens above $A_r \approx 10^{21}\,photons/s/m^2/nm$ [150, 169]. These different illumination environments are indicated across the range of arrival photon rates shown in Figure 5.4c.

To evaluate the responsiveness of the photoconductance of the a-$LaAlO_3/SrTiO_3$ interface to a diversity of environmental conditions, the values of $\frac{\delta\sigma_{ph}(\tau_{il})}{\sigma_0}$ were measured at different wavelengths under illumination time $\tau_{il} = 1500\,ms$ (Figure 5.4c). The data reported in this Figure was acquired immediately after switching off light ($\tau_{pr} = 0\,s$). Empty symbols correspond to direct illumination, while solid symbols represent the data acquired under focusing conditions. For the latter, the value of the illuminance is determined at the back aperture of the objective lens. The data displayed in Figure 5.4c shows that high-NA focusing increases substantially the sensitivity to varying illumination conditions (Figure 5.4d). This is not unexpected since the strong reduction of the spot size is overcompensated by the strong increase of photon flux over the reduced illuminated area, resulting in larger changes of conductance. We also observe that the photoconductive response is highly nonlinear with wavelength, with values that go from $\frac{\delta\sigma_{ph}(\tau_{il})}{\sigma_0} \approx (0.3 - 30)\%$ for red to $\frac{\delta\sigma_{ph}(\tau_{il})}{\sigma_0} \approx (3 - 900)\%$ for violet. Interestingly, the data displayed in the low irradiance region demonstrate that the photoconductance of the amorphous $LaAlO_3/SrTiO_3$ system is sensitive to changes in brightness comparable to bright day conditions ($A_r \approx 10^{18} - 10^{19}\ photons/s/m^2/nm$). Attempts to measure the photoconductance for lower rates, i.e., $A_r < 10^{18}\ photons/s/m^2/nm$, give values that are too low to be detected above the noise level (Figure 5.4c). This is partly accounted for by the sheer drop of photoconductance that occurs for irradiance below $P_w < 6\, W \cdot nm^{-1} \cdot m^{-2}$, especially noticeable for blue and violet, which limits the sensitivity at the low end of irradiance. Further studies are needed to understand this observation.

5.5 Conclusion

Summing up, our research gives a perspective on the use of persistent photoconductance of the amorphous $LaAlO_3/SrTiO_3$ interface for neuromorphic vision applications through the detection of ambient conditions potentially found in natural scenes. As a general rule, we find that highly-resistive states are desirable for optimal sensitivity. This, in turn, may require finding appropriate conditions for materials preparation, especially regarding the stability of the transport properties and oxygen stoichiometry, which is discussed in this Chapter. Also, our study reveals that sensitivity to visual contrasts in bright day conditions is feasible with a-$LaAlO_3/SrTiO_3$, albeit the sensitivity required for scenes under more demanding conditions, such as dull-day or dusk ambient light, is far more challenging and calls for other approaches to increase the responsiveness. This sensitivity threshold is certainly a limitation for applications demanding dynamical sensing of visual scenes, but it could afford an alternative for image acquisition and recognition of visual patterns of large enough intensity. Another relevant interesting aspect is that measurements of photoconductance carried out at the lowest irradiance conditions were done after relatively long illumination times ($\tau_{il} = 1500\, ms$), roughly one order of magnitude above the timescales typical for perceptual cognition (on the scale of $100's$ of ms) [150], One possible way to improve the performance may be with the help of plasmonics. Indeed, the same principles that enable plasmonics to improve absorption in photovoltaic devices and solar cells [172], or to boost surface-enhanced Raman spectroscopy [173],may serve well the purpose to increase the photoconductance sensitivity to lower photon arrival rates. Further studies are required to explore this possibility.

5.6 Supporting information

5.6.1 Measurement noise and thermal noise

During the measurement of the electronic transport, the voltage is measured with a lock-in amplifier (Ametek model 7270 ®) with sampling frequency $2\, kHz$ and injected dc currents of $\approx 1\, A$ for devices with resistance $R \leq 10^6\, \Omega$. Alternatively, the voltage across samples with higher resistance is measured with a Keithley 2611B instrument with sampling frequency $2\, Hz$ and dc

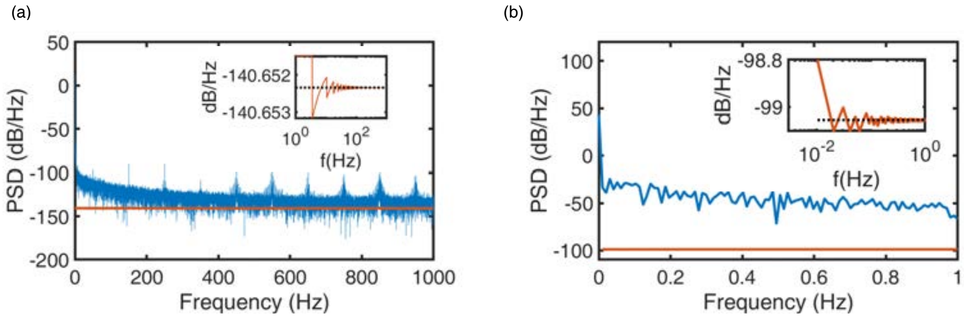

FIGURE 5.5: The power spectral density (PSD, blue line) and spectral density of thermal noise $G_v(f)$ (red line) from lock-in amplifier (a) and Keithley 2611B (b). The zooms in both panels show the $G_v(f)$.

current of $\approx 1\,nA$. We measured random signals by recording the conductance in darkness for given periods of time. The corresponding power spectral densities (PSD) were calculated from Equation 5.2 of the main text, which are shown in Figure 5.5 for measurements done with the lock-in amplifier Ametek model 7270 panel (a) and Keithley 2611B panel (b). The data measured for the lock-in amplifier gives an average value $PSD \approx -132.23\,dB$ at frequencies $> 200\,Hz$ (note that the sampling frequency is $2\,kHz$), which is relatively close to the theoretical value of thermal noise PSD -140.65 dB calculated from Equation 1 for $R \leq 10^6\,\Omega$ (Figure 5.5a).

5.6.2 Dependence of the resistance and photoconductance on growth conditions

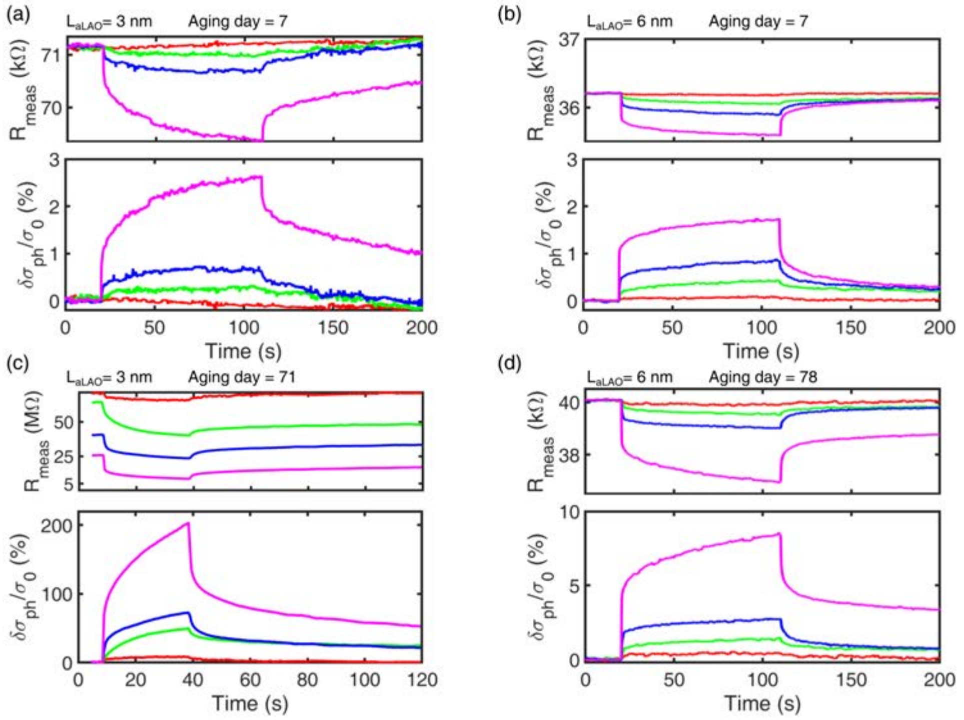

FIGURE 5.6: Normalized photoconductance and resistance of two a-$LaAlO_3/SrTiO_3$ samples grown under identical conditions with thickness 3 (panels (a) and (c)) and 6nm (panels (b) and (d)), respectively. The data were measured at different aging times, as indicated in the figures..

The transport properties of the amorphous $LaAlO_3/SrTiO_3$ interfaces depend on the growth parameters. We illustrate this observation by plotting the evolution of the transport properties and photoconductance as a function of the thickness of the deposited $LaAlO_3$ film, keeping the deposition pressure fixed. In previous works, we have demonstrated that the vacancy concentration in $LaAlO_3/SrTiO_3$ can be controllably tuned by changing the thickness of oxide films [80]. The same trend is observed for many amorphous films grown on $SrTiO_3$ crystals [158]. Therefore, the amount of oxygen vacancies (and, therefore, of carriers) can be modulated by changing the thickness, whereby larger concentrations of vacancies are attained in samples with thicker deposited overlayers. We consider now the samples that were analysed in the present study. In Figure 5.6 we compare the resistance and photoconductance of two amorphous $LaAlO_3/SrTiO_3$ interfaces grown under identical conditions but with different thickness of the $LaAlO_3$ layer, namely, 3 and 6 nm, respectively. As we see in Figure 5.6, in agreement with the above-mentioned reports, increasing the thickness of the amorphous $LaAlO_3$ layer causes a decrease of the resistance and, correspondingly, the relative change of photoconductance is larger for the thinner film. This observation provides a strategy to achieve the highest possible resistance state, based on decreasing the thickness as closer as possible to the critical value needed for the conductive interface.

Chapter 6

Outlook and Perspectives

In this thesis, we have analyzed the wavelength-dependent time-correlated photoresponses of the epitaxial $LaAlO_3/SrTiO_3$ interface (Chapter 3), which can be extended to neuromorphic photonics based on spiking time-dependent plasticity model (Chapter 4). Furthermore, we have explored the sensitivity of the photoconductance of amorphous $LaAlO_3/SrTiO_3$ interfaces to environmental illumination conditions (Chapter 5). This chapter provides perspectives and outlook on potential applications of the studied photoresponses to neuron networks consisting of $LaAlO_3/SrTiO_3$ interfaces as synapses and physical mechanisms of the interplay between the 2DES and other functional oxides , e.g., ferroelectric oxides.

While we are watching around this moment, a remarkable and sophisticated show is playing in our brains. Is it possible to emulate the complicated and fast biological vision system? Lets see how can we see and how can electronics emulate basic features of vision.

6.1 Artificial synapses and neurons for vision

Biological vision is a sophisticated process of image formation performed by several varieties of neuronal cells. A beam of photons coming out of an object enters the eye and is absorbed by the *photoreceptors*, by which the photons are converted into electric current via a phototransduction process. The information contained in such input signals is redundant and some reduction is required before proceeding towards the brain. For this purpose, the retina performs low-level information processing as follows , see also Figure 6.1: before the signal flows into the bipolar cells, the horizontal cells modulate it, so that, instead of absolute levels of light, the information is coded by the difference in the values between the received light and the surrounding light detected by the photoreceptors. This involves signal subtraction from the surrounding cells and, therefore, the global signal processing in the retina requires both excitatory and inhibitory synapses. Subsequently, the modulated signal travels through the ganglion cells and is modulated further by amacrine cells using a similar protocol, so that the surrounding excitation is subtracted from the central excitation of illumination for bipolar cell inputs [107, 174]. In the following, photoreceptor and ganglion cells are described briefly, as well as their implementation of artifical vision using the persistent photoconductance observed in the 2DES at the $LaAlO_3/SrTiO_3$ interface.

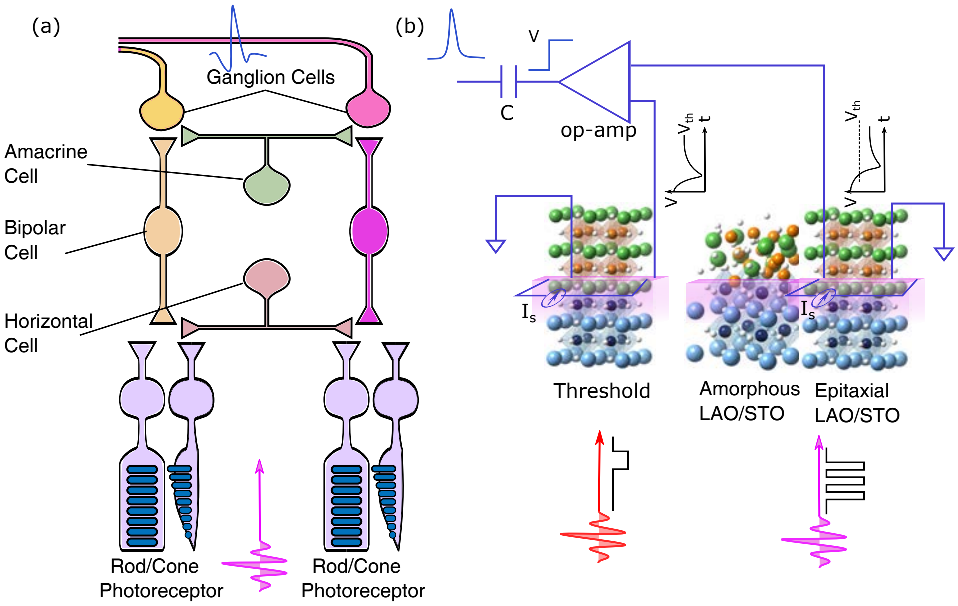

FIGURE 6.1: (a) schematic diagram showing retinal information processing. Information carried by light reaches the photoreceptors and flows to bipolar cells and then ganglion cells which are connected to the optic nerve. During the information flowing, horizontal cells and amacrine cells adjust the actions of bipolar cells and ganglion cells. (b) Proposed artificial retina based on the photoconductance of $LaAlO_3/SrTiO_3$. An $LaAlO_3/SrTiO_3$ system may be used to adjust the threshold value on one of the inputs to an operational amplifier. Conversely, other $LaAlO_3/SrTiO_3$ systems are coupled to the other input of the operational amplifier and produce an output spike whenever the photoresponse crosses the thershold.

6.1.1 Photoreceptor and ganglion cells

There are two main types of photoreceptors in the retina, namely, rods and cones, which both contain disk membranes where photopigments absorb light, resulting in changes of the membrane potential that lead to conversion from light to electric signals. Only rods play a major role in detecting the shape and movement in very dim light. That is because there is a large number of rods (about 92 million rods and 5 million cones in the human retina [107]) and inside of them there are much more disks and much higher concentration of photopigments, which make them more sensitive to the light intensity (but not wavelength). On the other hand, cones contribute to vision in photopic conditions, i.e., well-lit environments with large enough luminance levels, and also are responsible for discriminating colors. The reason of the color perception is that the bright light can activate the three kinds of cones which are sensitive to red, green and blue light, respectively, and then the brain deduces the signal of wavelength-dependence to reproduce the colorful picture.

The photoreceptor is a key element in the design of a non-biological vision system that aims at replicating the basic features of a biological retina. In this respect, it is important to replicate the synaptic plasticity found in biological systems which, as mentioned above, has to include both excitatory and inhibitory synapses. In excitatory synapses, the external stimuli (light in our case) increase the synaptic weight, so that the likelihood to trigger a neuron spike increases.

Conversely, the synaptic strength is decreased in inhibitory synapses, thus decreasing the likelihood for neuron firing. As described in previous chapters, the photoconductance of the epitaxial $LaAlO_3/SrTiO_3$ interface can be increased or decreased depending on the frequency and the time arrival of optical pulses, endowing these systems with the capability to replicate excitatory and inhibitory synapses.

Furthermore, synaptic plasticity in biological vision is relevant to ganglion cells, which are a type of spiking neuron cells that project axons through the optic nerves, which can be considered as ports where the information is transmitted to the brain in the form of action potentials. We discuss in the next section how an artificical spiking neuron can be built from the photoresponse of the $LaAlO_3/SrTiO_3$ interface.

6.1.2 Electric vision

Retina forms images through transmitting in spikes carried the encoded information by relative changes. This property allows encoding information from an external image only when an event causes a change in the light intensity, e.g., caused by a movement of an object, saving a huge amount of redundant information. In contrast, a common camera captures images at periodic framed times, recording the whole ensemble of infomation at every clock time. The redundant information recorded and transmitted consumes much energy, time and memory. As aformentioned, the neuromorphic retina can save a lot of time and energy by capturing images by refreshing pixel by pixel only when a change of light intensity is produced, which is at the basis of the so-called event-based vision sensors. Along these lines, Carver Mead and his colleagues proposed 1990s, to build a silicon retina with asynchronous digital output [40]. They modeled the silicon retina through combining silicon photoreceptors and designing adaptive circuitry to calculate the changing light level [175].

Our observations that the wavelength-dependent time-correlated photoresponses at the epitaxial $LaAlO_3/SrTiO_3$ interface (Chapters 3 , 4) and the profound sensitivity at the amorphous $LaAlO_3/SrTiO_3$ interface (Chapter 5), potentially provide an alternate approach to implement the artificial retina. As illustrated in Figure 6.1b, the $LaAlO_3/SrTiO_3$ systems, acting as synapses, can be integrated in a circuitry, which can be designed to act as artificial neurons that can generate spikes in responses to changes of the photoresponse. In Figure 6.1b, a group of $LaAlO_3/SrTiO_3$ systems are used to set the firing thresholds V_{th} of the artificial spiking neurons, whose value can be adjusted by light (6.1b left). Another group of $LaAlO_3/SrTiO_3$ systems respond to the optic pulses, causing to decrease in the voltage. Once the decreasing voltage reaches the threshold V_{th}, the operational-amplifier produces a sudden change of output voltage. In this model, both the synaptic threshold and synaptic plasticity are suggested to be replicated by $LaAlO_3/SrTiO_3$ systems, which may mimic the computation of the light difference through Horizontal cell and Amacrine cells of biological vision (see above). This implementation would be a step beyond this Thesis, which would represent replicating physically a spiking neuron from the photoresponse of the $LaAlO_3/SrTiO_3$ interface.

6.2 Complex oxide device based on 2DES

Here we discuss another perspective beyond the work presented in this Thesis, which aims at taking advantage of the large variety of physical properties of transition metal complex oxides, which arise from the narrow bandwidths dominated by d-orbitals where strongly correlated electrons intrinsically compete or cooperate in the charge, spin and orbital degrees of freedom [176]. Such interaction induces kinds of symmetry breaking, resulting in a variety of astounding properties, such as superconductivity, multiferroics, Mott insulators and metal-insulator transitions [177]. Due to their structural compability, these complex oxides can combine with the 2DES at the $LaAlO_3/SrTiO_3$ interface, offering multiple functionality that can be useful for neuromorphic devices.

For instance, as we discussed in Chapter 3, the properties of the 2DES can be modified by electronic states at the $LaAlO_3$ surface. This can be also achieved by using some functional oxides that can be epitaxially grown on the surface of $LaAlO_3/SrTiO_3$, such as ferroelectrics [178, 179]. This would enable the ferroelectric polarization to modulate the charge of surface states. One the other hand, capping the $LaAlO_3$ surface with metals can also modify the properties of 2DES, providing additional routes to modulate the conductance externally [180].

Appendix A

Optical lithography protocols

Micro-Writer ML3 from Durham Magneto Optics Ltd. (DMO) is used to directly write the patterns onto the photoresist (PR), which is polydimethylglutarimide (PGMI) Shipley S1813 during current study. The software CleWin4 is recommended to design the patterns.

- Rinsing the substrate with acetone and isopropanol. Then blowing with Nitrogen gun
- Dehydration bake to remove water 95°C
- Spin coating of S1813, with 5500 rpm and acceleration of 0.7 s
- Soft baking at 95°C for $60 - 90\,s$
- Exposure with 385 nm lightsource (i-line) with fluency around 200 mJ/cm
- Develop for 60 s
- Deposition
- Liftoff of S1813 through immersing in the acetone

Appendix B

Photoconductance Calculation Details

B.1 Photoexcitation via DX-resonance states

The in-scattering $\Sigma_{in}(\vec{x},t)$ and out-scattering $\Sigma_{out}(\vec{x},t)$ functions described in this chapter give account, respectively, of the inward and outward flux of particles in the quantum well. For the function $\Sigma_{in}(\vec{x},t)$ we assume that it is proportional to the differential scattering cross-section of the optical absorption process, which is proportional to the current-current operator, i.e.,

$$\frac{d^2\sigma}{d\Omega d\omega} \sim \langle Tj(\vec{x},t)j(0)\rangle \tag{B.1}$$

We solve the current-current autocorrelation function $\langle Tj(\vec{x},t)j(0)\rangle$ using finite-temperature Green's functions following the procedure described in chapter 4 Ref [128]. We assume that the current operator is given by

$$j(\vec{x},t) = P\sum_{c,c'} b_c^+ b_{c'} \tag{B.2}$$

where, for simplicity, we consider the matrix element P constant. In Equation B.2, the operators $(b_c^+ b_{c'})$ refer to DX-center states. Then, we compute Equation B.1 using finite-temperature Green's functions:

$$\begin{gathered}\langle Tj(\vec{x},t)j(0)\rangle = P\textstyle\sum_{c_2,c_1',c_1,c_1'} \left\langle Tb_{c_2}^+(t)b_{c_2'}(t)b_{c_1}^+ b_{c_1'}\right\rangle = \\ Pe^{\beta\Omega}\textstyle\sum_{c_2,c_2',c_1,c_1'} \mathrm{Tr}\left\{e^{-\beta H_1}e^{iH_1t}b_{c_2}^+ b_{c_2'}e^{-iH_1t}b_{c_1}^+ b_{c_1'}\right\}\end{gathered} \tag{B.3}$$

where H_1 is the Hamiltonian described in Equation 3.1 , $\beta = 1/k_BT$ (defined in terms of the temperature T and Boltzmann constant k_B), *Tr* is the trace over the complete set of states and Ω is defined as $e^{-\beta\Omega} = e^{-\beta[H_1-\mu N]}$, with μ the chemical potential and N the number operator. The canonical transformation $S = \sum_c b_c^+ b_c \sum q\frac{M_q}{\omega_q}\left[a_q + a_q^+\right]$ changes the Hamiltonian to $\overline{H_1} = e^S H_1 e^S$ (Equation 3.1). Then, Equation B.3 can be rewritten as

$$\begin{aligned}\langle Tj(\vec{x},t)j(0)\rangle &= Pe^{\beta\Omega}\textstyle\sum_{c_2,c_2',c_1,c_1'} \mathrm{Tr}\left\{e^{-\beta\widetilde{H}_1}e^{i\widetilde{H}_1t}X_{c_2}^+X_{c_2}'b_{c_2}^+b_{c_2'}e^{-i\widetilde{H}_1'}X_{c_1}^+X_{c_1}^+b_{c_1}^+b_{c_1'}b_{c_1'}\right\} \\ &= Pe^{\beta\Omega}\textstyle\sum_{c_2,c_2',c_1,c_1'} e^{it\left(\varepsilon_{c_2}-\varepsilon_{c_2'}-\Delta\right)}\,\mathrm{Tr}\left\{e^{-\beta\widetilde{H_1}}X_{c_2}^+(t)X_{c_2'}(t)X_{c_1}^+X_{c_1'}b_{c_2}'b_{c_2'}b_{c_1}^+b_{c_1'}\right\} \\ &= Pe^{\beta\Omega}\textstyle\sum_{c_2,c_2',c_1,c_1'} e^{it\left(\varepsilon_{c_2}-\varepsilon_{c_2'}-\Delta\right)}\,\mathrm{Tr}\left\{e^{-\beta\widetilde{H}_1}b_{c_2}^+b_{c_2'}b_{c_1}^+b_{c_1'}\right\}\mathrm{Tr}\left\{e^{-\beta\widetilde{H}_1}X_{c_2}^+(t)X_{c_2'}(t)X_{c_1}^+X_{c_1'}\right\}\end{aligned} \tag{B.4}$$

where $X_{c_i} = exp\left[-\sum_q \frac{M_q}{\omega_q}[a_q^+ - a_q]\right]$, with M_q the dimensionless electron-phonon coupling parameter, (a_q, a_q^+) the annihilation and creation operators for phonons and $\Delta = \sum_q \frac{M_q}{\omega_q}$. In Equation B.4, the electronic part of the trace can be calculated as:

$$\mathrm{Tr}\left\{e^{-\beta\widetilde{H}_1} b_{c_2}^+ b_{c_2'} b_{c_1'} b_{c_1'}\right\} = \mathrm{Tr}\left\{e^{-\beta\widetilde{H}_1} b_{c_2}^+ b_{c_1} b_{c_1}^+ b_{c_2}\right\} = \left(1 - n_{DX}^*\left(\varepsilon_{DX}^*\right)\right) n_{DX}\left(\varepsilon_{DX}\right) \tag{B.5}$$

In Equation B.5 we make use of Wick's theorem, so that the subscripts in the operators $(b_{c_i}, b_{c_i}^+)$ must be paired up, and thus, $c_2' = c_1$ and$c_1' = c_2$. The terms $n_D X$ ($_D X$) and $n_D X^*$ ($_D X^*$) refer, to the density of states of DX centers in the ground and excited state, respectively.

The phonon part of the trace in Equation B.4 can be evaluated following the procedure described in chapter 4 of Reference [128], so that

$$\mathrm{Tr}\left\{e^{-\beta\widetilde{H}_1} X_{c_2}^+(t) X_{c_2'}(t) X_{c_1}^+ X_{c_1'}\right\} = \exp\left[-\frac{M_{q_0}}{\omega_0}\left[(N_0+1)\left(1-e^{-i\omega_0 t}\right) N_0\left(1-e^{+i\omega_0 t}\right)\right]\right] \tag{B.6}$$

where we consider an Einstein model for phonons with $\omega_q = \omega_0$, and N_0 is the phonon occupation number.

We end up with the following expression for the optical absorption process,

$$\frac{d^2\sigma}{d\Omega d\omega} \propto \frac{P}{2\omega}\left[\int\int \delta\left\{\hbar\omega - \left(\varepsilon_{DX}^* - \varepsilon_{DX}\right)\right\}\left(1 - n_{DX}^*\left(\varepsilon_{DX}^*\right)\right) n_{DX}\left(\varepsilon_{DX}\right) d\varepsilon_{DX} d\varepsilon_{DX}^*\right]$$
$$\int_{-\infty}^{+\infty} dt \exp\left\{it\left[\left[\left(\omega + \varepsilon_{DX}^* - \varepsilon_{DX} - \Delta\right)\right] - \frac{M_{q_0}}{\omega_0}\left[(N_0+1)\left(1-e^{-i\omega_0 t}\right) N_0\left(1-e^{+i\omega_0 t}\right)\right]\right]\right\} \tag{B.7}$$

An expansion can be used to simplify Equation B.7 using Bessel functions of the first kind and complex argument, so that finally the expression can be rewritten as

$$\begin{gathered}\tfrac{d^2\sigma}{d\Omega d\omega} \propto \tfrac{P}{2\omega}\left[\iint \delta\left\{\hbar\omega - \left(\varepsilon_{DX}^* - \varepsilon_{DX}\right)\right\}\left(1 - n_{DX}^*\left(\varepsilon_{DX}^*\right)\right) n_{DX}\left(\varepsilon_{DX}\right) d\varepsilon_{DX} d\varepsilon_{DX}^*\right] \\ e^{-g\left(2N_q+1\right)} \sum_m \delta\left\{\hbar\left(\omega - \omega_m\right) I_m(\gamma)\right\} e^{m\hbar\omega_0/2k_B T}\end{gathered} \tag{B.8}$$

which is Equation 3.4. The expression includes the Bessel function $I_m(\gamma)$, where $\gamma = 2g\sqrt{N_0(N_0+1)}$, g is the electron-phonon coupling and m is the number of phonons has to be emitted so that $\hbar w_m = \varepsilon_{DX}^* - \varepsilon_{DX} - (g - m)\hbar\omega_0$.

B.2 Calculation of the density of states (DOS)

B.2.1 Quantum well states

I. DOS for π bands of bulk SrTiO$_3$

Due to the symmetry of the wavefunction, the overlaps of $O - 2p$ orbitals and $Ti - 3d$ orbitals only permit two types of bands: t_{2g} orbitals and p orbitals form π bands, or e_g orbitals and p orbitals form σ bands. For the t_{2g} states coming from π-type bonds, the following dispersion relation (Ref. [181]) is used

$$E_{\vec{k}\pi(\alpha\beta)} = \frac{1}{2}\left(E_t + E_\perp\right) + \sqrt{\left[\frac{1}{2}\left(E_t - E_\perp\right)\right]^2 + 4(pd\pi)^2\left(S_\alpha^2 + S_\beta^2\right)} \\ (\alpha\beta = xy, xz, \text{ or } yz) \tag{B.9}$$

and the density of states is given by the expression (Ref. [181]).

$$\rho_\pi(E) = \frac{1}{\pi^2}\left|\frac{E - \frac{1}{2}\left(E_t + E_\perp\right)}{(pd\pi)^2}\right| K\left(\sqrt{1-\left(\varepsilon_\pi(E)/2\right)^2}\right)\Theta\left[1-\left(\varepsilon_\pi(E)/2\right)^2\right] \tag{B.10}$$

where $K(k) = \int_0^{\pi/2}\frac{d\theta}{\sqrt{1-k^2\sin^2\theta}}$ is the complete elliptical integral of the first kind and $\Theta[x]$ is the Heaviside function. $\varepsilon_\pi(E) \equiv \frac{\left[E_{\vec{k}v} - \frac{1}{2}(E_t+E_\perp)\right]^2 - \left[\frac{1}{2}(E_t-E_\perp)\right]^2}{2(pd\pi)^2} - 2$ is deduced from the Equation B.9, and $S_\alpha \equiv \sin k_\alpha a$. That the DOS of the π band bulk $SrTiO_3$ can be calculated, as shown in Figure B.1 The initiate values are chosen from the literature (Ref. [182]) and adjusted according to the density functional theory calculation (Ref. [183]), as shown in Figure B.1b. Therefore the parameters are obtained as: $E_t = 0$, $pd = 1.29\,eV$, $E_\perp = -3.36\,eV$, which gives the Energy gap. The lattice constant a is set as 1.

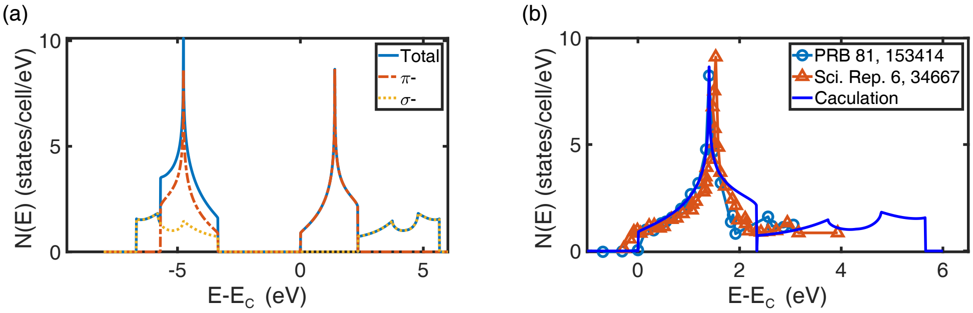

FIGURE B.1: (a) The total density of states (DOS) of the π band and σ band in bulk $SrTiO_3$. The energy gap between conduction band and valance band is $\Delta E = 3.36\,eV$. (b) Comparison of conduction band DOS between the analytical calculation and DFT calculations [183, 184].

II. DOS for σ bands of bulk $SrTiO_3$

For the e_g states coming from σ-type bonds, we considered these expressions (Ref. [181])

$$\rho\left(\varepsilon_\sigma\right) = \begin{cases} \rho_1\left(\varepsilon_\sigma\right) & \text{for } \left|\varepsilon_\sigma\right| \leq 1 \\ \rho_2\left(\varepsilon_\sigma\right) & \text{for } 1 \leq \left|\varepsilon_\sigma\right| \leq 3 \end{cases} \tag{B.11}$$

with

$$\begin{aligned} \rho_1\left(\varepsilon_\sigma\right) &= A + B\sqrt{1-\varepsilon_\sigma^2} + F\left(1-\left|\varepsilon_\sigma\right|\right)\left|\varepsilon_\sigma\right| \\ \rho_2\left(\varepsilon_\sigma\right) &= C + Dx^2 + F(1-x)\sqrt{x} \\ x &\equiv \left(3-\left|\varepsilon_\sigma\right|\right)/2 \end{aligned} \tag{B.12}$$

In the calculations, we used these values taken from Ref. [181]:

$$\begin{aligned} A &= \rho_{\text{Num}}(\pm 1) \approx 0.432 \\ B &= -0.1646 \\ C &= \tfrac{1}{\pi} = 0.3183 \\ D &= A - C \approx 0.1136 \\ F &= -0.0151 \end{aligned} \tag{B.13}$$

We calculated the density of states of e_g states using

$$\rho_\sigma(E) = \left| \frac{E - \frac{1}{2}\left(E_e + E_\parallel\right)}{(pd\sigma)^2} \right| \rho\left(\varepsilon_\sigma(E)\right) \tag{B.14}$$

Where we used the values $E_e = 2.34\,eV$, $E_\parallel = -6\,eV$ $pd\sigma = -2.23\,eV$ taken from Ref. [181]. The total DOS of t_{2g} and e_g is shown in Figure B.1.

III. Wedge model for quantum well LaAlO$_3$/SrTiO$_3$

We use a wedge model to calculate the energy of the quantum well E_Γ^n at the Γ point in the reciprocal space, using the expression (Ref. [74])

$$E_\Gamma^n = V_0 + 9 \times 10^{-7} \left(\frac{m_e}{m_z^*}\right)^{1/3} \left(n - \frac{1}{4}\right)^{2/3} F^{2/3} \tag{B.15}$$

where the superscript n refers to the different subband states of the quantum well. In our model, we use seven subbands $n = 1, \cdots, 7$. for each quantum well state (see Figure B.2a). The calculation considers the effective masses along the out-of-plane direction of t_{2g} states, where $m_z^* = 0.75 m_e$ for $d_{(yz/xz)}$ states and $m_z^* = 25 m_e$ for d_{xy} states, and $V_0 = -0.25\,eV$, $F = 120\,MV/m$.

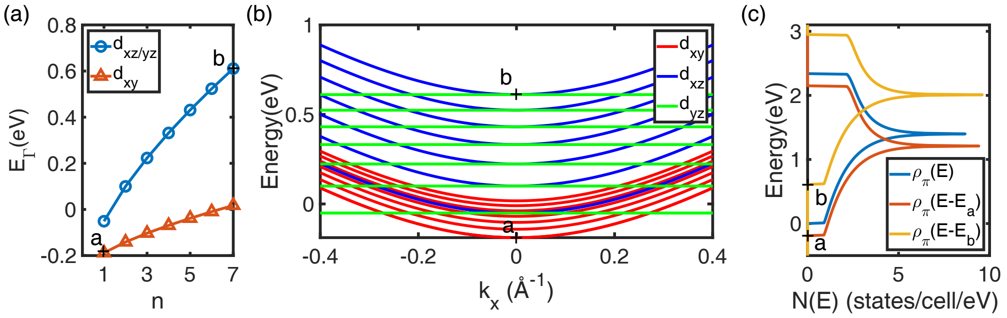

FIGURE B.2: (a) Energy levels at the Γpoint for different subbands $n = 1, \cdots, 7$, obtained through Equation B.8.(b) Energy dispersion of the subbands along the $\Gamma - X$ direction in reciprocal space. (c) Bulk density states used in Eqs. S10 with Wedge potential applied, the E_a and E_b correspond to the minimal and maximal energy of the quantum well in (a).

IV. Total quantum well states

Assuming the wedge potential of the quantum well lifts the degeneration of the bulk states, the approximate formula of the subbands ($n = 1, \cdots, 7$ for each of d_{xy} and $d_{(yz/xz)}$) can be written as:

$$E^n_{\vec{k}\pi(\alpha\beta)} = E_{\vec{k}\pi(\alpha\beta)} - E^n_\Gamma \tag{B.16}$$

That, the subbands of d_{xy} and $d_{(yz/xz)})$ states are separated, as Figure B.2b shows the dependence of the different quantum well states as a function of the wavevector along $\Gamma - X$. Figure B.2c shows the bulk density of states with any potential applied $\rho_\pi(E)$ and density of states with a minimum or maximum of E_Γ^n , which are notated as $\rho_\pi(E - E_a)$ and $\rho_\pi(E - E_b)$, respectively.

Similarly, for each $\pi-$type subband with potential applied, we calculated the density of states from the Equation B.9 replacing E with $E - E_\Gamma^n$.

$$\rho_\pi^n(E) = \rho_\pi^n(E - E_\Gamma^n) \tag{B.17}$$

and for each σ-type subband has,

$$\rho_\sigma^n(E) = \rho_\sigma^n(E - E_\Gamma^n) \tag{B.18}$$

The average total density of the states is obtained from the summation of all the subbands over the number:

$$\rho_{total}(E) = \sum_{n=1}^{3N} \left[\rho_\pi^n(E) + \rho_\sigma^n(E)\right] / 3N \tag{B.19}$$

Thus we get the approximate DOS of quantum well, as shown in the Figure B.3(a). The following sections will present the DOS of Excited DX, Ground DX, surface (Figure B.3(b)).

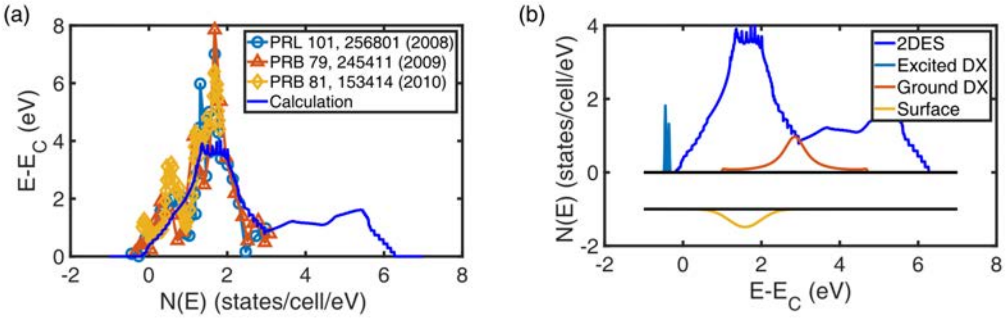

FIGURE B.3: (a) shows the total density of states (DOS) of the quantum well, average all the states derived from t_{2g} and e_g states per unit cell. For comparison, the figure also includes the DOS from DFT studies. (b) Density of states of structurally relaxed (c_0) DX-center states (inferred from DLTS) and unrelaxed DX-center states (c_1). The DOS of the QW are derived from t_{2g} and e_g states, as well as of surface states.

B.2.2 DX-center states

We introduce a localized DX-center excited state described by the spectral function:

$$\rho_{\mathrm{L}} = \frac{2C\Theta\left(w^2 - E^2\right)}{\sqrt{w^2 - E^2}\left[E^2 + \frac{C^2}{w^2 - E^2}\right]} \tag{B.20}$$

where the C is coupling strength, w is the width and Θ is step function. To fit the data (as shown Figure B.4c), the parameters is: $C = 0.65$, $W = 1.85$, and the center of the localized state is at 2.85 eV.

For the ground DX-center state we used the normalized expression:

$$\rho_{\mathrm{i}}^{I}(E) \cong \frac{a_1}{a_1+a_2}\sqrt{\frac{w}{\pi}}e^{-w\left(E-E_1^0\right)^2}+\frac{a_2}{a_1+a_2}e^{-w\left(E-E_2^0\right)^2} \tag{B.21}$$

where $E_1^0 = -0.17\,eV$ and $E_2^0 = -0.26\,eV$ from the bottom of conduction band, $w = 3.09 \times 10^3$, $a_1 = 2.4 \times 10^{-14}$, $a_2 = 3.3 \times 10^{-14}$. These parameters are determined through fitting the data measured by deep-level transient spectroscopy (DLTS).

$$D_{fit}(E) = a_1 e^{-w\left(E-E_1^0\right)^2} + a_2 e^{-w\left(E-E_2^0\right)^2} \tag{B.22}$$

B.2.3 Surface states

For the surface states we introduce a single Gaussian function:

$$\rho_s^I(E) \cong \sqrt{\frac{w}{\pi}}e^{-W_s\left(E-E_s^0\right)^2} \tag{B.23}$$

where $E_s^0 = 1.77\,eV$; $W_s = 3$. We assume the density of the surface states $\rho_s = 0.5\rho_s^I(E)$. The assumptions of the occupancy of the defects and surface states do not affect the distribution of the DOS, but they influence the ratio of the transition probability. Including the trap states (inferred from DLTS), all the density of states can be profiled, as shown in Figure B.3b.

B.3 Deep-level transient spectroscopy (DLTS)

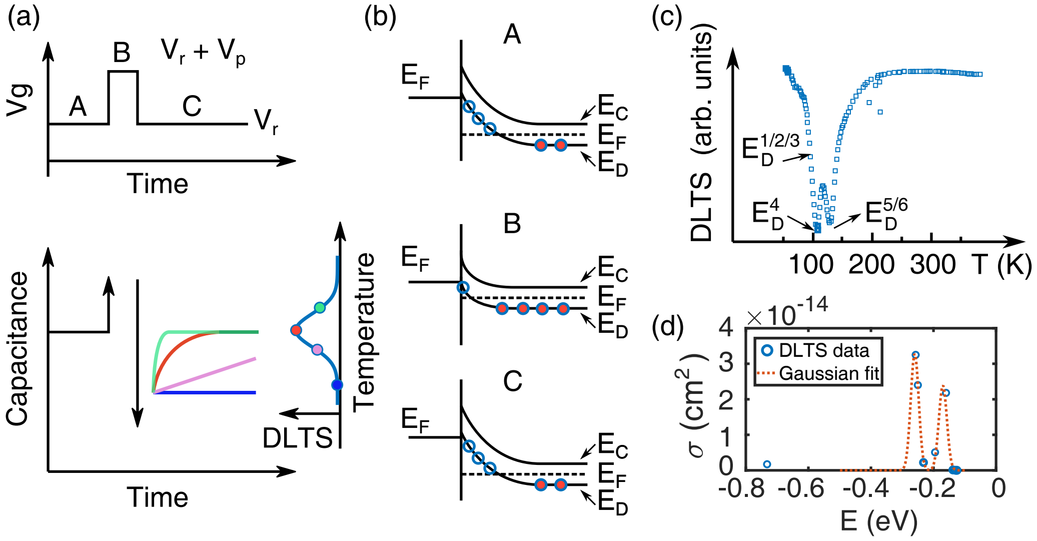

FIGURE B.4: (a) Schematics of DLTS measurement. The capacitance is measured at the reversal voltage. Then a transient pulse is added to charge the trap, resulting in a decrease in capacitance. After the pulse, the capacitance is recovering based on the temperature. (b) Schematics of de-charging and charging process in traps. (c) DLST signal vs temperature. (d) DLTS data and a bi-Gaussian fitting.

We carried out deep-level transient spectroscopy (DLTS) to detect trap levels below the Fermi energy. In the experiments, we grow samples with M/I/QW structure (Au [10 nm]/LaAlO$_3$ [

$\sim 4\,nm$]/STO). To observe a transient transition of electrons from trap levels to the conduction level, we measured the capacitance after a pulse of gate voltage (Figure B.4a top). At the reverse bias V_r , the trap levels are partly filled. Then a pulse V_p with hundred milliseconds width is applied, so that nearly all traps are occupied. Subsequently, after the end of the pulse, the trapped electrons are emitted into the conduction band (Figure B.4b). This recovery process depends on temperature, which can be measured by DLTS (Figure B.4a bottom). The trap levels can be extracted from the DLTS analysis (relative details can refer Ref. [185]). As shown in Figure B.4c, the peak is located at the $E_D^4 \sim -0.195\,eV$ and $E_D^{5/6} \sim -0.250\,eV$. A bi-Gaussian function is used to fit the data of capture cross section vs energy (Figure B.4d). The parameters are used to profile the DOS of DX-centers.

B.4 Calculation of the photoconductance

B.4.1 Photoexcitation with single pulses

The photoexcitation can proceed by either excitation of the DX-center or excitation towards surface states via quantum tunneling. In the former case, we calculate the photoconductance via DX-center excitation using the Einstein model:

$$\Sigma_{in} = p\frac{\pi}{\hbar w}\iint \sum_{m=-\infty}^{m=\infty} \delta\left[\hbar w - \hbar w_m\right] \rho_L\left(\epsilon_L\right) \rho_i\left(\epsilon_i\right) e^{-\frac{g}{2N} + I_m(\gamma) e^{\frac{m\hbar w_0}{k_B T}}} d\epsilon_L d\epsilon_i \tag{B.24}$$

where we used the following values, $\hbar w_m = (\epsilon_L - \epsilon_i) + \hbar w_0$, $g = 1$, $\gamma = 4.97g$, $N = 2$, $\hbar w_0 = 10\,meV$; $k_B T = 25\,meV$; The $I_m(\gamma)$ is modified Bessel function. The value of p is adjusted based on the data.

The photoexcitation towards surface states via quantum tunneling is calculated using

$$\Sigma_{\text{out}} = T\int \mathrm{d}\epsilon \rho_L(\epsilon)\rho_i(\epsilon) = 4\pi T\iint \mathrm{d}\epsilon_{\mathrm{L}} d\epsilon_i \rho_L\left(\epsilon_s\right) \rho_i \delta\left(\epsilon_s - \epsilon_i - \hbar w\right) \tag{B.25}$$

The total scattering function is calculated as $\sum_{tot} = \sum_{in} - \sum_{out}$. The photoconductance change against the photo-energy (shown in Figure 3.1c) is used to examine and decide the parameters including the DOS, transition, quantum tunneling probability.

B.4.2 Photoexcitation with two-pulse sequences

We carry out the simulations of two-pulse sequences according to the steps described in the following. The conductance increases under the illumination with the first pulse, which we calculate using the total scattering function $\sum_{tot}$. Subsequently, after the first pulse switches off, the conductance decreases. Such decay process is characterized using the bi-exponential function to fit the data (see Figure B.5a).

$$\mathrm{F}_\lambda = \mathrm{A}\left(\mathrm{w}\exp\left(-\frac{\mathrm{t}}{\tau_1}\right) + (1-\mathrm{w})\exp\left(-\mathrm{t}/\tau_2\right)\right) \tag{B.26}$$

where A is the excitation state, τ_1 and τ_2 are characteristic time, and the w is weight for the two different characteristic time. We give the parameters in Table B.1:

TABLE B.1: The parameters of the recovery fitting

λ(nm)	A	w	$\tau_1(s)$	$\tau_2(s)$
638 (R)	1.529	0.8751	0.871	4.1e4
520 (G)	2.197	0.8156	1.008	30.09
450 (B)	2.796	0.6907	0.665	19.26
405 (V)	7.523	0.797	1.172	22.29

The final of the population of the quantum well after the second pulse depends on the balance between photoexcitation of DX-centers and wavelength-dependent quantum tunneling (QT). As illustrated in Figure B.5(b), the incorporation of photoexcitation via QT is essential to understand the depletion of carriers after a second pulse of red light. We give more details about these calculations in the following.

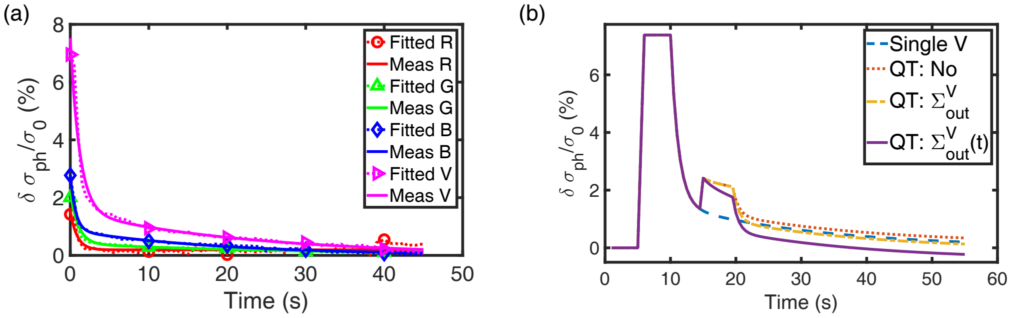

FIGURE B.5: (a) The data and fitted lines of the recovery from the excitation under the illumination with different wavelengths (see Table T1 for reference of fitted parameters). (b) The simulation of the conductance recovery based on different models, where the first pulse is violet and the second one is red. As a reference, the dashed blue line shows the recovery after a single pulse of violet light. The dotted red line presents the calculation based on the model without photoexcitation via quantum tunneling (QT), while the line-doted yellow line (which considers the QT process is time-independent) and purple line (the QT process is relative to the decay process from the first pulse) are resulted from the model with QT.

The models with or without quantum tunneling are compared in the Table B.2

Under the illumination with the first violet pulse, the photoconductance is $\sum^V_{No} = \sum^V_{QT}$ for the model with or without QT. The excitation values are same and then decay at same rate, that is $\sum^{D1}_{No} = \sum^{D1}_{QT} = F_V(A^{D1}, t^V_{off} - t^R_{on})$, where $t^V_{off} - t^R_{on}$ means the duration started from the moment the violet is switched off to the moment the red is switched on, and $A^{D1} = \sum^V_{No} = \sum^V_{QT}$.

Considering the second pulse of the red light, for the model without QT, $\sum^R_{No} = \sum^{R'}_{in} + F_V(A^{D1}, t^R_{on} - t^R_{off})$, which is simply treated as the addition of the increment excited by the red and decrement from the first pulse of violet during the red light is keeping on. For the model with QT, whereas, $\sum^R_{QT} = \sum^R_{in} + \sum^R_{out}(t) + F_V(A^{D1}, t^R_{on} - t^R_{off})$, where $\sum^R_{in}$ describes the electrons excited towards the quantum well. The surface charges from the QT not only are depleting partial number of the interface electrons but also are enhancing the attractive of the trap centers resulting in barrier shift (seen in the Figure 2). Hence, the quantity of the quantum tunneling $\sum^V_{out}(t)$ is simply assumed as $\sum^V_{out}(t) = \sum^V_{out}(1 + A_{QT}(\sum_Q T^D 1(t^R_{on} - \sum^{D1}_{QT}(t^R_{on} - t^R_{off}))$, the second term means that as more electrons travel back the ground state, and more electrons quantum-tunnel to the surface, where parameter $A_{QT} = 5$ in the simulation based on the data.

After the second pulse of red light is switched off, the decaying process can be fitted by adding the recovery from the first pulse of violet and that of red, although the real physical process cannot differentiate them. For the model without QT, $\sum_{No}^{D2} = F_V(A^{D1}, t_{off}^R - t_{end}) + F_R(A_{No}^{D2}, t_{off}^R - t_{end})$, while for the model with QT, $\sum_{QT}^{D2} = F_V(A^{D1}, t_{off}^R - t_end) + F_R(t_{off}^R - t_{end}) - \sum_{out}^R(end)$, where the amplitude $A_{No}^{D2} = \sum_{QT}^R$ and $A_{QT}^{D2} = \sum_{in}^R + F_V(A^{D1}, t_{on}^R - t_{off}^R) = \sum_{QT}^R - \sum_{out}^V(t)$. We assume only the electrons in the quantum well are jumping back to the ground state, so the fitting function should exclude the final surface electrons $\sum_{out}^V(end)$.

TABLE B.2: Comparison of model with or without quantum tunneling

Process	No QT	QT
Violet on	$\Sigma_{No}^V = \Sigma_{in}^{V'}$	$\Sigma_{QT}^V = \Sigma_{in}^V - \Sigma_{out}^V$
Decay	$\Sigma_{No}^{D1} = F_V(A^{D1}, t_{off}^V - t_{on}^R)$	$\Sigma_{No}^{D1} = \Sigma_{QT}^{D1} = F_V(A^{D1}, t_{off}^V - t_{on}^R)$
Red on	$\Sigma_{No}^R = \Sigma_{in}^{R'} + \mathrm{F_v}\left(\mathrm{t_{on}^R} - \mathrm{t_{off}^R}\right)$	$\Sigma_{QT}^R = \Sigma_{in}^R + \Sigma_{\mathrm{out}}^V(t) + \mathrm{F_V}\left(\mathrm{t_{on}^R} - \mathrm{t_{off}^R}\right)$
Decay	$\Sigma_{No}^{D2} = \mathrm{F_V}\left(\mathrm{t_{off}^R} - t_{end}\right)$ $+F_R\left(\mathrm{t_{off}^R} - t_{end}\right)$	$\Sigma_{QT}^{D2} = \mathrm{F_V}\left(\mathrm{t_{off}^R} - t_{end}\right)$ $+F_R\left(\mathrm{t_{off}^R} - end\right) - \Sigma_{out}^V(end)$

B.5 Photoexcitation without DX-centers

If we only consider the conduction band of the quantum well without a localized DX-center excited state (Figure S6(a)), the density of states is given by:

$$\rho_c = \rho_\pi^n(E > 0) + \rho_\sigma^n(E > 0) \tag{B.27}$$

According to Equation 3.4, the photoexcitation can be calculated in this case by replacing $n_D X$ with ρ_c of Equation 3.5. As shown in Figure B.6b, if we assume photoexcitation without DX-centers, the photoconductance should decrease with increasing photon energy, in contradiction with experiments.

B.6 Configuration-coordinate model

The persistent photoconductance can be interpret using the configuration-coordinate model (Refs. [87, 92, 94]), which takes the couple of electronic and vibrational system of the neutral DX centers into account. We assume that the lattice vibrations do not change the electronic states, so that the Hamiltonian is as follows (Ref 9):

$$\begin{aligned} H &= H_E + H_{EL} + H_L \\ &= \left[p_e^2/2m^* + V_{DX}(r)\right] \\ &+ BQV_{DX}(r) + \left(P_L^2/2M^* + \tfrac{1}{2}M^*\omega^2Q^2\right) \end{aligned} \tag{B.28}$$

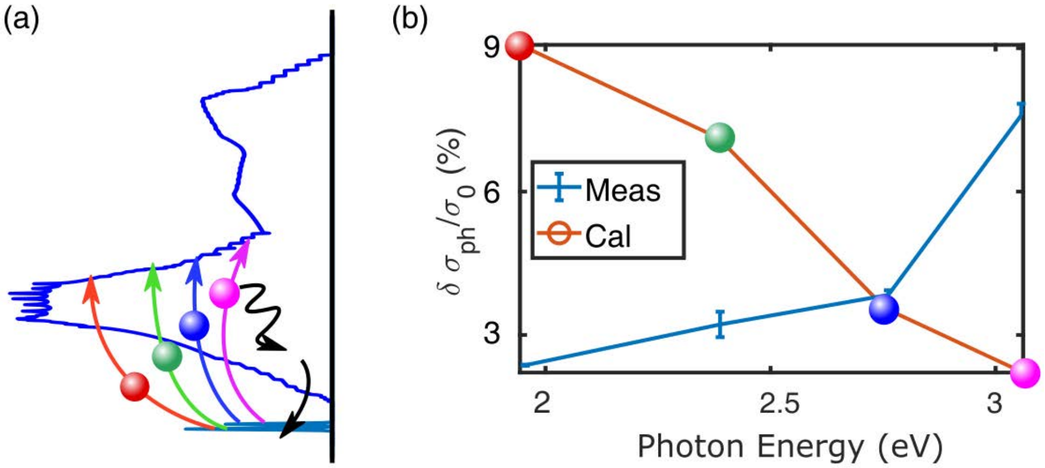

FIGURE B.6: (a) Schematic depiction of photoexcitation without DX-centers, under illumination with different wavelengths (638, 520, 450 and 405 nm) . (b) Calculated photoconductance using Equation 3.5. Assuming a model based on photoexcitation without DX-centers leads to a wrong prediction of the spectral response of the photoconductance.

where, the single lattice coordinate Q denotes for the vibrations of the DX centers. Without considering vibrations $Q = 0$, the term $H_E = p_e^2/2m^* + V_D X(r)$ describes the electronic behavior with an effective mass m^* at the potential-well $V_{DX}(r)$, $H_{EL} = BQV_{DX}(r)$ defines the shift of the potential-well depth by a lattice displacement Q, and the vibration of the DX system can be approximately considered as a harmonic oscillator along $Q = 0$, which can be described as $H_L = P_L^2/2M^* + 1/2M^*\omega^2Q^2$.

The eigenfunctions are supported as $|c\rangle$, $|v\rangle$ and $|D\rangle$ for the de-trapped states at the bottom of the valence band (VB) and conduction band (CB), and a trapped state (DB). Concerning the lattice coordinate Q, the value of $V_{DX}(r)$ is approximate to a constant. Neglecting the probability $\langle c|V_{DX}|c\rangle = 0$ and $\langle v|V_{DX}|v\rangle = 0$, the energies of the free states are independent of Q, while probability $\langle D|V_{DX}|D\rangle \neq 0$ causes the V_{DX} change. Hence, the Hamiltonian matrix without considering any off-diagonal elements is written:

$$H = \begin{matrix} [E_{v0} + U_i & 0 & 0 \\ 0 & E_{c0} + U_i & 0 \\ 0 & 0 & E_{\mathrm{d}0} + V_{DX} + \mathrm{U_i} + H_{EL}] \end{matrix} \tag{B.29}$$

where, the energies at the bottom of the VB and CB are $E_{v0} = p_e^2/2m_{VB}^*$ and $E_{c0} = p_e^2/2m_{CB}^*$, respectively. The energy at the trapped state without vibration is $E_{d0} = p_e^2/2m_{DB}^*$, the oscillation Hamiltonian $U_i = P_L^2/2M^* + 1/2M^*\omega^2Q^2 = 0.2Q^2$. To fit the description of the large-lattice-relaxation model (Ref 8) and our measurement, the parameters are chose as: $E_{v0} = 0$, $E_{c0} = 3\,eV$, $E_{t0} = 4.48\,eV$, $V_{DX} = -0.8\,eV$, $U_i = 0.2Q^2$ and $H_{EL} = QV_{DX}$. Substituting them into the Equation B.29, the relation of the bands vs Q is obtained (Figure B.7b). For simplicity, we only focus the electronic state without considering the lattice oscillation, approximately, the electronic energy isn't changed by the lattice vibration (see in Figure B.7a). Notably, the equilibrium positions are different in the de-trapped state and trapped state of the DX-centers. At the such different equilibrium the thermal vibrations of the electrons approximate to be identical, which is shown by the amplitude of the smaller arrows in the Figure B.7a. The equilibrium changed by the lattice vibrations which is presented by the large arrow in Figure B.7a. The detailed discussion can be found in the reference Ref [94].

If the DX center is ionized or external field is applied, the potential V_DX will be altered: $V_{DX} = V_{DX} + E_{ext}$ (E_{ext} denotes external energy), i.e., the positive DX centers tend to attract an electrons or, in our case, the electric field produced by the negative electrons at the surface of $LaAlO_3$ will push the electrons towards the DX center almost located at the $SrTiO_3$ side. Therefore creations of the positive DX centers and negative surface charges by the quantum tunneling can increase the depth of trapped potential, we assume the potential change to $V_{DX} = -0.8 - 0.1\,eV = -0.9\,eV$ (seen in Figure B.7(c)).

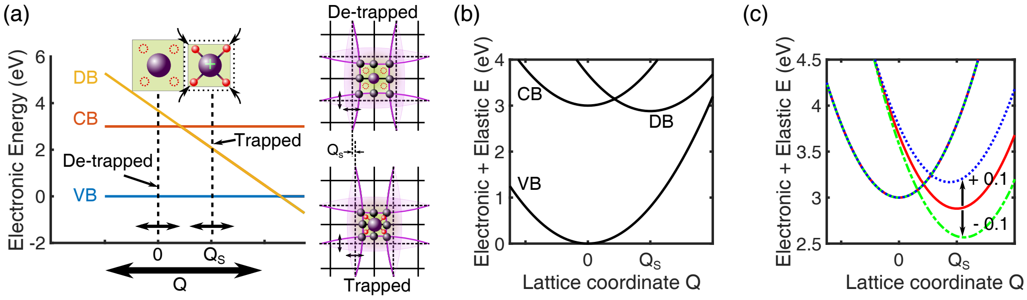

FIGURE B.7: (a) The electronic energy is assumed to be unchanged by the lattice vibrations (reproduced the figure in the Ref. [94]), which is represented by the large arrow. The DX-center with unoccupied state or occupied state vibrate along different equilibrium position denoted as $Q = 0$ and $Q = Q_S$, respectively, along the equilibrium the electrons thermally vibrate, which is denoted by the smaller arrows. The right panel shows the sketch illustrating the vibrations. (b) The total energy vs lattice coordinate, the CB and VB are separated by energy gap $\Delta E = 3\,eV$, and the bottom of the DB is located slightly below the bottom of the CB (seen in Ref. [92]). (c) The shift of the DB caused by ionizing of electric field with respective to adding the positive or negative energy.

Appendix C

Calculation of bulk band structure with matlab

The Hamiltonian of perovskite is given by the Ref. [181].

$$H(\vec{r}) = -\frac{\hbar^2}{2m}\nabla^2 + v_{\text{eff}}(\vec{r}) \tag{C.1}$$

The elements of the Hamiltonian are written using Linear combination of atomic orbitals (LCAO) methods.There are 14 orbitals used to calculate the bandstructure:

$$\begin{array}{ccc} d_{z^2}(\vec{r}) \Rightarrow 1 & p_z\left(\vec{r}-a\vec{e}_z\right) \Rightarrow 2 & d_{x^2-y^2}(\vec{r}) \Rightarrow 3 \\ & p_x\left(\vec{r}-a\vec{e}_x\right) \Rightarrow 4 & p_y\left(\vec{r}-a\vec{e}_y\right) \Rightarrow 5 \\ d_{xy}(\vec{r}) \Rightarrow 6 & p_x\left(\vec{r}-a\vec{e}_y\right) \Rightarrow 7 & p_y\left(\vec{r}-a\vec{e}_x\right) \Rightarrow 8 \\ d_{xz}(\vec{r}) \Rightarrow 9 & p_x\left(\vec{r}-a\vec{e}_z\right) \Rightarrow 10 & p_z\left(\vec{r}-a\vec{e}_x\right) \Rightarrow 11 \\ d_{yz}(\vec{r}) \Rightarrow 12 & p_y\left(\vec{r}-a\vec{e}_z\right) \Rightarrow 13 & p_z\left(\vec{r}-a\vec{e}_y\right) \Rightarrow 14 \end{array} \tag{C.2}$$

These 14 orbitals comprise 14 × 14 matrix with $H - E_{\vec{k}v}I$ with vanishing determinat. To calculate

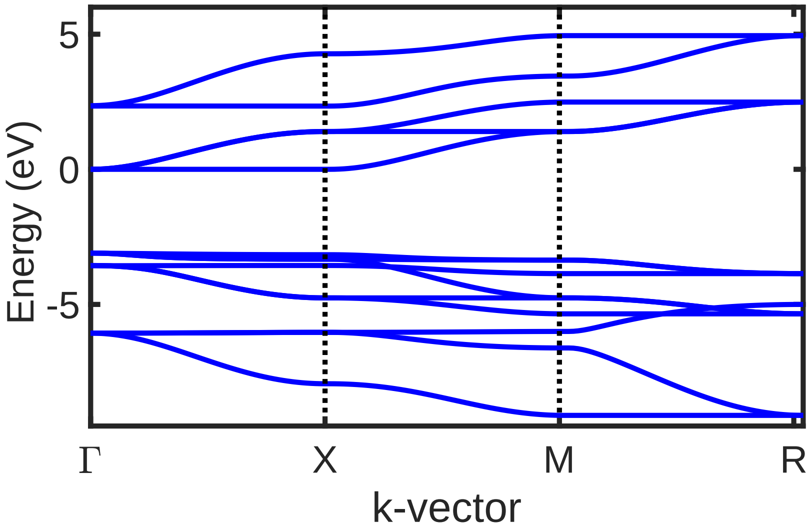

FIGURE C.1: Energy Band of bulk SrTiO$_3$ for the parameters (all in eV),$E_{\parallel} = -6$; $E_{\perp} = -3.36$; $Ee = 2.34$; $pd\sigma = -2.23$; $pd\pi = 1.29$

the SrTiO$_3$ band structure, the main parameters are adjusted according the DFT data [183]: $E_{\parallel} = -6$; $E_{\perp} = -3.36$; $Ee = 2.34$; $pd\sigma = -2.23$; $pd\pi = 1.29$;

```
%-------------------------------------------------------------------------
%  Perovskite Band structure
%  2019-7-2
%-------------------------------------------------------------------------
% Copyright (c) 2019 Chen Yu
%-------------------------------------------------------------------------

clear all
close all

% parameters
Ep =-3.36;  E11 = -6; Et =0;  Ee = 2.34;
pds = -2.23;  pdp = 1.29;
ppp = 0.05; pps = -0.2;
b = pps - ppp;  c = pps+ ppp; a = 1; % Angstrom

% k vectors
kmax=pi/2/a;Nt=51;%X-direction
K1 = linspace(0,kmax, Nt).*[1 0 0]';
K2 = linspace(0,kmax, Nt).*[0 1 0]' +[kmax,0,0]' ;
K3 = linspace(0,kmax, Nt).*[0 0 1]' + [kmax,kmax,0]' ;

K = [K1 K2 K3];

%  Hamiltonian
for Nk=1:3*Nt
k=K(:,Nk);
Sx = sin(k(1)*a); Sy = sin(k(2)*a); Sz = sin(k(3)*a);
Cx = cos(k(1)*a); Cy = cos(k(2)*a); Cz = cos(k(3)*a);

h=[  Ee/2    2*j*pds*Sz     0     -j*pds*Sx    -j*pds*Sy   0   0   0 0 0 0 0 0 0;
0 E11/2 0 -2*b*Sx*Sz -2*b*Sy*Sz 0 0 0 0 0 2*c*Cx*Cz 0 0 2*c*Cy*Cz
0 0 Ee/2 sqrt(3)*j*pds*Sx -sqrt(3)*j*pds*Sy 0 0 0 0 2*c*Cz*Cx 0 0 0 0;
0 0 0 E11/2 -2*b*Sx*Sy 0 2*c*Cx*Cy 0 0 2*c*Cz*Cx 0 0 0 0;
0 0 0 0 E11/2 0 0 2*c*Cx*Cy 0 0 0 0 2*c*Cy*Cz 0;
0 0 0 0 0 Et/2 2*j*pdp*Sy 2*j*pdp*Sx 0 0 0 0 0 0;
0 0 0 0 0 0 Ep/2 -2*b*Sx*Sy 0 4*ppp*Cy*Cz 0 0 0 0;
0 0 0 0 0 0 0 Ep/2 0 0 0 0 4*ppp*Cx*Cz 0;
0 0 0 0 0 0 0 0 Et/2  2*j*pdp*Sz  2*j*pdp*Sx 0 0 0;
0 0 0 0 0 0 0 0 0 Ep/2 -2*b*Sx*Sz 0 0 0;
0 0 0 0 0 0 0 0 0 0 Ep/2 0 0 4*ppp*Cx*Cy;
0 0 0 0 0 0 0 0 0 0 0 Et/2 2*j*pdp*Sz 2*j*pdp*Sy;
0 0 0 0 0 0 0 0 0 0 0 0 Ep/2 -2*b*Sy*Sz;
0 0 0 0 0 0 0 0 0 0 0 0 0 Ep/2];
H=h+h';
[V,D]=eig(H);
eiglst = sum(D);
E(Nk,:) = sort(real(eiglst));
%      X(Nk)=-(Nk-1)/(Nt-1);%L-direction
```

```
X1(Nk)=(Nk-1)/(Nt-1);%X-direction
end

figure
hold on
h=plot(X1,E,'b','linewidth',LineWidth);
set(gca,'linewidth',LineWidth,'fontsize',FontSize);
set(gca,'xtick',[0 1 2 3], 'xticklabel',{'\Gamma','X','M','R'})
line([1 1],[-9 6],'LineWidth',LineWidth,'Color','k','LineStyle',':');
line([2 2],[-9 6],'LineWidth',LineWidth,'Color','k','LineStyle',':');
xlabel('k-vector')
ylabel('Energy (eV) ','fontsize',FontSize);
grid off
box on
ylim([-9.5 6])

% figure is saved as pdf
fig = gcf;
fig.PaperUnits = 'inches';
fig.PaperPosition = [0 0  10 6.16];
fig.PaperSize = [10 6.16  ];
print(['E(k)_STO_CB_Long'],'-dpdf','-r0')
```

CODE C.1: Bulk band structure of $SrTiO_3$

List of publications and communications

List of scientific publications:

- Chen, Y., Casals, B. & Herranz, G. *Plasticity of Persistent Photoconductance of Amorphous* $LaAlO_3/SrTiO_3$ *Interfaces under Varying Illumination Conditions*. ACS Appl. Electron. Mater. 1, 810816 (2019).

- Chen, Y., Casals, B., Sánchez, F. & Herranz, G. *Solid-State Synapses Modulated by Wavelength-Sensitive Temporal Correlations in Optic Sensory Inputs*. ACS Appl. Electron. Mater. 1, 11891197 (2019).
- Chen, Y., et al., *Photoinduced tunable carrier accumulation and depletion in a quantum well* (In preparation, to be submitted)

List of conferences:

- Poster presentation at 25th International Workshop on Oxide Electronics, Les Diablerets, Switzerland, October 1, 2018

- Poster Presentation at TO-BE cost action, spring meeting, Sant Feliu de Guixols - Spain, March 12, 2018

- Poster Presentation at Nanoselect NOE-Annual Meeting, Sant Feliu de Guixols - Spain, July 10, 2017

- Poster Presentation at International School of Oxide Electronics (ISOE2017), Corsica - France, April 11, 2017

- Poster Presentation at Nanoselect NOE-Annual Meeting, Sant Feliu de Guixols - Spain, June 8, 2016

Bibliography

[1] D. Castelvecchi. “Black hole pictured for first time in spectacular detail”. In: *Nature* 568 (Apr. 2019), pp. 284–285. DOI: 10.1038/d41586-019-01155-0.

[2] EHT Press Conference. *National Science Foundation/EHT Press Conference Revealing First Image of Black Hole - YouTube*. 2019.

[3] Y. LeCun, Y. Bengio, and G. Hinton. “Deep learning”. In: *Nature* 521.7553 (May 2015), pp. 436–444. ISSN: 0028-0836. DOI: 10.1038/nature14539.

[4] A. Krizhevsky, I. Sutskever, and G. E. Hinton. “ImageNet Classification with Deep Convolutional Neural Networks”. In: *Proceedings of the 25th International Conference on Neural Information Processing Systems - Volume 1*. NIPS’12. Lake Tahoe, Nevada: Curran Associates Inc., 2012, pp. 1097–1105.

[5] G. Hinton et al. “Deep Neural Networks for Acoustic Modeling in Speech Recognition: The Shared Views of Four Research Groups”. In: *IEEE Signal Processing Magazine* 29.6 (Nov. 2012), pp. 82–97. ISSN: 1053-5888. DOI: 10.1109/MSP.2012.2205597.

[6] I. Sutskever, O. Vinyals, and Q. V. Le. “Sequence to sequence learning with neural networks”. In: *Advances in neural information processing systems*. 2014, pp. 3104–3112.

[7] R. Collobert et al. “Natural language processing (almost) from scratch”. In: *Journal of machine learning research* 12.Aug (2011), pp. 2493–2537.

[8] A. Bordes, S. Chopra, and J. Weston. “Question Answering with Subgraph Embeddings”. In: *Proceedings of the 2014 Conference on Empirical Methods in Natural Language Processing (EMNLP)*. Doha, Qatar: Association for Computational Linguistics, Oct. 2014, pp. 615–620. DOI: 10.3115/v1/D14-1067.

[9] T. Chouard. “The Go Files: AI computer wraps up 4-1 victory against human champion”. In: *Nature* (Mar. 2016). ISSN: 0028-0836. DOI: 10.1038/nature.2016.19575.

[10] N. Jones. “Computer science: The learning machines”. In: *Nature* 505.7482 (Jan. 2014), pp. 146–148. ISSN: 0028-0836. DOI: 10.1038/505146a.

[11] D. E. Rumelhart, G. E. Hinton, and R. J. Williams. “Learning representations by back-propagating errors”. In: *Nature* 323.6088 (Oct. 1986), pp. 533–536. ISSN: 0028-0836. DOI: 10.1038/323533a0.

[12] Y. LeCun et al. “Handwritten digit recognition with a back-propagation network”. In: *Advances in neural information processing systems*. 1990, pp. 396–404.

[13] Y. Lecun et al. “Gradient-based learning applied to document recognition”. In: *Proceedings of the IEEE* 86.11 (1998), pp. 2278–2324. ISSN: 00189219. DOI: 10.1109/5.726791.

[14] D. Ielmini and H. S. Wong. "In-memory computing with resistive switching devices". In: *Nature Electronics* 1.6 (2018), pp. 333–343. ISSN: 25201131. DOI: `10.1038/s41928-018-0092-2`.

[15] G. E. Moore. "Cramming more components onto integrated circuits, Electronics, 38 (8), S. 114-117,(1965) oder: GE Moore". In: *Electronics* 38 (1965), pp. 114–117.

[16] W. A. Wulf and S. A. McKee. "Hitting the memory wall". In: *ACM SIGARCH Computer Architecture News* 23.1 (Mar. 1995), pp. 20–24. ISSN: 01635964. DOI: `10.1145/216585.216588`.

[17] M. M. Waldrop. "The chips are down for Moore's law". In: *Nature* 530.7589 (Feb. 2016), pp. 144–147. ISSN: 0028-0836. DOI: `10.1038/530144a`.

[18] J. G. Brookshear. *Computer science: an overview*. Addison-Wesley Publishing Company, 2008.

[19] P. A. Merolla et al. "A million spiking-neuron integrated circuit with a scalable communication network and interface". In: *Science* 345.6197 (2014), pp. 668–673. ISSN: 10959203. DOI: `10.1126/science.1254642`.

[20] Y.-H. Chen et al. "Eyeriss: An Energy-Efficient Reconfigurable Accelerator for Deep Convolutional Neural Networks". In: *IEEE Journal of Solid-State Circuits* 52.1 (Jan. 2017), pp. 127–138. ISSN: 0018-9200. DOI: `10.1109/JSSC.2016.2616357`.

[21] N. P. Jouppi et al. "In-Datacenter Performance Analysis of a Tensor Processing Unit". In: *Proc. 44th Int. Symp. Comp. Architecture* (2017). DOI: `10.1145/3079856.3080246`.

[22] J. T. Pawlowski. "Hybrid memory cube (HMC)". In: *2011 IEEE Hot Chips 23 Symposium (HCS)*. IEEE, Aug. 2011, pp. 1–24. ISBN: 978-1-4673-8877-1. DOI: `10.1109/HOTCHIPS.2011.7477494`.

[23] D. U. Lee et al. "25.2 A 1.2V 8Gb 8-channel 128GB/s high-bandwidth memory (HBM) stacked DRAM with effective microbump I/O test methods using 29nm process and TSV". In: *2014 IEEE International Solid-State Circuits Conference Digest of Technical Papers (ISSCC)*. IEEE, Feb. 2014, pp. 432–433. ISBN: 978-1-4799-0920-9. DOI: `10.1109/ISSCC.2014.6757501`.

[24] Q. Wan et al. "Emerging Artificial Synaptic Devices for Neuromorphic Computing". In: *Advanced Materials Technologies* 4.4 (2019), pp. 1–34. ISSN: 2365709X. DOI: `10.1002/admt.201900037`.

[25] J. Hasler and B. Marr. "Finding a roadmap to achieve large neuromorphic hardware systems". In: *Frontiers in Neuroscience* 7 (Sept. 2013), p. 118. ISSN: 1662-453X. DOI: `10.3389/fnins.2013.00118`.

[26] I. Boybat et al. "Neuromorphic computing with multi-memristive synapses". In: *Nature Communications* 9.1 (2018), pp. 1–12. ISSN: 20411723. DOI: `10.1038/s41467-018-04933-y`.

[27] E. R. Kandel et al. *Principles of neural science*. Vol. 4. McGraw-hill New York, 2000.

[28] G. Indiveri and S.-C. Liu. "Memory and Information Processing in Neuromorphic Systems". In: *Proceedings of the IEEE* 103.8 (Aug. 2015), pp. 1379–1397. ISSN: 0018-9219. DOI: `10.1109/JPROC.2015.2444094`.

[29] M. Di Ventra and Y. V. Pershin. "The parallel approach". In: *Nature Physics* 9.4 (Apr. 2013), pp. 200–202. ISSN: 1745-2473. DOI: `10.1038/nphys2566`.

[30] A. N. Tait et al. "Silicon Photonic Modulator Neuron". In: *Physical Review Applied* 11.6 (2019), p. 1. ISSN: 23317019. DOI: `10.1103/PhysRevApplied.11.064043`.

[31] M. D. Pickett, G. Medeiros-Ribeiro, and R. S. Williams. "A scalable neuristor built with Mott memristors". In: *Nature Materials* 12.2 (Feb. 2013), pp. 114–117. ISSN: 1476-1122. DOI: `10.1038/nmat3510`.

[32] M. Davies et al. "Loihi: A Neuromorphic Manycore Processor with On-Chip Learning". In: *IEEE Micro* 38.1 (Jan. 2018), pp. 82–99. ISSN: 0272-1732. DOI: `10.1109/MM.2018.112130359`.

[33] A. Graves et al. "Hybrid computing using a neural network with dynamic external memory". In: *Nature* 538.7626 (Oct. 2016), pp. 471–476. ISSN: 0028-0836. DOI: `10.1038/nature20101`.

[34] J. Schemmel et al. "A wafer-scale neuromorphic hardware system for large-scale neural modeling". In: *Proceedings of 2010 IEEE International Symposium on Circuits and Systems*. IEEE, May 2010, pp. 1947–1950. ISBN: 978-1-4244-5308-5. DOI: `10.1109/ISCAS.2010.5536970`.

[35] B. V. Benjamin et al. "Neurogrid: A Mixed-Analog-Digital Multichip System for Large-Scale Neural Simulations". In: *Proceedings of the IEEE* 102.5 (May 2014), pp. 699–716. ISSN: 0018-9219. DOI: `10.1109/JPROC.2014.2313565`.

[36] S. B. Furber et al. "The SpiNNaker Project". In: *Proceedings of the IEEE* 102.5 (May 2014), pp. 652–665. ISSN: 0018-9219. DOI: `10.1109/JPROC.2014.2304638`.

[37] T. Ferreira de Lima et al. "Progress in neuromorphic photonics". In: *Nanophotonics* 6.3 (Jan. 2017), pp. 577–599. ISSN: 2192-8614. DOI: `10.1515/nanoph-2016-0139`.

[38] S Löwel and W Singer. "Selection of intrinsic horizontal connections in the visual cortex by correlated neuronal activity." In: *Science (New York, N.Y.)* 255.5041 (Jan. 1992), pp. 209–12. ISSN: 0036-8075. DOI: `10.1126/science.1372754`.

[39] M. M. Waldrop. "Neuroelectronics: Smart connections". In: *Nature* 503.7474 (2013), pp. 22–24. ISSN: 00280836. DOI: `10.1038/503022a`.

[40] C. Mead. "Analog VLSI and neutral systems". In: *NASA STI/Recon Technical Report A* 90 (1989).

[41] D. Psaltis et al. "Holography in artificial neural networks". In: *Nature* 343.6256 (Jan. 1990), pp. 325–330. ISSN: 0028-0836. DOI: `10.1038/343325a0`.

[42] Y. Shen et al. "Deep learning with coherent nanophotonic circuits". In: *Nature Photonics* 11.7 (July 2017), pp. 441–446. ISSN: 1749-4885. DOI: `10.1038/nphoton.2017.93`.

[43] J. Lazzaro et al. “Silicon auditory processors as computer peripherals”. In: *IEEE Transactions on Neural Networks* 4.3 (May 1993), pp. 523–528. ISSN: 10459227. DOI: `10.1109/72.217193`.

[44] M. Mahowald. “VLSI analogs of neuronal visual processing: a synthesis of form and function”. In: (1992).

[45] G.-q. Bi and M.-m. Poo. “Synaptic Modifications in Cultured Hippocampal Neurons: Dependence on Spike Timing, Synaptic Strength, and Postsynaptic Cell Type”. In: *The Journal of Neuroscience* 18.24 (Dec. 1998), pp. 10464–10472. ISSN: 0270-6474. DOI: `10.1523/JNEUROSCI.18-24-10464.1998`.

[46] Daniele Ielmini. *Neuromorphic computing with emerging memory devices - YouTube*. 2018.

[47] M. T. Sharbati et al. “Low-Power, Electrochemically Tunable Graphene Synapses for Neuromorphic Computing”. In: *Advanced Materials* 30.36 (Sept. 2018), p. 1802353. ISSN: 09359648. DOI: `10.1002/adma.201802353`.

[48] D. Ielmini. “Modeling the Universal Set/Reset Characteristics of Bipolar RRAM by Field- and Temperature-Driven Filament Growth”. In: *IEEE Transactions on Electron Devices* 58.12 (Dec. 2011), pp. 4309–4317. ISSN: 0018-9383. DOI: `10.1109/TED.2011.2167513`.

[49] A. Beck et al. “Reproducible switching effect in thin oxide films for memory applications”. In: *Applied Physics Letters* 77.1 (July 2000), pp. 139–141. ISSN: 0003-6951. DOI: `10.1063/1.126902`.

[50] A. Sawa. “Resistive switching in transition metal oxides”. In: *Materials Today* 11.6 (June 2008), pp. 28–36. ISSN: 1369-7021. DOI: `10.1016/S1369-7021(08)70119-6`.

[51] N. Yamada et al. “Rapidphase transitions of GeTeSb 2Te 3pseudobinary amorphous thin films for an optical disk memory”. In: *Journal of Applied Physics* 69.5 (Mar. 1991), pp. 2849–2856. ISSN: 0021-8979. DOI: `10.1063/1.348620`.

[52] N. Locatelli, V. Cros, and J. Grollier. “Spin-torque building blocks”. In: *Nature Materials* 13.1 (Jan. 2014), pp. 11–20. ISSN: 1476-1122. DOI: `10.1038/nmat3823`.

[53] J. Torrejon et al. “Neuromorphic computing with nanoscale spintronic oscillators”. In: *Nature* 547.7664 (2017), pp. 428–431. ISSN: 14764687. DOI: `10.1038/nature23011`. arXiv: `1701.07715`.

[54] M. Trentzsch et al. “A 28nm HKMG super low power embedded NVM technology based on ferroelectric FETs”. In: *2016 IEEE International Electron Devices Meeting (IEDM)*. IEEE, Dec. 2016, pp. 11.5.1–11.5.4. ISBN: 978-1-5090-3902-9. DOI: `10.1109/IEDM.2016.7838397`.

[55] D. Psaltis et al. “Holography in artificial neural networks”. In: *Nature* 343.6256 (Jan. 1990), pp. 325–330. ISSN: 0028-0836. DOI: `10.1038/343325a0`.

[56] A. N. Tait et al. “Neuromorphic photonic networks using silicon photonic weight banks”. In: *Scientific Reports* 7.1 (Dec. 2017), p. 7430. ISSN: 2045-2322. DOI: `10.1038/s41598-017-07754-z`.

[57] Q. Zhang et al. “Artificial neural networks enabled by nanophotonics”. In: *Light: Science and Applications* 8.1 (2019). ISSN: 20477538. DOI: `10.1038/s41377-019-0151-0`.

[58] M. Lee et al. “Brain-Inspired Photonic Neuromorphic Devices using Photodynamic Amorphous Oxide Semiconductors and their Persistent Photoconductivity”. In: *Advanced Materials* 29.28 (July 2017), p. 1700951. ISSN: 15214095. DOI: `10.1002/adma.201700951`.

[59] X. Zhu and W. D. Lu. “Optogenetics-Inspired Tunable Synaptic Functions in Memristors”. In: *ACS Nano* 12.2 (2018), pp. 1242–1249. ISSN: 1936086X. DOI: `10.1021/acsnano.7b07317`.

[60] S. Qin et al. “A light-stimulated synaptic device based on graphene hybrid phototransistor”. In: *2D Materials* 4.3 (Aug. 2017), p. 035022. ISSN: 2053-1583. DOI: `10.1088/2053-1583/aa805e`.

[61] Editorials. “The interface is still the device”. In: *Nature Materials* 11.2 (Feb. 2012), pp. 91–91. ISSN: 1476-1122. DOI: `10.1038/nmat3244`.

[62] H. Kroemer. “Nobel Lecture: Quasielectric fields and band offsets: teaching electrons new tricks”. In: *Reviews of Modern Physics* 73.3 (Oct. 2001), pp. 783–793. ISSN: 0034-6861. DOI: `10.1103/RevModPhys.73.783`.

[63] A Ohtomo and H. Y. Hwang. “A high-mobility electron gas at the LAO/STO heterointerface.” In: *Nature* 427.6973 (2004), pp. 423–426. ISSN: 0028-0836. DOI: `10.1038/nature04773`. arXiv: `arXiv:1011.1669v3`.

[64] N Reyren et al. “Superconducting interfaces between insulating oxides.” In: *Science (New York, N.Y.)* 317.5842 (Aug. 2007), pp. 1196–9. ISSN: 1095-9203. DOI: `10.1126/science.1146006`.

[65] W. Meevasana et al. “Creation and control of a two-dimensional electron liquid at the bare $SrTiO_3$ surface”. In: *Nature Materials* 10.2 (2011), pp. 114–118. ISSN: 14764660. DOI: `10.1038/nmat2943`.

[66] “Engineering two-dimensional superconductivity and Rashba spin-orbit coupling in $LaAlO_3$ / $SrTiO_3$ quantum wells by selective orbital occupancy”. In: *Nature Communications* 6.1 (Dec. 2015), p. 6028. ISSN: 20411723. DOI: `10.1038/ncomms7028`.

[67] A. Tebano et al. “Room-Temperature Giant Persistent Photoconductivity in $SrTiO_3$/$LaAlO_3$ Heterostructures”. In: *ACS Nano* 6.2 (Feb. 2012), pp. 1278–1283. ISSN: 1936-0851. DOI: `10.1021/nn203991q`.

[68] R. W. Simon et al. “Lowloss substrate for epitaxial growth of hightemperature superconductor thin films”. In: *Applied Physics Letters* 53.26 (Dec. 1988), pp. 2677–2679. ISSN: 0003-6951. DOI: `10.1063/1.100543`.

[69] H. Lehnert et al. “A powder diffraction study of the phase transition in $LaAlO_3$”. In: *Zeitschrift für Kristallographie - Crystalline Materials* 215.9 (Jan. 2000), pp. 536–541. ISSN: 2196-7105. DOI: `10.1524/zkri.2000.215.9.536`.

[70] S. A. Hayward et al. “Transformation processes in $LaAlO_3$: Neutron diffraction, dielectric, thermal, optical, and Raman studies”. In: *Phys. Rev. B* 72 (5 Aug. 2005), p. 054110. DOI: `10.1103/PhysRevB.72.054110`.

[71] D. de Ligny and P. Richet. "High-temperature heat capacity and thermal expansion of $SrTiO_3$ and $SrZrO_3$ perovskites". In: *Phys. Rev. B* 53 (6 Feb. 1996), pp. 3013–3022. DOI: `10.1103/PhysRevB.53.3013`.

[72] P. Delugas, V. Fiorentini, and A. Filippetti. "Dielectric properties and long-wavelength optical modes of the high-κ oxide $LaAlO_3$". In: *Phys. Rev. B* 71 (13 Apr. 2005), p. 134302. DOI: `10.1103/PhysRevB.71.134302`.

[73] S. Thiel et al. "Tunable Quasi-Two-Dimensional Electron Gases in Oxide Heterostrustures". In: *Science* 313.August (2006), p. 1942.

[74] A. F. Santander-Syro et al. "Two-dimensional electron gas with universal subbands at the surface of $SrTiO_3$". In: *Nature* 469.7329 (Jan. 2011), pp. 189–194. ISSN: 14764687. DOI: `10.1038/nature09720`.

[75] J. G. Bednorz and K. A. Müller. "Perovskite-Type Oxidesthe New Approach to High-Tc Superconductivity. Nobel Lecture". In: *Angewandte Chemie International Edition in English* 27.5 (1988), pp. 735–748.

[76] H. P. R. Frederikse, W. R. Thurber, and W. R. Hosler. "Electronic Transport in Strontium Titanate". In: *Phys. Rev.* 134 (2A Apr. 1964), A442–A445. DOI: `10.1103/PhysRev.134.A442`.

[77] W. Luo et al. "Structural and electronic properties of n-doped and p-doped $SrTiO_3$". In: *Phys. Rev. B* 70 (21 Dec. 2004), p. 214109. DOI: `10.1103/PhysRevB.70.214109`.

[78] N. Nakagawa, H. Y. Hwang, and D. A. Muller. "Why some interfaces cannot be sharp". In: *Nature Materials* 5.3 (2006), pp. 204–209. ISSN: 1476-1122. DOI: `10.1038/nmat1569`.

[79] G. Herranz et al. "High mobility conduction at (110) and (111) $LaAlO_3/SrTiO_3$ interfaces". In: *Scientific Reports* 2.110 (2012), pp. 3–7. ISSN: 20452322. DOI: `10.1038/srep00758`. arXiv: `1210.7955`.

[80] G. Herranz et al. "Controlling high-mobility conduction in $SrTiO_3$ by oxide thin film deposition". In: *Applied Physics Letters* 94.1 (Jan. 2009), p. 012113. ISSN: 00036951. DOI: `10.1063/1.3063026`.

[81] G. Herranz et al. "High Mobility in $LaAlO_3/SrTiO_3$ Heterostructures: Origin, Dimensionality, and Perspectives". In: *Phys. Rev. Lett.* 98 (21 May 2007), p. 216803. DOI: `10.1103/PhysRevLett.98.216803`.

[82] C. Cen et al. "Oxide nanoelectronics on demand." In: *Science (New York, N.Y.)* 323.5917 (Feb. 2009), pp. 1026–30. ISSN: 1095-9203. DOI: `10.1126/science.1168294`.

[83] F. Bi et al. "Water-cycle mechanism for writing and erasing nanostructures at the $LaAlO_3$ / $SrTiO_3$ interface". In: *Applied Physics Letters* 97.17 (Oct. 2010), p. 173110. ISSN: 0003-6951. DOI: `10.1063/1.3506509`.

[84] K. A. Brown et al. "Giant conductivity switching of LaAlO$_3$/SrTiO$_3$ heterointerfaces governed by surface protonation". In: *Nature Communications* 7 (2016), pp. 1–6. ISSN: 20411723. DOI: `10.1038/ncomms10681`.

[85] W. Dai et al. "Tailoring LaAlO$_3$/SrTiO$_3$Interface Metallicity by Oxygen Surface Adsorbates". In: *Nano Letters* 16.4 (Apr. 2016), pp. 2739–2743. ISSN: 1530-6984. DOI: 10.1021/acs.nanolett.6b00421.

[86] E. Lesne et al. "Suppression of the critical thickness threshold for conductivity at the LaAlO$_3$/SrTiO$_3$interface". In: *Nature Communications* 5 (2014), pp. 1–7. ISSN: 20411723. DOI: 10.1038/ncomms5291.

[87] T. N. Morgan. "The DX centre". In: *Semiconductor Science and Technology* 6.10 B (Oct. 1991), B23–B26. ISSN: 02681242. DOI: 10.1088/0268-1242/6/10B/004.

[88] J. Z. Li et al. "Persistent photoconductivity in Ga$_{1x}$In$_x$N$_y$As$_{1y}$". In: *Applied Physics Letters* 75.13 (Sept. 1999), pp. 1899–1901. ISSN: 0003-6951. DOI: 10.1063/1.124865.

[89] U Scotti di Uccio et al. "Reversible and Persistent Photoconductivity at the NdGaO3/SrTiO$_3$ Conducting Interface". In: *Arxiv preprint arXiv:* (2012), p. 24. arXiv: 1206.5083.

[90] E. Di Gennaro et al. "Photoresponse dynamics in amorphous-LaAlO$_3$/SrTiO$_3$ interfaces". In: *Scientific Reports* 5 (2015), pp. 1–6. ISSN: 20452322. DOI: 10.1038/srep08393.

[91] C. Biswas et al. "Negative and Positive Persistent Photoconductance in Graphene". In: *Nano Letters* 11.11 (Nov. 2011), pp. 4682–4687. ISSN: 1530-6984. DOI: 10.1021/nl202266h.

[92] D. V. Lang and R. A. Logan. "Large-Lattice-Relaxation Model for Persistent Photoconductivity in Compound Semiconductors". In: *Physical Review Letters* 39.10 (Sept. 1977), pp. 635–639. ISSN: 0031-9007. DOI: 10.1103/PhysRevLett.39.635.

[93] Y. Kang, H.-h. Nahm, and S. Han. "Light-Induced Peroxide Formation in ZnO : Origin of Persistent Photoconductivity". In: *Nature Publishing Group* October (2016), pp. 1–7. DOI: 10.1038/srep35148.

[94] C. H. Henry and D. V. Lang. "Nonradiative capture and recombination by multiphonon emission in GaAs and GaP". In: *Phys. Rev. B* 15 (2 Jan. 1977), pp. 989–1016. DOI: 10.1103/PhysRevB.15.989.

[95] D. F. M. Goodman. "The Brian simulator". In: *Frontiers in Neuroscience* 3.2 (2010), pp. 192–197. ISSN: 16624548. DOI: 10.3389/neuro.01.026.2009.

[96] C. W. Schneider et al. "Microlithography of electron gases formed at interfaces in oxide heterostructures". In: *Applied physics letters* 89.12 (2006), p. 122101.

[97] T. S. Jespersen et al. "Patterning of high mobility electron gases at complex oxide interfaces". In: *Applied Physics Letters* 107.19 (2015), p. 191604. ISSN: 0003-6951. DOI: 10.1063/1.4935553.

[98] L. Li et al. "Very large capacitance enhancement in a two-demensional electron system". In: *Science (New York, N.Y.)* 332.May (2011), pp. 825–829.

[99] S. K. Kim et al. "Electric-field-induced Shift in the Threshold Voltage in LaAlO$_3$/SrTiO$_3$ Heterostructures". In: *Scientific Reports* 5.1 (July 2015), p. 8023. ISSN: 2045-2322. DOI: 10.1038/srep08023.

[100] S. K. Kim et al. "Capacitance-voltage analysis of LaAlO$_3$/SrTiO$_3$ heterostructures". In: *Applied Physics Letters* 102.11 (2013). ISSN: 00036951. DOI: 10.1063/1.4798334.

[101] G. Wu et al. “Electrically induced colossal capacitance enhancement in $LaAlO_3/SrTiO_3$ heterostructures”. In: *NPG Asia Materials* 5.10 (2013), e65–e65. ISSN: 1884-4049. DOI: 10.1038/am.2013.48.

[102] G Herranz et al. “High mobility conduction at (110) and (111) $LaAlO_3/SrTiO_3$ interfaces”. In: *Scientific Reports* 2 (2012). ISSN: 20452322. DOI: 10.1038/srep00758.

[103] B. J. Oneill et al. “Catalyst design with atomic layer deposition”. In: *ACS Catalysis* 5.3 (2015), pp. 1804–1825. ISSN: 21555435. DOI: 10.1021/cs501862h.

[104] S. Shi et al. “ Structural and Optical Properties of Amorphous Al_2O_3 Thin Film Deposited by Atomic Layer Deposition ”. In: *Advances in Condensed Matter Physics* 2018 (2018), pp. 1–10. ISSN: 1687-8108. DOI: 10.1155/2018/7598978.

[105] O. Vlasin et al. “Optical Imaging of Nonuniform Ferroelectricity and Strain at the Diffraction Limit”. In: *Scientific Reports* 5.1 (Dec. 2015), p. 15800. ISSN: 2045-2322. DOI: 10.1038/srep15800.

[106] B. Romain and F. G. Dan. *https://brian2.readthedocs.io/en/stable/index.html – Brian Simulator*.

[107] M. F. Bear, B. W. Connors, and M. A. Paradiso. *Neuroscience: Exploring the brain*. Vol. 2. Lippincott Williams & Wilkins, 2007.

[108] S. Song, K. D. Miller, and L. F. Abbott. “Competitive Hebbian learning through spike-timing-dependent synaptic plasticity”. In: *Nature Neuroscience* 3.9 (Sept. 2000), pp. 919–926. ISSN: 1097-6256. DOI: 10.1038/78829.

[109] M. V. M. H. Tsodyks. “The neural code between neocortical pyramidal neurons depends”. In: *Proceedings of the National Academy of Sciences of the United States of America* 94.January (1997), pp. 719–723.

[110] A. L. HODGKIN and A. F. HUXLEY. “A quantitative description of membrane current and its application to conduction and excitation in nerve.” In: *The Journal of physiology* 117.4 (Aug. 1952), pp. 500–44. ISSN: 0022-3751.

[111] R. A. Marcus. “Exchange reactions and electron transfer reactions including isotopic exchange. Theory of oxidation-reduction reactions involving electron transfer. Part 4.A statistical-mechanical basis for treating contributions from solvent, ligands, and inert salt”. In: *Discuss. Faraday Soc.* 29.0 (Jan. 1960), pp. 21–31. ISSN: 0366-9033. DOI: 10.1039/DF9602900021.

[112] J. R. Miller, L. T. Calcaterra, and G. L. Closs. “Intramolecular long-distance electron transfer in radical anions. The effects of free energy and solvent on the reaction rates”. In: *Journal of the American Chemical Society* 106.10 (May 2002), pp. 3047–3049. DOI: 10.1021/ja00322a058.

[113] P. L. Houston. *Chemical Kinetics and Reaction Dynamics.* Dover Publications, 2012. ISBN: 9780486131696.

[114] G. A. Parada et al. “Concerted proton-electron transfer reactions in the Marcus inverted region.” In: *Science (New York, N.Y.)* 364.6439 (May 2019), pp. 471–475. ISSN: 1095-9203. DOI: 10.1126/science.aaw4675.

[115] J. C. Bourgoin and A. Mauger. “Physical origin of the *DX* center”. In: *Applied Physics Letters* 53.9 (Aug. 1988), pp. 749–751. DOI: `10.1063/1.99821`.

[116] T. Ihn. *Semiconductor nanostructures: quantum states and electronic transport*. Oxford University Press, 2010, p. 552. ISBN: 9780199534425.

[117] S. Lany and A. Zunger. “Intrinsic *DX* Centers in Ternary Chalcopyrite Semiconductors”. In: *Phys. Rev. Lett.* 100 (1 Jan. 2008), p. 016401. DOI: `10.1103/PhysRevLett.100.016401`.

[118] M. C. Tarun, F. A. Selim, and M. D. McCluskey. “Persistent Photoconductivity in Strontium Titanate”. In: *Phys. Rev. Lett.* 111 (18 Oct. 2013), p. 187403. DOI: `10.1103/PhysRevLett.111.187403`.

[119] D. Eom, C.-Y. Moon, and J.-Y. Koo. “Switching the Charge State of Individual Surface Atoms at Si(111)-$\sqrt{3} \times \sqrt{3}$:B Surfaces”. In: *Nano Letters* 15.1 (Jan. 2015), pp. 398–402. DOI: `10.1021/nl503724x`.

[120] B. Linares-Barranco et al. “On Spike-Timing-Dependent-Plasticity, Memristive Devices, and Building a Self-Learning Visual Cortex”. In: *Frontiers in Neuroscience* 5 (2011), p. 26. ISSN: 1662-453X. DOI: `10.3389/fnins.2011.00026`.

[121] “Plasticity in memristive devices for spiking neural networks”. In: *Frontiers in Neuroscience* 9.MAR (Mar. 2015), pp. 1–16. ISSN: 1662453X. DOI: `10.3389/fnins.2015.00051`.

[122] “Learning through ferroelectric domain dynamics in solid-state synapses”. In: *Nature Communications* 8.1 (Apr. 2017), p. 14736. ISSN: 2041-1723. DOI: `{10.1038/ncomms14736}`.

[123] N. Nakagawa, H. Y. Hwang, and D. A. Muller. “Why some interfaces cannot be sharp”. In: *Nature Materials* 5.3 (2006), pp. 204–209. ISSN: 14764660. DOI: `10.1038/nmat1569`.

[124] J. Gazquez et al. “Competition between Polar and Nonpolar Lattice Distortions in Oxide Quantum Wells: New Critical Thickness at Polar Interfaces”. In: *Physical Review Letters* 119.10 (Sept. 2017), p. 106102. ISSN: 0031-9007. DOI: `10.1103/PhysRevLett.119.106102`.

[125] C. Wetzel et al. “Pressure Induced Deep Gap State of Oxygen in GaN”. In: *Phys. Rev. Lett.* 78 (20 May 1997), pp. 3923–3926. DOI: `10.1103/PhysRevLett.78.3923`.

[126] T. Thio et al. “DX centers in II-VI semiconductors and heterojunctions”. In: *Journal of electronic materials* 25.2 (1996), pp. 229–233.

[127] P. Coleman. *Introduction to many-body physics*. Cambridge University Press, 2015.

[128] G. D. Mahan. *Many-particle physics*. Springer Science & Business Media, 2013.

[129] Z. Wang et al. “Memristors with diffusive dynamics as synaptic emulators for neuromorphic computing”. In: *Nature Materials* 16.1 (2017), pp. 101–108. ISSN: 14764660. DOI: `10.1038/nmat4756`.

[130] M. Ignatov et al. “Memristive stochastic plasticity enables mimicking of neural synchrony: Memristive circuit emulates an optical illusion”. In: *Science Advances* 3.10 (2017), pp. 1–10. ISSN: 23752548. DOI: `10.1126/sciadv.1700849`.

[131] T. Tuma et al. “Stochastic phase-change neurons”. In: *Nature Nanotechnology* 11.8 (2016), pp. 693–699. ISSN: 17483395. DOI: `10.1038/nnano.2016.70`.

[132] "Neural-like computing with populations of superparamagnetic basis functions". In: *Nature Communications* 9.1 (2018), p. 1. ISSN: 20411723. DOI: `10.1038/s41467-018-03963-w`.

[133] C. Mead. "Neuromorphic Electronic Systems". In: *Proceedings of the IEEE* 78.10 (1990), pp. 1629–1636.

[134] K. Aizawa. "Computational Sensors--Vision VLSI". In: *IEICE TRANSACTIONS on Information and Systems* 82.3 (1999), pp. 580–588.

[135] C. Simon Chane et al. "Event-Based Tone Mapping for Asynchronous Time-Based Image Sensor". In: *Frontiers in Neuroscience* 10 (Aug. 2016), p. 391. ISSN: 1662-453X. DOI: `10.3389/fnins.2016.00391`.

[136] M. Osswald et al. "A spiking neural network model of 3D perception for event-based neuromorphic stereo vision systems". In: *Scientific Reports* 7.1 (Feb. 2017), p. 40703. ISSN: 2045-2322. DOI: `10.1038/srep40703`.

[137] D. Hebb. "The Organization of Behavior". In: *Brain research bulletin* 50.5-6 (1949), p. 437. ISSN: 0361-9230.

[138] H Markram et al. "Regulation of synaptic efficacy by coincidence of postsynaptic APs and EPSPs." In: *Science (New York, N.Y.)* 275.5297 (Jan. 1997), pp. 213–5. ISSN: 0036-8075. DOI: `10.1126/SCIENCE.275.5297.213`.

[139] G. Q. Bi and M. M. Poo. "Synaptic modifications in cultured hippocampal neurons: dependence on spike timing, synaptic strength, and postsynaptic cell type." In: *The Journal of neuroscience : the official journal of the Society for Neuroscience* 18.24 (Dec. 1998), pp. 10464–72. ISSN: 0270-6474. DOI: `10.1523/JNEUROSCI.18-24-10464.1998`.

[140] C. Zamarreño-Ramos et al. "On Spike-Timing-Dependent-Plasticity, Memristive Devices, and Building a Self-Learning Visual Cortex". In: *Frontiers in Neuroscience* 5 (Mar. 2011), p. 26. ISSN: 1662-4548. DOI: `10.3389/fnins.2011.00026`.

[141] O. Bichler et al. "Extraction of temporally correlated features from dynamic vision sensors with spike-timing-dependent plasticity". In: *Neural Networks* 32 (Aug. 2012), p. 339. ISSN: 0893-6080. DOI: `10.1016/J.NEUNET.2012.02.022`.

[142] W. J. Hu et al. "Colossal X-Ray-Induced Persistent Photoconductivity in Current Perpendicular - to - Plane Ferroelectric/Semiconductor Junctions". In: *Advanced Functional Materials* 28.6 (Feb. 2018), p. 1704337. ISSN: 1616301X. DOI: `10.1002/adfm.201704337`.

[143] H. Z. Shouval, M. F. Bear, and L. N. Cooper. "A unified model of NMDA receptor-dependent bidirectional synaptic plasticity." In: *Proceedings of the National Academy of Sciences of the United States of America* 99.16 (Aug. 2002), pp. 10831–6. ISSN: 0027-8424. DOI: `10.1073/pnas.152343099`.

[144] S. R. Kheradpisheh, M. Ganjtabesh, and T. Masquelier. "Bio-inspired unsupervised learning of visual features leads to robust invariant object recognition". In: *Neurocomputing* 205 (Sept. 2016), pp. 382–392. ISSN: 0925-2312. DOI: `10.1016/J.NEUCOM.2016.04.029`.

[145] L. F. Abbott and S. B. Nelson. "Synaptic plasticity: taming the beast". In: *Nature Neuroscience* 3.S11 (Nov. 2000), pp. 1178–1183. ISSN: 1097-6256. DOI: `10.1038/81453`.

[146] Z. Wang et al. “Fully memristive neural networks for pattern classification with unsupervised learning”. In: *Nature Electronics* 1.2 (Feb. 2018), pp. 137–145. ISSN: 2520-1131. DOI: `10.1038/s41928-018-0023-2`.

[147] A. Banino et al. “Vector-based navigation using grid-like representations in artificial agents”. In: *Nature* 557.7705 (May 2018), pp. 429–433. ISSN: 0028-0836. DOI: `10.1038/s41586-018-0102-6`.

[148] A. D. Lien and M. Scanziani. “Cortical direction selectivity emerges at convergence of thalamic synapses”. In: *Nature* 558.7708 (June 2018), pp. 80–86. ISSN: 0028-0836. DOI: `10.1038/s41586-018-0148-5`.

[149] B. L. McNaughton et al. “Path integration and the neural basis of the ’cognitive map’”. In: *Nature Reviews Neuroscience* 7.8 (Aug. 2006), pp. 663–678. ISSN: 1471-003X. DOI: `10.1038/nrn1932`.

[150] P. Nelson. *From photon to neuron: Light, imaging, vision*. Princeton University Press, 2017.

[151] D. Thomson et al. “Roadmap on silicon photonics”. In: *Journal of Optics* 18.7 (July 2016), p. 073003. ISSN: 2040-8978. DOI: `10.1088/2040-8978/18/7/073003`.

[152] J. Park et al. “Creation of a two-dimensional electron gas at an oxide interface on silicon”. In: *Nature Communications* 1.1 (Dec. 2010), p. 94. ISSN: 2041-1723. DOI: `10.1038/ncomms1096`.

[153] S. Thiel et al. “Tunable Quasi-Two-Dimensional Electron Gases in Oxide Heterostructures”. In: *Science* 313.5795 (Sept. 2006), pp. 1942–1945. ISSN: 0036-8075. DOI: `10.1126/SCIENCE.1131091`.

[154] M. Scigaj et al. “Conducting interfaces between amorphous oxide layers and $SrTiO_3$(110) and $SrTiO_3$(111)”. In: *Solid State Ionics* 281 (Nov. 2015), pp. 68–72. ISSN: 01672738. DOI: `10.1016/j.ssi.2015.09.002`.

[155] G. Herranz et al. “Engineering two-dimensional superconductivity and Rashba spin-orbit coupling in $LaAlO_3$ / $SrTiO_3$ quantum wells by selective orbital occupancy”. In: *Nature Communications* 6.1 (Dec. 2015), p. 6028. ISSN: 20411723. DOI: `10.1038/ncomms7028`.

[156] Y. Chen et al. “Metallic and insulating interfaces of amorphous $SrTiO_3$-based oxide heterostructures”. In: *Nano Letters* 11.9 (2011), pp. 3774–3778. ISSN: 15306984. DOI: `10.1021/nl201821j`.

[157] Z. Q. Liu et al. “Origin of the Two-Dimensional Electron Gas at $LaAlO_3/SrTiO_3$ Interfaces: The Role of Oxygen Vacancies and Electronic Reconstruction”. In: *Physical Review X* 3.2 (2013). ISSN: 21603308. DOI: `10.1103/PhysRevX.3.021010`.

[158] M. Scigaj et al. “Conducting interfaces between amorphous oxide layers and $SrTiO_3$(110) and $SrTiO_3$(111)”. In: *Solid State Ionics* 281 (Nov. 2015), pp. 68–72. ISSN: 01672738. DOI: `10.1016/j.ssi.2015.09.002`.

[159] G. Herranz et al. “High mobility conduction at (110) and (111) $LaAlO_3/SrTiO_3$ interfaces”. In: *Scientific Reports* 2 (2012). ISSN: 20452322. DOI: `10.1038/srep00758`.

[160] Y.-C. Wu et al. "Extrinsic Origin of Persistent Photoconductivity in Monolayer MoS2 Field Effect Transistors". In: *Scientific Reports* 5.1 (Sept. 2015), p. 11472. ISSN: 2045-2322. DOI: `10.1038/srep11472`.

[161] A. Rastogi et al. "Photoconducting state and its perturbation by electrostatic fields in oxide-based two-dimensional electron gas". In: *Physical Review B - Condensed Matter and Materials Physics* 86.7 (Aug. 2012), p. 075127. ISSN: 10980121. DOI: `10.1103/PhysRevB.86.075127`.

[162] H. L. Lu et al. "Reversible insulator-metal transition of $LaAlO_3/SrTiO_3$ interface for non-volatile memory". In: *Scientific Reports* 3.1 (Dec. 2013), p. 2870. ISSN: 20452322. DOI: `10.1038/srep02870`.

[163] K. X. Jin et al. "Photoinduced modulation and relaxation characteristics in $LaAlO_3/SrTiO_3$ heterointerface". In: *Scientific Reports* 5.1 (Aug. 2015), p. 8778. ISSN: 20452322. DOI: `10.1038/srep08778`.

[164] J. Sun et al. "Optoelectronic Synapse Based on IGZO-Alkylated Graphene Oxide Hybrid Structure". In: *Advanced Functional Materials* 28.47 (Nov. 2018), p. 1804397. ISSN: 1616301X. DOI: `10.1002/adfm.201804397`.

[165] M. Kumar, S. Abbas, and J. Kim. "All-Oxide-Based Highly Transparent Photonic Synapse for Neuromorphic Computing". In: *ACS Applied Materials and Interfaces* 10.40 (Oct. 2018), pp. 34370–34376. ISSN: 19448252. DOI: `10.1021/acsami.8b10870`.

[166] Y. Yang et al. "Light stimulated IGZO-based electric-double-layer transistors for photoelectric neuromorphic devices". In: *IEEE Electron Device Letters* 39.6 (June 2018), pp. 897–900. ISSN: 07413106. DOI: `10.1109/LED.2018.2824339`.

[167] C. S. Chane et al. "Event-based tone mapping for asynchronous time-based image sensor". In: *Frontiers in Neuroscience* 10.AUG (Aug. 2016), p. 391. ISSN: 1662453X. DOI: `10.3389/fnins.2016.00391`.

[168] O. Bichler et al. "Extraction of temporally correlated features from dynamic vision sensors with spike-timing-dependent plasticity". In: *Neural Networks* 32 (Aug. 2012), pp. 339–348. ISSN: 0893-6080. DOI: `10.1016/J.NEUNET.2012.02.022`.

[169] M. Tawfik, X. Tonnellier, and C. Sansom. *Light source selection for a solar simulator for thermal applications: A review*. July 2018. DOI: `10.1016/j.rser.2018.03.059`.

[170] F. Trier et al. "Degradation of the interfacial conductivity in $LaAlO_3$ /$SrTiO_3$ heterostructures during storage at controlled environments". In: *Solid State Ionics* 230.C (2013), pp. 12–15. ISSN: 01672738. DOI: `10.1016/j.ssi.2012.08.005`.

[171] A. B. Carlson and A Bruce. "An Introduction to Signals and Noise in Electrical Communication". In: *Printed in Singapore, McGraw-Hill Communication Systems* (2002).

[172] H. A. Atwater and A. Polman. "Plasmonics for improved photovoltaic devices." In: *Nature materials* 9.3 (Mar. 2010), pp. 205–13. ISSN: 1476-1122. DOI: `10.1038/nmat2629`.

[173] D. Cialla-May et al. *Recent progress in surface-enhanced Raman spectroscopy for biological and biomedical applications: From cells to clinics*. July 2017. DOI: `10.1039/c7cs00172j`.

[174] F. Amthor. *Neuroscience for dummies*. John Wiley & Sons, 2016.

[175] K. Boahen. “Retinomorphic vision systems”. In: *Proceedings of Fifth International Conference on Microelectronics for Neural Networks*. IEEE. 1996, pp. 2–14.

[176] M. Coll et al. “Towards Oxide Electronics: a Roadmap”. In: *Applied Surface Science* 482 (2019), pp. 1–93. ISSN: 01694332. DOI: `10.1016/j.apsusc.2019.03.312`.

[177] M. Imada, A. Fujimori, and Y. Tokura. “Metal-insulator transitions”. In: *Reviews of Modern Physics* 70.4 (Oct. 1998), pp. 1039–1263. ISSN: 0034-6861. DOI: `10.1103/RevModPhys.70.1039`. arXiv: `arXiv:1208.0637v1`.

[178] S.-I. Kim et al. “Giant electroresistive ferroelectric diode on 2DEG”. In: *Scientific reports* 5 (2015), p. 10548.

[179] S. Wang et al. “Ferroelectric Polarization-Modulated Interfacial Fine Structures Involving Two-Dimensional Electron Gases in Pb (Zr, Ti) O3/$LaAlO_3$/$SrTiO_3$ Heterostructures”. In: *ACS applied materials & interfaces* 10.1 (2017), pp. 1374–1382.

[180] E Lesne et al. “Suppression of the critical thickness threshold for conductivity at the $LaAlO_3$/$SrTiO_3$ interface”. In: *Nature communications* 5 (2014), p. 4291.

[181] T. Wolfram and S. Ellialtioglu. *Electronic and Optical Properties of D -Band Perovskites*. Cambridge: Cambridge University Press, 2006, p. 315. ISBN: 9780511541292. DOI: `10.1017/CBO9780511541292`.

[182] T. Wolfram. “Two-Dimensional Character of the Conduction Bands of *d*-Band Perovskites”. In: *Phys. Rev. Lett.* 29 (20 Nov. 1972), pp. 1383–1387. DOI: `10.1103/PhysRevLett.29.1383`.

[183] M. Breitschaft et al. “Two-dimensional electron liquid state at $LaAlO_3$-$SrTiO_3$ interfaces”. In: *Phys. Rev. B* 81 (15 Apr. 2010), p. 153414. DOI: `10.1103/PhysRevB.81.153414`.

[184] K. Yang et al. “High-Throughput Design of Two-Dimensional Electron Gas Systems Based on Polar/Nonpolar Perovskite Oxide Heterostructures”. In: *Scientific Reports* 6.September (2016), pp. 1–9. ISSN: 20452322. DOI: `10.1038/srep34667`.

[185] J. V. Li and G. Ferrari. *Capacitance Spectroscopy of Semiconductors*. 2018. ISBN: 9789814774543. DOI: `10.1201/b22451`.